OKINAWA INSTITUTE OF SCIENCE AND TECHNOLOGY
GRADUATE UNIVERSITY

Thesis submitted for the degree

Doctor of Philosophy

Improvements in optical techniques to investigate the behavior and neuronal network dynamics over long timescales

by

Viktoras Lisicovas

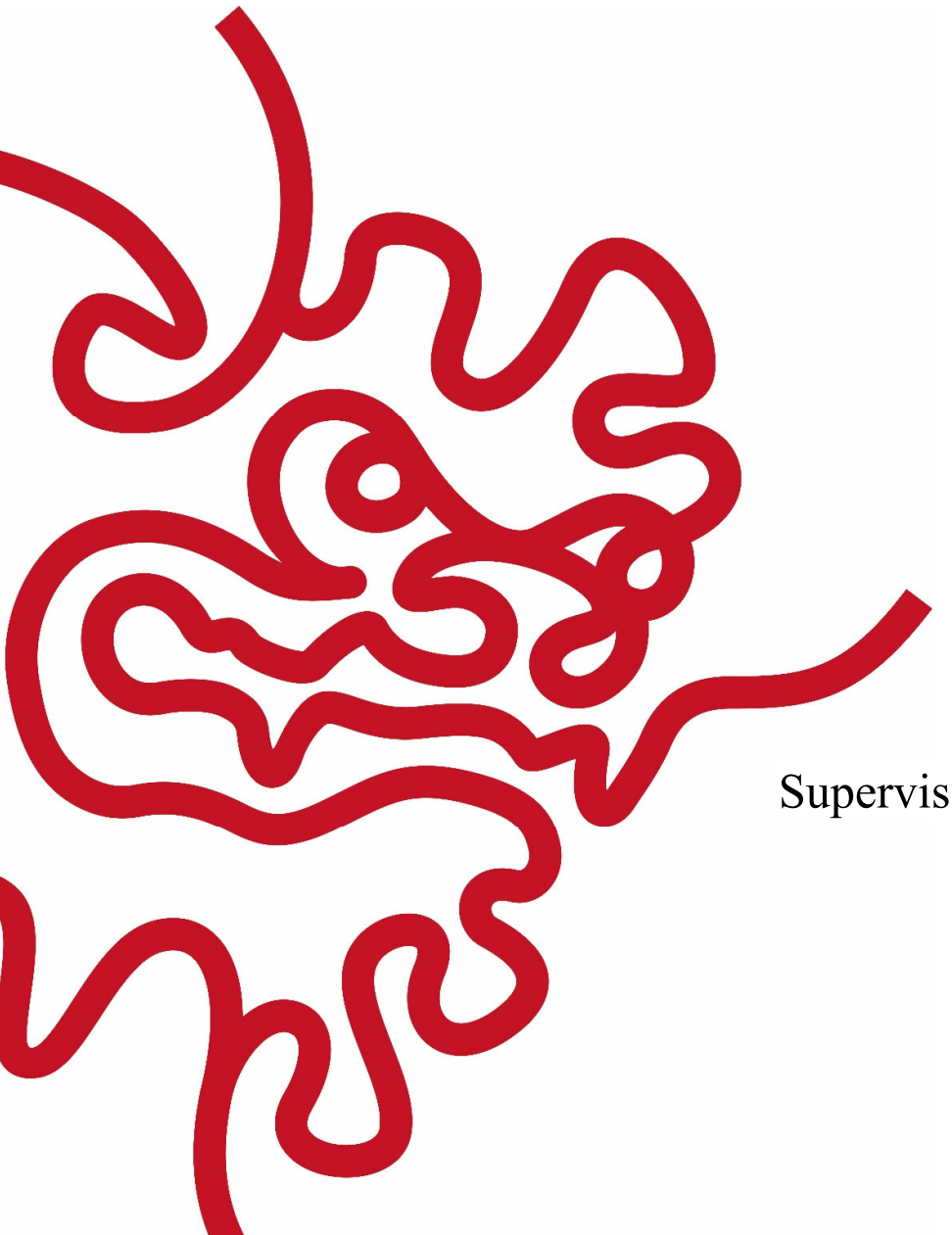

Supervisor: **Keshav M. Dani**

March, 2020

Declaration of Original and Sole Authorship

I, Viktoras Lisicovas, declare that this thesis entitled *Improvements in optical techniques to investigate the behavior and neuronal network dynamics over long timescales* and the data presented in it are original and my own work.

I confirm that:

- No part of this work has previously been submitted for a degree at this or any other university.
- References to the work of others have been clearly acknowledged. Quotations from the work of others have been clearly indicated, and attributed to them.
- In cases where others have contributed to part of this work, such contribution has been clearly acknowledged and distinguished from my own work.
- None of this work has been previously published elsewhere, with the exception of the following:
    - Lisicovas, Viktoras, Bala Murali Krishna Mariserla, Chakradhar Sahoo, Reuben T. Harding, Michael KL Man, E. Laine Wong, Julien Madéo, and Keshav M. Dani. "Improving Signal and Photobleaching Characteristics of Temporal Focusing Microscopy with the Increase in Pulse Repetition Rate." *Methods and protocols* 2, no. 3 (2019): 65. (Selected as the cover of the quarterly issue by the editors).

Date: 18th March, 2020

Signature: 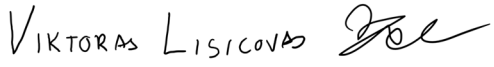

Abstract: Developments in optical technology have produced an important shift in experimental neuroscience from electrophysiological methods for observation and stimulation to all-optical solutions. One expects this trend to continue as future developments continue to deliver, and improve upon, the original promises of the technology: 1) minimally invasive actuation and recording of neurons, and 2) a drastic increase in targets that can be treated simultaneously. Moreover, as the high costs of the technology are reduced, one may expect its larger-scale adoption in the neuroscience community. In this thesis, I describe the development and implementation of two all-optical solutions for the analysis of behavior, neuronal signaling, and stimulation, which improve on previous state-of-the-art: (1) A minimally-invasive, high signal-to-noise two-photon microscopy setup capable of simultaneous, live-imaging of a large subset of sensory neurons post activation, and (2) a low-cost tracking solution to stimulate and record behavior. I begin this thesis with a review of recent advances in optical neuroscience techniques for the study of neuronal networks with the focus on work done in *Caenorhabditis elegans*. Then, in chapter 2, I describe my implementation of a two-photon temporal focusing microscopy setup and show significant improvements through the use of a high power/ high pulse repetition rate excitation system, enabling live imaging with high resolution for extended periods of time. I model temperature increase during a physiological imaging scenario for different repetition rates at fixed peak intensities and find range centered around 1 MHz to be optimal. Lastly, I describe the low-cost tracking setup with the ability to stimulate and record behavior over the course of hours. The setup is capable of two-color stimulation of optogenetic proteins over the area of the behavioral arena in combination with volatile chemicals. To showcase the utility of the system, I demonstrate behavioral analysis of integration of contradictory cues. In summary, I present a set of techniques for the interrogation of neural networks from animal behavior to neuronal activity, over timescales of potentially hours and days. These techniques can be used to address a new dimension of scientific questions.

Acknowledgment

Putting this work from thought to paper has been a long and winding road. As luck would have it, I have been blessed to interact with a number of remarkable people along the way, who showed me the true meaning of solid science, professionalism, comradery, compassion, and perseverance. I would like to express my kindest thanks to the people, without whom this work could not have been:

- My supervisor, Prof. Dr. Keshav M. Dani, whose laser-cut guidance in things big and small have kept me sane through the years. I am yet to meet anyone with more energy and enthusiasm for either science or people. Also for helping with research design, data interpretation, and writing.
- My Academic Mentor, Prof. Dr. Tadashi Yamamoto, whose kind words, advice, and perspective always helped me see the bright side.
- My Third Committee Member, Prof. Dr. Ichiro N. Maruyama, for providing support, resources and lab bench to assist with the development of the tracking system.
- All of the present and past members of the Femtosecond Spectroscopy Unit and in particular: Prof. Dr. Bala Murali Krishna Mariserla, for technical assistance and showing me a masterclass in optical alignment; Dr. Julien Madéo for numerous discussions and rock-solid advice in data acquisition, interpretation and French cuisine; Dr. Michael Ka Lun Man for advice on data analysis, interpretation and an inspiring example of effortless professionalism; Chakradhar Sahoo for help with optical alignment and valuable late-night discussions; and Reuben Harding for taking those hard first steps with me towards what became the microscopy setup described herein.
- All of the present and past members of the Information Processing Biology Unit and in particular: Dr. Takashi Murayama, who painstakingly mentored me in finer points of *C. elegans* research and always found time for a lengthy midnight discussion; Dr. Eichiro Saita, who provided invaluable advice on implementation of odor stimulation; Dr. Yuto Momohara and Andrew Mugo for refreshing breaks; and (now Dr.) Tosif Ahamed, who is

my *de facto* data analysis guru and one-stop-shop of excellent advice and positivity.

- OIST Engineering Section for granting access, training, and help with microscopy and manufacturing, in particular: Dr. Kieran Deasy for always finding time in his busy schedule to help with microfabrication; and Takuya Miyazawa for assistance with fluorescence lifetime measurements.
- Yumi Ito and Hitomi Ohtaki, Research Associates from Femtosecond Spectroscopy Unit and Information Processing Biology Unit for positive energy and helping out with all manner of paperwork.
- Dr. William Schafer, Dr. Edward Boyden, Dr. Cornellia Bargmann, Dr. Kevin M. Collins, Caenorhabditis Genetics Center, and Addgene for providing strains and plasmids used in this work and Nanoscribe for valuable advice on microfluidics manufacturing.
- OIST Graduate University for generous funding and support through this journey.
- My beautiful wife, Sakurako, family, and friends, who kept faith in spite of all the trials and tribulations.

Abbreviations

AMPA	α-amino-3-hydroxy-5-methyl-4-isoxazolepropionic acid
ATR	All-trans-Retinal
C. elegans	*Caenorhabditis elegans*
C1V1-ET/ET	A variant of chimeric fusion of channelrhodopsin-1 and *Volvox* VChR1
CGC	*Caenorhabditis Elegans* Genetics Center
ChR2	Channelrhodopsin 2
CMOS	Short for complementary metal-oxide-semiconductor
CREB	cAMP response element-binding protein
CRISPR	Clustered regularly interspaced short palindromic repeats
CrR	ChrimsonR red-shifted channelrhodopsin variant
CTX	chemotaxis
GCaMP	Genetically encoded calcium indicator
GFP	Green fluorescent protein
LED	Light-emitting diode
NGM	Nematode growth medium
NMDA	N-methyl-D-aspartate
NOPA	Non-colinear optical parametric amplifiers
NpHR	Halorodopsin
OP50	*E. coli* uracil auxotroph
OPA	Non-linear optical parametric amplifier
PC	Principal component
PCR	Polymerase chain reaction
PDMS	Polydimethylsiloxane
TRPV1	The transient receptor potential cation channel subfamily V member 1
WF-TeFo	Wide-field two-photon temporal focusing microscope

Nomenclature

μ_a	Absorption coefficient
C	Typical concentration of fluorophores
c	Speed of light in vacuum
F_a	The fraction of absorbed photons that do not result in two-photon emission
h	Planck constant
I	Peak power density
k	Specific thermal conductivity of brain tissue
d	Propagation length (two Rayleigh lengths)
$N_{1\lambda}$	Number of photons absorbed due to one-photon absorption of the medium
$N_{2\lambda}$-N_{em}	Number of absorbed photons that do not result in two-photon emission
N_a	Number of absorbed photons
N_τ	Total number of photons
P_A	Average laser power
q_r	Heat
S	Coherence parameter
T	Temperature
V	The volume of the excitation cylinder
ε	Heat source
v	Tangential velocity
Φ	Quantum efficiency
ω	Angular velocity
$\delta_{2\lambda}$	Two-photon cross-section at 960 nm
λ	The wavelength used for two-photon imaging

To my little Maya, who came into this world and beamed away all shadows.

Contents

List of Figures

List of Tables

Outline of the thesis

The main body of this thesis is structured into four parts:

1. In Chapter 1, I provide an introduction to the biology and behavior of *C. elegans*. Optical techniques for investigation of neuronal networks are then reviewed.
2. In Chapter 2, I demonstrate how wide-field two-photon temporal focusing microscopy benefits from an increased repetition rate.
3. In Chapter 3, I describe a population tracking and stimulation system capable of dual-color optogenetic stimulation. I validate the system by demonstrating the behavioral implications of contradictory cues.
4. I conclude in Chapter 4.

1 Literature Review

Abstract

The overarching goal of neuroscience is to bridge the disconnect between observed animal behavior and the underlying 'black-box' of information flows in the complex neuronal networks. New optical and optogenetic methods have the potential to drastically accelerate the progress in this direction. Of the model systems used in neuroscience, *Caehnorhabditis elegans* is particularly well suited to address this question with optical means. The relative simplicity of its anatomy has motivated the research of all aspects of *C. elegans* biology. It is the only model system to date to be described with the annotated genome sequence and complete connectome. Despite the small nervous system composed of only 302 neurons, this animal exhibit complex behavior on short and long time scales, including complex navigation, decision making, learning and even social behaviors. In this chapter, I provide an overview of the *C. elegans* nervous system and highlight previous work dealing with optical behavioral tracking, optogenetic manipulation and neuronal imaging techniques aimed at dissection of function of neuronal networks.

1.1 Introduction

With the growing understanding of neuronal physiology and mechanisms of information transmission and integration, there is a mounting interest in the neuroscience community to shift focus toward the analysis of the function of more extensive networks (Friston 2011). For decades functional imaging using functional magnetic resonance imaging aimed to do just that; however, the indirect measure of blood oxygen level-dependent activity is a macro-scale measure and suffers from poor signal-to-noise ratios (Logothetis et al. 2001). Therefore more direct methods of measuring neuronal activity are in active development (Scanziani and Häusser 2009).

An established method for measuring and manipulating neuronal activity is the *in vivo* electrophysiology, which has redefined the 20th-century neuroscience (Bickle 2016). The introduction of the electrophysiological techniques has, for the first time, enabled the dissection of mechanisms controlling the flow of electrical signals through neuronal tissue (Schwiening 2012). Additionally, the basic methodology was rapidly adapted for probing

and control of all conceivable neuronal cell types generating insights not only in the inner workings of neurons (Verkhratsky and Parpura 2014) but also the behavior of populations of neurons (Taketani and Baudry 2006).

Much like the introduction of electrophysiology, developments in optical imaging technology (J. N. D. Kerr and Denk 2008) and optogenetics (Fenno, Yizhar, and Deisseroth 2011) have sparked a modern revolution in neuroscience research. The former, coupled with genetically encoded activity probes, enables high-resolution imaging of neural activity over large volumes of neurons deep in the neural tissue and with minimal photo-damage (Ji, Freeman, and Smith 2016). The latter enables depolarization or inhibition of genetically targeted cells and cell populations. The combination of the two essentially recaptures an electrophysiological system (Hochbaum et al. 2014). Figure 1.1 presents a comparison between two families of techniques from a historical and practical perspective.

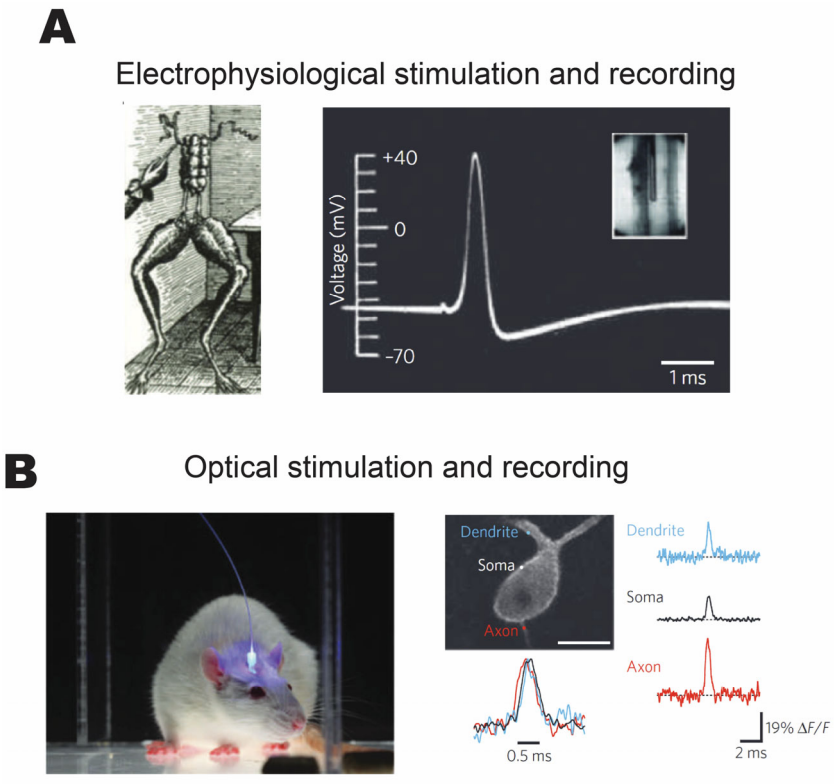

Figure 1.1 Historical comparison of electrophysiological and optical techniques for stimulation and recording. (A) The electrical stimulation of a frog nerve by Galvani revealing the electrical basis of neural information transmission and the first intracellularly recorded movement of action potential by Hodgkin and Huxley. (B) Optical stimulation of deep brain regions expressing optogenetic proteins and optical recording of action potentials from multiple sites simultaneously. Figure adapted from (Scanziani and Häusser 2009).

Electrophysiological methods, in general, require substantial dissection of the specimen, and it is virtually impossible to reuse the animal for subsequent experiments. Nevertheless, electrophysiology remains the 'gold standard' for analysis of neuronal activity, which is well illustrated by high signal-to-noise ratios of pioneering recordings of Hodgkin and Huxley (A. L. Hodgkin and Huxley 1939). On the other hand, optogenetic tools enable minimally invasive stimulation and recording of live, behaving animals. The same animal can be utilized for months after the installation of a cranial window (Goldey et al. 2014). The downsides, however, include the intrinsically noisy recordings and non-

specific labeling of neural targets (Scanziani and Häusser 2009). While electrophysiological methods remain the most accurate methods for measurement and control, optical methods have far surpassed the former in experimental throughput as well as intrinsic non-invasiveness offered by the use of light. These features of light-based technologies are what make it such an attractive tool for study of network dynamics.

Among the established animal models, the nematode *C. elegans* is particularly interesting for the study of functional connectivity. Optically transparent bodies, as well as the small number of neurons, make it particularly tractable by optical means (R. A. Kerr 2006). *C. elegans* is a genetically flexible system, enabling the expression of optogenetic tools with relative ease (Husson, Gottschalk, and Leifer 2013). In fact, *C. elegans* was the first model organism to use the green fluorescent protein as a marker (Chalfie et al. 1994). Additionally, its small size enables the study of both individual animal and population dynamics. A few pioneering studies have shown that these simple animals with 302 neurons are capable of unusually complex behaviors: long-term learning and adapting behavior to suit their environment (Morrison et al. 1999; Amano and Maruyama 2011; de Bono and Maricq 2005; Ghosh et al. 2016).

1.2 Overview of the nervous system of *C. elegans*

C. elegans is a small, detritivorous nematode found widely around the world (Kiontke and Sudhaus 2006). As a model organism, it was pioneered in the early 1960s by Sydney Brenner, who envisioned that it could be used for investigating developmental processes and nervous system functions (Brenner 1974). The biology of this species offers several advantages. Apart from fast generation time and simple cultivation conditions, they are of sufficient size to experiment on individual animals, but at the same time small enough to investigate a population without substantially changing the experimental setup. The main strength of this model organism lies in its genetic amenability. High robustness under mutagenesis and hermaphroditic reproduction offer additional benefits in making and maintaining new lines. Over the years, many mutant strains have been identified by forward genetic screens giving insights into many critical life processes (Wood 1988). It was the first multicellular organism to have its full genome sequenced, and the sequence is well annotated (Harris et al. 2010). Additionally, the developmental fate of each cell has been traced, and a number of tissue and cell-specific promoters have been identified

(Riddle 1997). Transgenic animals can be made relatively quickly by direct injection of foreign DNA into the gonad (Fire 1986; Evans 2006).

From the perspective of neuroscience, it was the first animal to have its complete connectome mapped, revealing the connectivity of all 302 neurons (White et al. 1986). The nervous system of the animal can be roughly divided into four categories based on information flow from inputs to observed behaviors: sensory neurons, interneurons, motor neurons, and polymodal neurons, which share the characteristics of two or more categories (polymodal). Others neurons still may be more important in the guidance of neuronal processes or maintenance than in information transmission. Neurons of the animal mostly exhibit monopolar or bipolar structure, with only a few showing higher degrees of branching. Furthermore, the position of soma and processes are almost invariable between individuals, making it easier to identify specific neurons (Hall, Lints, and Altun 2005).

The nervous system of *C. elegans* shares features with those of higher animals at the molecular and cellular levels. Despite the available connectome, polarity and type have not been determined for the vast majority of synapses. Recent research indicates that, at least in the case of interneurons, the majority of synapses is likely to be inhibitory, and is optimized to receive excitatory input from sensory neurons (Rakowski et al. 2013). Despite the small size of its neurons, most electrophysiological techniques can be applied to *C. elegans* (Goodman et al. 2012). Due to the lack of evidence for the presence of voltage-gated Na^+ channels, it is assumed that most information coding in the neural network of the animal occurs via graded potentials. However, advances in electrophysiological recordings and the small size of the network and neurons themselves suggest that information may be represented digitally (Mellem et al. 2008). Also, there are hints that locomotion direction is coded as two possible states: reverse or forward (Lockery and Goodman 2009). One recent study indicates that some neurons are likely to function as digital gates, while others as analog modulators. AIY neurons form inhibitory synapses to AIZ neurons, which locks them in a low-activity state. Upon inhibition of AIY, AIZ switches from an inactive to an active state in an all-or-none manner, with a narrow dynamic range resulting in animal initiating a reversal in movement direction. AIY neurons also form excitatory connections with RIB neurons, which have a much wider dynamic range and have been shown to modulate locomotion speed in accordance with the magnitude of neuronal activity (Li et al. 2014).

Powerful genetic approaches available for *C. elegans* have helped to identify many protein candidates that play essential roles in all stages of synaptic transmission. These findings indicate that features of synaptic signaling are highly conserved throughout the animal kingdom (Richmond 2005). The expression pattern of glutamate transporter EAT-4 suggests that 38 out of 118 anatomical neuronal classes are glutamatergic (Serrano-Saiz et al. 2013). So far, ten putative ionotropic glutamate receptor subunits have been found in *C. elegans*: 8 AMPA or kainate subfamilies and 2 of NMDA. Amino acid alignment with vertebrate homologs reveals many similarities. As in vertebrates, ionotropic glutamate receptors are implicated in long-term behavioral plasticity in *C. elegans* (Brockie and Maricq 2006). Furthermore, expression of the cAMP response element binding protein (CREB), required for long-term memory formation in animals ranging from sea slugs to mammals, is also essential for long-term memory in the nematode. More surprisingly, overexpression of *C. elegans* homolog of CREB, *chr-1*, results in enhanced long-term memory retention (Alcedo and Zhang 2013).

Considering that its nervous system is so small, an unexpected wealth of complexity is observed in *C. elegans* from foraging to social interactions and other aspects of complex behavior (de Bono and Maricq 2005; Kiontke and Sudhaus 2006). These observations can be partly explained by several peculiar features of its nervous system. First, the majority of neuronal processes can both receive and send potentials (Hall, Lints, and Altun 2005). Neurites of AIY interneurons have calcium transients that are independent of the neuronal soma (Chalasani et al. 2007; Larsch et al. 2013). Second, compartmentalization of axons has been observed previously in RIA neurons, where it plays a role in monitoring the animal's motion, accepting updates from its sensory system (Hendricks and Zhang 2013). It is not inconceivable that this feature of the nervous system is more prevalent. Secondly, many neurons are not strictly specialized but have evolved to perform different functions. Some neurons are capable of mechanosensation while functioning as interneurons. AVL, for instance, is a motor neuron, which has interneuron features. ASH neurons incorporate a number of different sensory modalities (Hall, Lints, and Altun 2005). Third, neuromodulators can have a dramatic effect on the activity of particular neurons. For example, the level of NLP-12, a cholecystokinin homolog, has been shown to modulate motor responses in local search behavior. NLP-12 release is modulated by dopaminergic DVA neurons, which may have a role in the integration of sensory

information about food availability (Bhattacharya et al. 2014). Furthermore, serotonin and insulin-like peptides are necessary for aversive learning through modulation of interneurons. Additional neuropeptides also are implicated in learning for other sensory modalities (McDiarmid, Ardiel, and Rankin 2015). These features, taken together, dramatically expand the complexity of the *C. elegans* nervous system beyond what might be expected from the connectome alone.

1.3 Olfaction and nociception in *C. elegans*

The chemosensory system of *C. elegans* is composed of 32 neurons found in the amphid, the phasmid, and neurons of the inner labia. Figure 1.2 shows the physiology and connectivity of sensory organs. These are exposed either directly or indirectly to the environment through pores in the cuticle made of socket and sheath cells. They are loosely specialized to respond to different classes of chemical cues, but also are observed to modulate sensitivity in a concerted manner (Cornelia I Bargmann 2006). Chemosensation in *C. elegans* is divided into two categories: gustatory and olfactory. Since gustatory cues are not volatile, while olfactory cues are, these two senses differ in the range over which their respective cues are detectable (C I Bargmann, Hartwieg, and Horvitz 1993; Cornelia I Bargmann 2006). Systematic behavioral screens have identified a number of substances that induce attraction or repulsion. *C. elegans* are observed to ascend gradients of cations, anions, cyclic nucleotides, and alkaline pH (Ward 1973) and show aversion to toxic cations (Sambongi et al. 1999). Similar experiments in olfactory preference have identified many volatile substances, including alcohols, amines, aldehydes, esters, organic acids, and heterocyclic compounds, to which specific preferences are exhibited by the animal (C I Bargmann, Hartwieg, and Horvitz 1993). In contrast to gustatory cues, the response to olfactory cues is more varied and is highly concentration-dependent. Individual neurons responsible for sensing many olfactory or gustatory cues have been identified: ASE, ADL, and ASH in the case of gustation and AWA, AWB, AWC, and ASH in olfaction (Cornelia I Bargmann 2006). More recently, it has been reported, however, that several different sensory neurons might respond to the same chemical cue as attractive or repulsive in a concentration-dependent manner (Yoshida et al. 2012; Taniguchi et al. 2014).

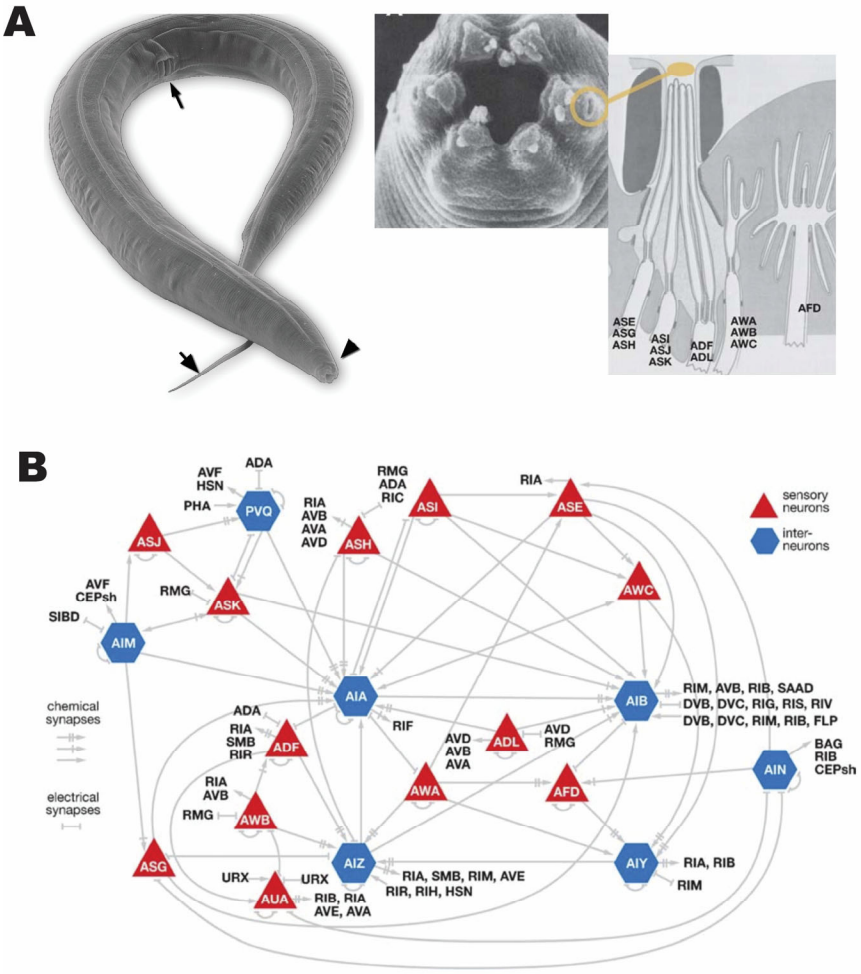

Figure 1.2. Olfactory and nociceptive system of *C. elegans*. (A) Electron microscopy image of the worm (arrows indicate the pharynx, vulva, and tail). Pharynx, the mouth of the animal, contains sensory amphid where neurons are exposed to the environment. (B) Connectivity diagram of different sensory neurons showing chemical and electrical connections. Adapted from (de Bono and Maricq 2005; Hall, Lints, and Altun 2005).

The ASH neuron mediates nociception in *C. elegans*. Exposure to high osmolality, a number of harmful compounds, such as heavy metals, detergents, acidic pH, and organic compounds produce an immediate reversal of direction, which requires ASH. Furthermore, the ASH neuron, in a similar manner, is necessary for withdrawal from a mechanical stimulation (Cornelia I Bargmann 2006). These observations establish the ASH neuron as a general sensor for damage detection, which, in conjunction with phasmid neurons in the

tail, transmit nociceptive signals to interneurons. The ASH forms connections with AVA, AVB, and AVD interneurons, which are responsible for the initiation of forward and backward locomotion (White et al. 1986). Direct activation of the ASH neuron is sufficient to induce a reversal response. It has been demonstrated by expressing the vertebrate TRPV1 channel in the ASH neuron and inducing avoidance behavior through the administration of capsaicin, an antagonist of TRPV1 channels (Cornelia I Bargmann 2006; Tobin et al. 2002). Additionally, a similar response has been observed through the expression of channelrhodopsin-2 (ChR2) in ASH and inducing activation of the neuron by exposure to blue light (Faumont et al. 2011). Glutamate release at synaptic sites of ASH with interneurons transmits sensory information through activation of AMPA and NMDA type glutamate receptors (Mellem et al. 2002).

1.4 Long-term behavioral plasticity

Research efforts spanning over three decades has uncovered a vast repertoire of behavioral plasticity in *C. elegans*. These include observed plasticity in all sensory modalities, including learning achieved through major sensory systems: mechanosensory, thermosensory, and chemosensory (Giles, Rose, and Rankin 2005). Additionally, behavioral plasticity has been shown in the application of sexual cues (Sakai et al. 2013) and as a response to changes in oxygen levels (Cheung et al. 2005) and humidity (Russell et al. 2014). Plasticity systems investigated thus far can be divided into several basic categories: non-associative learning (habituation), associative learning, imprinting (Ardiel and Rankin 2010), and decision making (see Figure 1.3). These studies, taken together, reveal unexpected behavioral plasticity in *C. elegans* despite its compact nervous system.

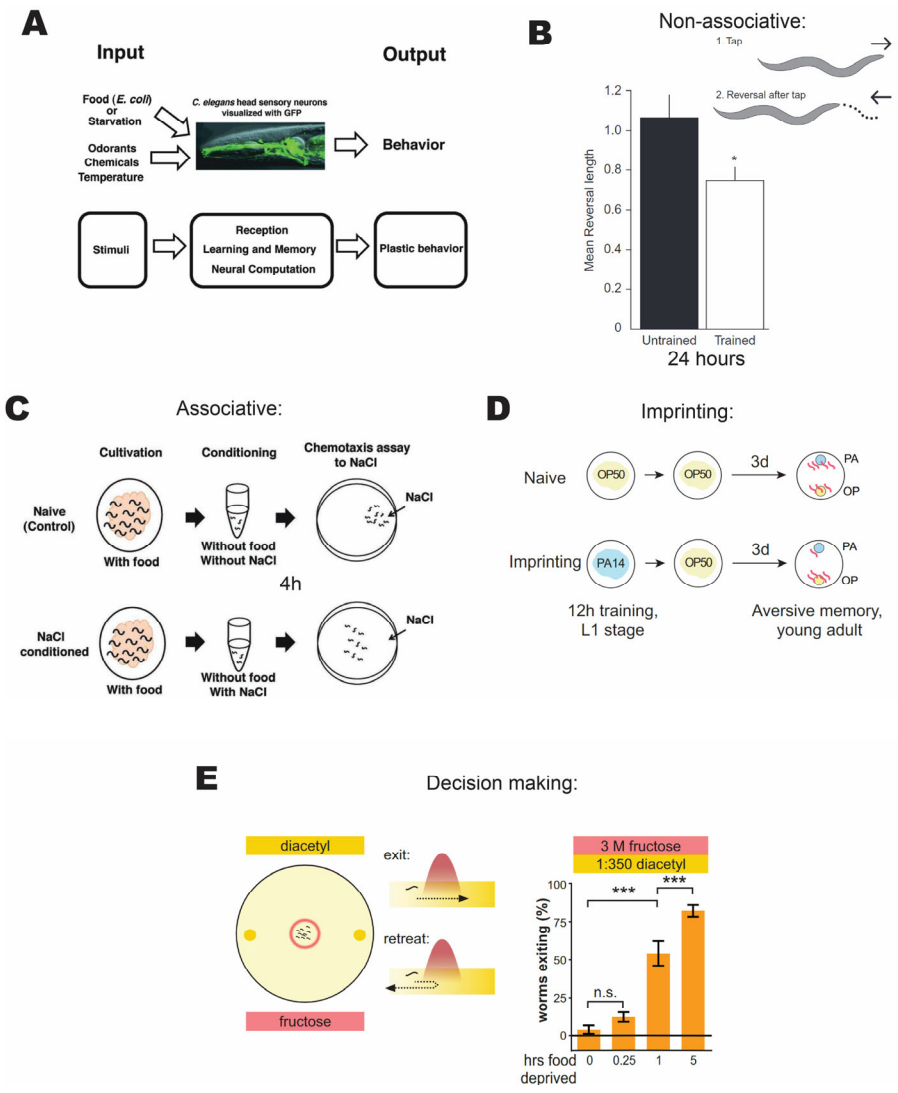

Figure 1.3 Relevant long time scale behavioral plasticity paradigms. (A) *C. elegans* neural system as an engine for studying plasticity of behavior. (B) Habituation is a form of non-associative plasticity, where a single sense loses sensitivity with repetition and can be retained for 24 hours. (C) Association of NaCl and starvation is a form of associative plasticity that can last for 4 hours. (D) Imprinting is learning that occurs only at an early developmental stage and lasts for life. In this case, learning to avoid noxious bacteria. (E) Behavioral decision-making paradigms, where animals reevaluate the cost and benefit of experiencing pain to gain reward based on their satiety state. Adapted from (Sasakura et al. 2013; McEwan and Rankin 2013; Jin, Pokala, and Bargmann 2016; Dipon Ghosh et al. 2016).

Mechanosensory stimulation induces reversal responses in *C. elegans*. If the animal is stimulated repeatedly, reversal responses reduce in magnitude, which serves as a measure of sensory habituation. Interestingly, this can be replicated by activating ChR2 expressed in touch receptor neurons (Timbers et al. 2013). When presented at spaced intervals, this training paradigm induces long-term memory for habituation in *C. elegans*. This effect is protein synthesis-dependent, as behavior is disrupted by heat shock, while training administered without resting periods is not. Furthermore, spaced training leads to decreased expression and changes in the distribution of glutamate receptor subunits on processes of interneurons in the posterior nerve cord (Rose et al., 2003). This change was later shown to be reversible in the case of heat shock delivery during reconsolidation (Rose and Rankin, 2006).

The study of associative learning in *C. elegans* traces its roots to the first report of animals showing preference to the temperature in which they were cultivated in an abundance of food (Hedgecock and Russell 1975). In the context of chemotaxis, initial evidence was provided by a study investigating behavioral plasticity towards Na^+ and Cl^- ions. Animals exposed to these ions in the presence or absence of food showed changes in preference on subsequent exposures (Wen et al. 1997). Later a similar paradigm was investigated, in which animals were left to starve in the presence and absence of NaCl for four hours. After conditioning, chemotaxis towards NaCl, as well as other soluble compounds, decreased, indicating that animals learned to associate starvation with the presence of particular substances (Saeki, Yamamoto, and Iino 2001).

Moreover, plasticity of learned avoidance responses was dependent on the expression of NMDA-type ionotropic glutamate receptor subunits NMR-1 and NMR-2, but not on GLR-1 or GLR-2, in contrast to long-term mechanosensory habituation memory. Expression of NMR-1 and NMR-2 in RIM interneurons rescued defective memory retention (Kano et al. 2008). Animals cultivated at a particular NaCl concentration will migrate toward this concentration when placed on a gradient. This indicates that animals can associate concentration with cultivation conditions. The ability to follow the concentration gradient was attributed to an ASE sensory neuron pair, which activates asymmetrically in response to salt concentrations below or above the preferred concentration (Suzuki et al. 2008). Recently it was shown with calcium imaging that memory of preferred conditions is stored directly in the ASE neuron, while the interneuron

network downstream of ASE only modulates motor output in accordance with a specific condition. This preference is plastic and can be changed within 4 hours (Luo, Wen, et al. 2014). Similar results were observed in the case of thermotaxis to a preferred temperature mediated by the AFD neuron (Luo, Cook, et al. 2014). These reports indicate that associations can be stored directly in the sensory neurons themselves.

Adult animals exposed to pathogenic bacteria on growth plates for four hours showed increased avoidance of the smell of the same pathogenic bacteria (Zhang, Lu, and Bargmann 2005). The same condition results in imprinting, if applied in the early stages of development (Jin, Pokala, and Bargmann 2016). This response was plastic, and otherwise normal sensitivity was not affected. Furthermore, this plasticity was dependent on serotonin modulation by ADF neurons (Zhang, Lu, and Bargmann 2005). Later the network for modulation of this aversive response was dissected through neuronal ablation and calcium imaging. Two neural circuits were identified for generation of naïve and trained aversion towards the pathogenic strain. The naïve response required AWC and AWB sensory-motor circuits, while ADF was necessary for trained responses through RIA interneurons and SMD motorneurons. ADF was also shown to play a role in the naïve response. Combined ablation of AIY and AIB interneurons, on the other hand, completely abolished aversive responses (Ha et al. 2010). Previously, animals have been compelled to climb artificial light gradients, when the AIY neuron was stimulated directly using optogenetic stimulation with ChR2 (Kocabas et al. 2012). This observation demonstrates that the AIY acts as a chemosensory input hub, and its activation alone is sufficient to induce behavior.

The two circuit aversive olfactory learning network in *C. elegans* is reminiscent of the regulation of fear responses in mice, where behavior depends on the interplay between low and high fear neurons in the amygdala (Herry et al. 2008; Ha et al. 2010). A recent report used optogenetic stimulation of a group of cells expressing ChR2 in the amygdala of a mouse, combined with fear conditioning to induce artificial fear response memories. Trained animals responded to optogenetic stimulation with an increased tendency to exhibit a freezing response, a hallmark of fear conditioning (Nabavi et al. 2014). When the functional similarities between fear response conditioning and aversive conditioning are taken into account, it is conceivable that a similar conditioning protocol, relying on optogenetic stimulation, could be implemented in the nematode as well.

An aversive olfactory conditioning paradigm was also reported to induce memory when animals were exposed to pure chemicals, rather than mixed stimuli (food). In this case, an initially attractive stimulus, diacetyl, was paired with an aversive acetic acid solution, which resulted in decreased chemotaxis toward diacetyl after training (Morrison et al. 1999). In this paradigm, mutant animals deficient in glutamate receptors did not show a reduction in attraction to diacetyl (Morrison and Van Der Kooy 2001). This paradigm was later modified to replace diacetyl with 1-propanol, a more neutral stimulus, which led to a pronounced difference in chemotaxis index before and after conditioning. When consecutive iterations of conditioning trials were presented with no or small delay, changes in chemotaxis persisted for only 3 hours. A memory that was induced using longer rests between consecutive iterations was shown to last for at least 12 hours after training. Furthermore, induced memory was dependent on protein synthesis. Analysis of mutants deficient in GLR-1 and NMR-1 as well as CREB mutants did not show any signs of memory retention 6 hours after conditioning, indicating that long-term memory failed to form (Amano and Maruyama 2011).

In summary, published research shows that *C. elegans* is capable of behavioral plasticity between different sensory modalities and on time scales of days. Moreover, the mechanisms mediating plasticity share features with more complex animals.

1.5 Optogenetic toolkit

Due to its amenability to genetic manipulation, its small size, and transparent body, *C. elegans* is particularly suited for manipulation and imaging using a number of optogenetic tools. Genetically expressed ChR2 has been widely used for the manipulation of neuronal activity with high temporal precision. This cationic ion channel is endogenous to the green alga, *Chlamydomonas reinhardtii*, where it functions in a photoreceptor system. Blue light with an excitation peak at 450-460 nm induces a conformation change in the cofactor all-trans-retinal (ATR), which renders the channel permeable to cations. ATR is an essential cofactor for the function of ChR2 and is not produced by *C. elegans* (G. Nagel et al. 2005). In physiological conditions, mostly Ca^{2+} are allowed to pass through ChR2, but K^{+} ions can also pass if they are present at high concentrations (E. Nagel et al. 2003). ChR2 was successfully expressed in muscles of *C. elegans*, where it caused predictable contraction upon stimulation with blue light. Furthermore, expression in ALM,

PLM, AVM, and PVM mechanosensory neurons induces reversals in both wild type animals and mechanosensation-defective mutants (G. Nagel et al. 2005). ChR2 and its enhanced derivatives have become popular tools for analysis of synaptic transmission, as well as dissection of neuronal circuits in *C. elegans* (Husson, Gottschalk, and Leifer 2013).

Recently several red-shifted photoactivatable ion channels have been discovered and optimized. One such variant, a chimeric fusion of channelrhodopsin-1 and *Volvox* VChR1, containing point mutations at E122T and E162T (C1V1-ET/ET), has been shown to induce muscle contraction in response to green light (580 nm). The same authors further demonstrated that this protein could be used in conjunction with hypersensitized ChR2 (mutagenized at H134R and T159C, termed ChR2-HR/TC) to activate muscle contraction in a mutually exclusive manner by either near UV or green light. This approach, however, necessitates the use of low-intensity light stimulation as C1V1-ET/ET is also activated by high-intensity blue light (Erbguth et al. 2012). Another approach for engineering novel ChR2 variants through mutagenesis is to continue probing natural sources for such proteins. A recent study employed large scale algal transcriptome sequencing and discovered a novel channelrhodopsin variant, which can be reliably activated by the red light. Termed ChrimsonR (CrR), it was expressed in mouse cortical slices in conjunction with a new blue light-sensitive ChR2 variant and used to independently excite distinct neural populations with light of appropriate wavelengths (Klapoetke et al. 2014).

Photoinhibitory membrane proteins can be expressed in *C. elegans* for precise light-induced hyperpolarization of neurons (Husson, Gottschalk, and Leifer 2013). There are two widely used varieties: light-gated inward Cl^- pumps and outward-directed proton pumps (Chow et al. 2010). Halorodopsin (NpHR) belongs to the former class, while Archaerhodopsin-3 (Arch) and Mac belong to the latter. Furthermore, these protein classes differ significantly in spectral properties. Mac and Arch peak activation is blue-shifted compared to NpHR (Husson et al. 2012). NpHR is activated by yellow light (580 nm and longer), while Mac, for instance, can be switched on with light wavelengths falling in between 400 and 650 nm; however, activation peak is achieved at green-blue light region (Husson et al. 2012; Waschuk et al. 2005). All of the photoinhibition proteins mentioned above require ATR for normal function (Husson et al. 2012). These proteins promise a much higher degree of flexibility for the manipulation and analysis of neural circuits than just relying on natural stimuli.

Activation of glutamate receptors produces an influx of Ca^{2+} into neuronal dendrites. This influx denotes the activation of a neuron and can be measured using genetically encoded calcium indicators. Often such proteins consist of a calcium-binding domain fused to a fluorescent protein. These proteins can generally be expressed readily in many model systems, including *C. elegans*. Furthermore, their color-type, dynamic range, and calcium sensitivity are being optimized continuously through mutagenesis (Tian et al. 2009; Zhao et al. 2011; Ohkura et al. 2012). A robust approach has been previously introduced for dissection of *C. elegans* neural networks and was used to examine reversal behaviors through stimulation of the ASH neuron and simultaneous imaging of ASH, AVA, AVD, and RIM interneurons. Calcium currents were imaged with then newly developed GCaMP2 calcium indicators. Using low-intensity blue illumination for imaging, coupled with periods of higher intensity for stimulation, authors were able to both image and excite predictably with a single wavelength of light (Guo, Hart, and Ramanathan 2009). Figure 1.4 shows an example of a toolkit for multineuronal stimulation and recording.

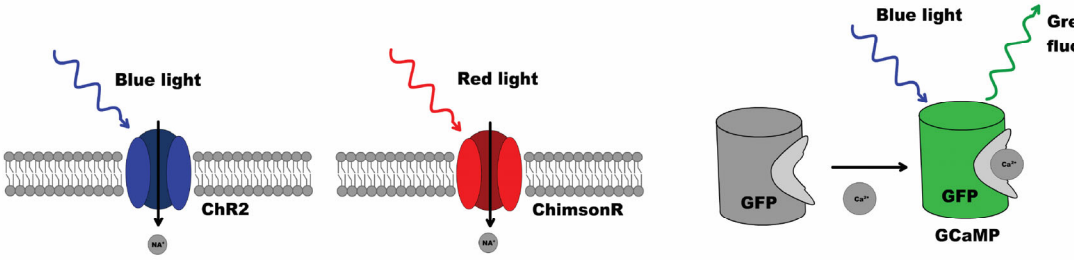

Figure 1.4 An example toolkit for two-color stimulation of neurons and readout of neuronal activity. Blue light-sensitive ChR2 and red light-sensitive ChrimsonR serve as actuators, while an intracellular calcium probe such as GCaMP allows for recording of neuronal activity.

1.6 Behavioral tracking of *C. elegans*

Animals dynamically adapt to the environment to increase the chances of survival. How it is achieved is one of the central questions of neuroscience. For a long time, the nervous system was viewed as a center of command issuing, but it is becoming

increasingly apparent that the interaction between changing environment, the body, which is subject to laws of physics and animal brain is not a top-down hierarchy, but rather a feedback loop (Chiel and Beer 1997). It thus follows that understanding the dynamics of the nervous system requires taking into account all three levels of complexity.

Historically, relatively little attention was spared for the behavior of the nematode. The view held by many researchers was that the animal, owing to its relatively simple structure, was not much more than a hardwired automaton. The focus fell more on unraveling developmental processes and biological structures. Nevertheless, this has changed with research work uncovering more sophisticated behaviors (Catharine H Rankin 2004) .

The earliest behavioral analysis for *C. elegans* was routinely performed in the context of mutant screens. The descriptions of the phenotype were broad and qualitative, such as the animal being uncoordinated or coordinated (Brenner 1974). The description list quickly expanded to include more coarse-grained descriptions such as kinky, coiling, sluggish, slow (J. Hodgkin 1983). The growing interest in understanding the sensory systems of the nematode motivated the introduction of the population assays. In this method, animals are allowed to move on the behavioral arena in response to a sensory cue for a set amount of time: temperature (Hedgecock and Russell 1975) and olfactory (C I Bargmann, Hartwieg, and Horvitz 1993). The distribution of animals relative to the cue was then determined manually. Recording of reversals of individual animals was used to study the properties of animal response to mechanical stimuli (C. H. Rankin, Beck, and Chiba 1990).

Automated behavioral tracking in the field had a slow start. The first system developed for tracking the movement of centroid of *C. elegans* was capable of monitoring ~ 25 animals at 1 Hz (Dusenbery 1985). Nevertheless, behavioral tracking was not adopted by the worm research community until the end of the 1990s. With cheaper computational costs and access to digital imaging equipment, the use of automated behavioral tracking has increased. A system capable of tracking the centroid position of approximately 50 animals was developed and used to investigate social aggregation behavior (de Bono and Bargmann 1998). Later a system was designed to track the movement speed and turning rate of individual animals during chemotaxis behavior using a motorized stage (Pierce-Shimomura, Morse, and Lockery 1999). The first standardized suit for behavioral tracking

of single animals was made available to the community in 2004, complete with software for feature extraction and classification (see Figure 1.5 A) (Feng et al. 2004; Cronin et al. 2005). This work and its derivatives have significantly increased the adoption of behavioral tracking in the *C. elegans* research community (Husson et al. 2018).

The revival of improved population tracking in the 2010s has dramatically increased the throughput of data acquisition. A system capable of collecting movement parameters of ~50 worms have been introduced as a tool for pharmacological analysis (Ramot et al. 2008). Later a multiworm tracking suit was developed for the use of researchers capable of simultaneous tracking of 120 animals and was used to analyze the spontaneous movement of animals on food in response to tapping stimulus. The software can collect animal outlines and centroid positions, while a supplemental analysis suite derives behavioral parameters (Swierczek et al. 2011).

Combining of optogenetic tools with behavioral tracking has been undertaken by several labs using different approaches. Single animal tracking and optogenetic stimulation were implemented using patterned illumination by digital micromirror devices (Leifer et al. 2011; Stirman et al. 2012) to enable stimulation of parts of the animal bodies expressing optogenetic proteins. Tracking and optogenetic control of the animal movement was demonstrated by stimulating AIY interneuron with shifting light gradients (Kocabas et al. 2012). Simultaneous tracking, optogenetic stimulation, and recording have been used to investigate the properties of the reversal response in individual animals (Faumont et al. 2011). Recently, the optogenetic stimulation with a single color of multiple animals has been shown as an extension of the multiworm tracking suit (Yu et al. 2019; Ardiel et al. 2016). Multiworm tracking has also been used with optogenetic analysis to uncover the landscape of short-term behaviors in response to random mechanosensory stimuli (see Figure 1.5 B). (Liu et al. 2018).

The behavior of *C. elegans* is fairly well understood on short timescales, owing to advances in behavioral tracking technology; however, ample research opportunities exist with multichannel stimulation on longer timescales (see Figure 1.5 C), which would require improved methods.

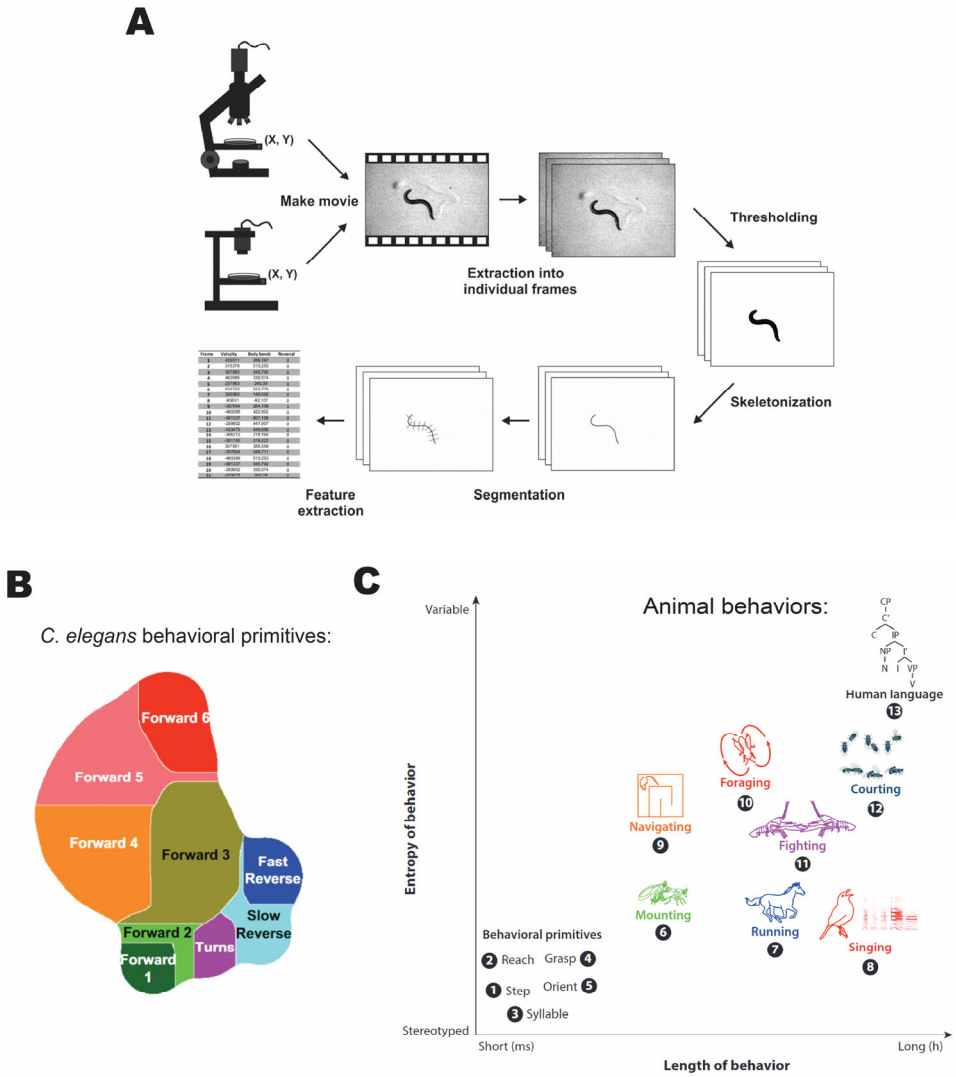

Figure 1.5 Principles of automated tracking and behavioral complexity. (A) Shows the key processes used in extracting behavioral data from animal recordings. (B) Short time scale behavioral repertoire of *C. elegans* uncovered with population tracking and optogenetic stimulation. (C) Breakdown of animal behaviors across different levels of complexity and time scales. Adapted from (Husson et al. 2018; Liu et al. 2018; Egnor and Branson 2016).

1.7 Optical microscopy for live imaging of neural activity

Capability to take into account the spatial and temporal dynamics of neuronal activity in cell populations with single-neuron resolution is essential to understanding how behavior adapts to the environment (Ji, Freeman, and Smith 2016). Recording of neuronal activity using electrodes still offers an unparalleled temporal resolution. Unfortunately, the spatial resolution, even using electrode arrays, is limited to a subset of nearby neurons (Henze et al. 2000). Neuronal activity recordings using optical imaging are significantly less intrusive and more comprehensive as light can access a vastly larger area and carry information to instruments that can be located away from the brain. Furthermore, genetically expressed calcium indicators evolve rapidly and provide an array of tools for extracting all sorts of metrics of interest, well beyond recording electrical signals (Wang, Kim, and Ting 2019). Optical methods enable the recording of neuronal communication over a large volume, which can reveal correlations, statistical properties, and large scale dynamics, that are vital to the understanding of adaptive brain function (Ji, Freeman, and Smith 2016).

The meticulous reconstruction of the whole connectome map of *C. elegans* neural system through electron microscopy (White et al. 1986) was posed to be a revolutionary step forward in understanding the nervous system function. However, decades later, its most significant achievement paradoxically was to highlight the additional complexity that is hidden behind mere connections between neurons. There are many features that are not obvious from the connectivity maps, which have been shown since to have crucial importance to animal behavior (Cornelia I. Bargmann 2012). For instance, the knowledge of connectivity graph does not inform on the polarity of the individual synapses (Rakowski et al. 2013), which can quite drastically shape the interpretation of the roles of individual neurons. Then there are neuromodulators that often not only act in the synapse locally, but can diffuse to affect neighboring connections (Hobert 2016). Additionally, mechanisms operating entirely outside the scope of connectome can have profound implications for neural computation. These include monoamine neuromodulators and neuropeptides that diffuse over vast distances and change short and long-term neuronal functions (McDiarmid, Ardiel, and Rankin 2015; Huang et al. 2017).

A way to take an integrative view of all the mechanisms that contribute to neuronal function is to determine the functional connectivity for investigated behaviors (DiLoreto et al. 2019), which could be accomplished by way of measuring the fluctuations in neuronal activity under different environmental conditions. In *C. elegans*, due to small size and transparent body as well as the relative ease of genetic manipulation, the most common way to measure neuronal activity is by using genetically encoded light-sensitive probes (Breimann, Preusser, and Preibisch 2019). Bioengineering efforts have resulted in many useful genetically encoded tools for the measurement of different aspects of neuronal signal transmission, of which the most broadly used are voltage and calcium sensors (Wang, Kim, and Ting 2019). The genetic engineering of animals carrying these proteins in the desired location has been simplified considerably by the introduction of CRISPR genome modification technology (El Mouridi et al. 2017). The introduction and refinement of these tools have greatly accelerated the progress in the neural imaging in this model system (Breimann, Preusser, and Preibisch 2019). Until recently, most published studies relied on imaging individual neurons (Zheng et al. 2012). Indeed, an impressive system, which can collect calcium dynamics from single neurons in populations of animals, while simultaneously acquiring behavioral features have been demonstrated (Larsch et al. 2015). The findings of this study also indicate that variability in behavior is more pronounced than in the recordings of neural activity motivating the development of single animal recording systems that can image the whole brain of the animal (~180 neurons simultaneously).

Systems for the whole brain imaging of *C. elegans* are in active development. The first published system, showing near 70% activity for ~5-minute recordings of all head neurons, was based on wide-field temporal focusing two-photon microscopy (WF-TeFo) (Schrödel et al. 2013). This method, however, did not see wide adoption in the community due to relatively weak signal intensities that could be obtained with low repetition laser systems. Another intriguing approach was the use of light-field microscopy (Prevedel et al. 2014). The method is compelling in that it requires no scanning, but is limited by considerable post-processing required to deconvolute imaging data for volumetric reconstruction. The more widespread approach in recent years is the use of a spinning disk confocal microscope (Nguyen et al. 2016; Venkatachalam et al. 2016). The main limitation of this approach is the use of single-photon excitation, which limits recording length in case of volumetric imaging. In spinning disk confocal microscopy, the sample is subjected

to a large number of spatially separated parallel beams scanning the imaging plane (Nakano 2002). Excitation is achieved in the one-photon regime, thus contributing to out-of-focus bleaching of the excitation volume and consequently reducing the viable imaging length (Diaspro, Chirico, and Collini 2005). The maximum reported length of recording is ~18 minutes of continuous volumetric, high-resolution imaging (Kato et al. 2015). It is conceivable that the application of two-photon spinning disk microscopy (Shimozawa et al. 2013) could resolve this problem, but the implementation of this technique is challenging. The more recent technique applied to whole animal imaging employed light-sheet microscopy (Ardiel et al. 2017). It is promising, but requires immobilization of the animals in a hydrogel to allow excitation by orthogonal plane, effectively isolating it from sensory stimuli. Out of the techniques mentioned, WF-TeFo is still the most attractive for achieving long-term high-resolution fast volumetric imaging as discussed in the following section.

1.8 Two-photon temporal focusing microscopy

The use of microscopy techniques based on two-photon excitation offers significant advantages for live imaging. Since two-photon excitation probability depends on the square of the intensity, a dramatic reduction in the background can be achieved, when compared to one-photon microscopy techniques. Additionally, tissues have lower absorption for infrared spectrum, which results in larger penetration depth and markedly reduced out of focus phototoxicity and photobleaching (Denk, Piston, and Webb 1995). In conventional two-photon microscopy, the axial confinement is primarily governed by spatial focusing, and the beam maintains a constant pulse width as it propagates along the optical axis. This is useful for scanning microscopy as the focused beam has a near-diffraction-limited spot size, which can be employed for obtaining high-resolution images. Unfortunately, the scanning speed limits the rate at which readouts can be achieved. This is particularly problematic for volumetric imaging, where short pixel dwell times limit the dynamic range (Ji, Freeman, and Smith 2016). Operating in the wide-field two-photon configuration using soft focusing of the beam has been attempted and may have advantages for particular experiments, but suffers from poor axial resolution and weak signal intensities (Amor et al. 2016).

Temporal focusing based two-photon microscopy introduces another degree of freedom, whereby the pulse duration is not fixed but depends on the distance away from

the focal plane (M E Durst, Zhu, and Xu 2008). The basic working principle is akin to that of an asymmetric 4f grating compressor (Oron, Tal, and Silberberg 2005). In ultrafast pulse compression using a double-pass grating compressor, a dispersive delay line is used to compensate for self-phase modulation (Weiner 2009). In temporal focusing microscopy, one of the gratings is replaced with an objective lens. Analogously, spectral components of an incoming pulse are spatially separated by the grating and recombined by the objective lens. According to Fermat's principle, the spatial and temporal overlap of components is realized only at the focal plane of the objective, while pulse duration outside the focal plane is subject to rapid broadening (M E Durst, Zhu, and Xu 2008).

This phenomenon significantly enhances the axial confinement offered by a nonlinear power dependence in conventional two-photon microscopy (Yew, Sheppard, and So 2013). Spatial focusing using an ideal lens results in a diffraction-limited excitation spot, offering the highest axial resolution. In the case of temporal focusing, the combination of grating and an objective, effectively create a temporal lens, whereby focusing is achieved in time rather than space. As a result, the resolution of temporal focusing microscopy is worse than point scanning microscope and is comparable to line focusing microscopy (Oron and Silberberg 2015). Intuitively, the axial resolution tends to ideal value, with shortening of excitation pulse duration. The reduction of the incoming pulse duration to sub-20 fs produces a depth of focus that is very close to 1.9 μm at 795 nm (Vaziri et al. 2008) and about twice that of point scanning two-photon microscope (Yew, Sheppard, and So 2013). Supplementing diffraction grating with an Echelle’s grating enables the generation of multifocal excitation that scans through the focal plane as the femtosecond pulse passes through the system. In this configuration, one can achieve an axial resolution comparable to point-scanning two-photon microscopy (Vaziri and Shank 2010), while retaining wide-field excitation.

While tissue exhibit low absorbance in the infrared, scattering presents significant problems for deep-tissue fluorescence imaging (Miller et al. 2017). Temporal focusing offers advantages for excitation of fluorophores inside the tissue due to inherent ‘self-healing’ properties. Owing to spatial separation of the spectral components, the beam acquires uncorrelated speckle patterns as it is propagating through turbid media. Moreover, even the adjacent components that are subject to correlated speckle maintain a spatial shift in speckle patterns resulting in anisotropic smoothing in the direction of the shift. The

combination of these phenomena enables wide-field excitation as deep as 500 μm in the scattering media. While it leads to the degradation of the axial resolution, the lateral sharpness is preserved (Papagiakoumou et al. 2013). A separate challenge is to capture the emitted fluorescence photons, that are subjected to scattering and absorption. The independent readout of adjacent neurons (~10 μm apart) has been demonstrated to result in less than 7% crosstalk within 250 μm below tissue surface using a scanless temporal focusing approach (Bovetti et al. 2017). A novel approach has been implemented recently, enabling deep tissue imaging with wide-field temporal focusing using single-pixel detection. The sample is excited using orthogonal Hadamard patterns imposed with an SLM. The spatial features are preserved due to the resilience of temporal focusing to scattering. The resulting excitation light intensity is collected for each pattern and is stored as a coefficient. The fluorescence image is reconstructed by adding all patterns weighed by respective coefficients. The authors demonstrated imaging through 400 μm of scattering medium with a lateral resolution of less than 5 μm (Escobet-Montalbán et al. 2018).

The ability of a two-photon temporal focusing microscope to excite large areas with high axial resolution, yet maintaining low out of focus phototoxicity characteristic of scanning two-photon microscopy, make it an ideal choice for fast volumetric imaging (Schrödel et al. 2013).

1.9 Problem statement and aims

This work focuses on advancing the toolkit for long-term observation and timed stimulation of live animals on behavior and neuronal levels. The overall goal is to provide the research community with better tools to perform long-term behavioral, optogenetic, and imaging experiments.

The specific aims of the project are as follows:

1. Develop and validate a neuronal imaging system capable of high throughput neuronal activity recording over long time scales.
2. Develop and validate a multicolor optogenetic stimulation system for analysis of behavior from individual to population level, capable of long-term recording.

A combination of these tools will enable the exploration of new scientific questions that were beyond the reach of current technologies.

2 Long-term neuronal activity recording with two-photon temporal microscopy with high pulse repetition rates

Contributions: sample preparation, microfluidics manufacturing, data collection, modeling, and analysis were performed by me. I thank Prof. Bala Murali Krishna Mariserla, Chakradhar Sahoo and Reuben T. Harding for help with setup design and implementation. Also Dr. Julien Madéo, Dr. E Laine Wong, and Dr. Michael K. L. Man for valuable advice on experiment design and data analysis.

Abstract

Neuronal recordings using fluorescent activity probes are routinely used in neuroscience research to study the dynamics of networks. In *C. elegans*, such experiments are performed using high-speed imaging techniques such as spinning-disk confocal microscopy. One-photon imaging techniques are not suitable for detailed recordings over long periods due to photobleaching. Recently, the wide-field temporal focused two-photon microscopy (WF-TeFo) has been applied to whole-brain imaging of *C. elegans*. WF-TeFo can potentially achieve an order of magnitude increase in volumetric recording speed owing to the use of large planar excitation area. Achieving large excitation area requires the use of laser systems capable of providing high peak power densities, at least half a millijoule per pulse, and only low repetition lasers were capable of driving pulses at such energies. The use of low repetition sources results in fluorophore saturation due to high excitation fluence as well as photobleaching. The recent introduction of high-repetition, high-pulse-energy laser systems can reduce these drawbacks by providing increased signal intensities seen in traditional two-photon microscopes and reducing the negatives of high fluence as seen in WF-TeFo setups to date. Here I use a laser system with a 100 microjoule per pulse driven at 50-100 kHz to investigate the advantages in performance achieved in WF-TeFo microscope for imaging *C. elegans* neuronal activity. I characterize the increase in signal intensity with increase in repetition rate by imaging fluorescent beads compared with a 1 kHz system and find that there is no increase in photobleaching. Indeed, increasing repetition rate and decreasing pulse intensity results in a proportional reduction

in photobleaching. As a proof-of-principle, I measure the activity of multiple neurons in live *C. elegans* over a period of 25 min in a custom-built microfluidic enclosure. Finally, I perform an analysis of steady-state temperature increase to find the optimal repetition rate. I find that repetition rates between approximately 0.5 and 5 MHz limit the rise to 1 K, which is a soft limit for *C. elegans* experiments. These findings demonstrate that the availability of high repetition rate, high-pulse-energy fiber laser systems will significantly increase the scope of neuroimaging experiments allowing for imaging longer at higher speeds.

2.1 Introduction

The demand for a more holistic snapshot of neuronal activity in live and behaving animals has spurred the development of advanced bio-optical technologies that aim to increase both the available speed and duration of imaging experiments. Use of one-photon microscopy and in particular high-speed spinning disk confocal microscopy has achieved high-speed volumetric imaging of a large number of neurons (Nguyen et al. 2016; Nichols et al. 2017), but imaging duration is constrained by the intense photobleaching resulting from one-photon excitation. Out of focus photobleaching can be reduced by the use of two-photon microscopy (Denk, Strickler, and Webb 1990). This method is minimally invasive and offers diffraction-limited resolution; however, it is limited in speed at which scanning of large areas can be implemented (Ji, Freeman, and Smith 2016). Adaptive optics can be used to extend the usefulness of this technique by producing multifocal excitation (Qu et al. 2012) and thus potentially increasing the scan speed (Abrahamsson et al. 2016). Here I make use of temporal focusing phenomenon, which allows for large excitation area that can be recorded with each exposure and offers excellent axial resolution (Yew, Sheppard, and So 2013).

Wide-field temporal focusing microscopy (WF-TeFo) is a multiphoton far-field imaging method, which enables excitation of large sample area and therefore overcomes temporal drift of the acquired signal in the lateral imaging plane. Due to broad area excitation, it potentially enables an increase in recording rate of the volumetric fluorescence signal. In this configuration, ultrashort laser pulses pass through a diffraction grating and become separated according to wavelength and then refocused in the focal plane of the objective lens. The result is the temporal focusing effect, where the shortest pulse duration is generated at the focal plane. The pulse rapidly broadens as it propagates

away from the focus of the objective (Zhu et al. 2005; Oron, Tal, and Silberberg 2005). A combination of an increase in axial confinement from the temporal focusing effect and quadratic dependence on excitation intensity enables the generation of a weakly focused excitation volume with large diameter laterally and narrow spread axially. As a result, the whole imaging plane can be excited simultaneously with low background coming from out-of-focus excitation. Since there is no need to scan pixel sequentially by pixel, the fluorescence information can be recorded in parallel from the whole area.

As the excitation area is larger than in the conventional point-scanning method, it is necessary to provide pulses with high energy for WF-TeFo. While temporal focusing microscopy originally was implemented with very high repetition laser systems in the range of ~80 MHz (Zhu et al. 2005; Oron, Tal, and Silberberg 2005), simultaneous excitation of large area required energetic pulses that are of wavelengths compatible with two-photon cross-sections of neural activity probes. Until recently, these could only be obtained at low repetition rates (~1-10 kHz), from amplifier systems. At low repetition rates, the fluorescence signal intensity can be increased by ramping up the energy per pulse. This approach, however, not only is limited by the fundamental saturation limit of the used fluorophores, but also results in increased photodamage, which is governed by a power law. The recent introduction of the new generation of fiber laser systems enable increased control over repetition rates without the necessity to realign the optical components manually and can provide highly energetic pulses (Xu and Wise 2013). The upper limit of repetition rates useful for live animal experiments is governed by thermal considerations. Tissue exposed to high average power excitation absorbs a fraction of incident light, which results in a local temperature increase, which leads to degradation of tissue components and changes in vital processes (Podgorski and Ranganathan 2016). An optimal balance between excitation intensity and pulse repetition rate can be selected to maximize the fluorescence signal while staying within the tolerance limit for a particular experiment (Denk, Piston, and Webb 1995).

In this chapter, I demonstrate improvements in the magnitude and persistence of the fluorescence signal by changing the repetition rate and peak power density of the excitation source. I establish the optimal combination using volumetric imaging of fluorescent beads and modeling of steady-state temperature increase. Findings are validated by performing neural activity recordings of live immobilized *C. elegans* expressing fluorescent

intracellular calcium probe. I show that the increase in laser repetition rate while staying below temperature limits, offer large improvements in signal strength and persistence.

2.2 Materials and methods

2.2.1 Configuration of the temporal focusing microscope

WT-TeFo microscope was designed and constructed following the previously published reports (Zhu et al. 2005; M E Durst, Zhu, and Xu 2008; Schrödel et al. 2013). Two laser systems were used for excitation. The reference laser, high energy, and low repetition rate system (Spitfire, Spectra-Physics) was tuned to yield, 1 mJ pulses at 1 kHz repetition rate with a central wavelength set at 800 nm and yielded 75 fs pulses. The optimal wavelength for two-photon excitation of fluorophores used in these experiments was 960 nm. The 800 nm output from the laser system was converted to 960 nm central wavelength using an optical parametric amplifier (Topas, Light Conversion). The test laser system (Wyvern, KMLabs), which was to substitute a high-repetition high-pulse-energy fiber laser source, was set to yield 50/100 kHz output with pulse energies of 100 μJ, providing pulses at 800 nm central wavelength with a duration of 45 fs. The central wavelength was converted to 960 nm using an optical parametric amplifier designed for high repetition (TopasHR, Light Conversion). A flip mirror was placed in the optical path to enable fast switching between the two laser systems. The average power control was implemented using a reflective neutral density filter wheel (ND 0.04 to 4, Thorlabs). In general, the average power at the neutral density was bellow ~50mW spread out in a beam diameter close to ~1 cm. Under this condition, I did not observe any adverse effects on imaging. The beam then entered the temporal focusing core composed of a high groove density reflective diffraction grating (1200 lines/mm, Thorlabs), a collimating relay lens (with a focal length of 500 mm, Newport Corporation) and a microscope objective (UPLFLN 40XO, Olympus). An inverted microscope (IX71, Olympus) was used to house the high-speed piezo scanning stage (Nano-Z50HS, Mad City Labs Inc.), the objective and the detector. Figure 2.1 shows the setup diagram and example of a volumetric capture of the beads.

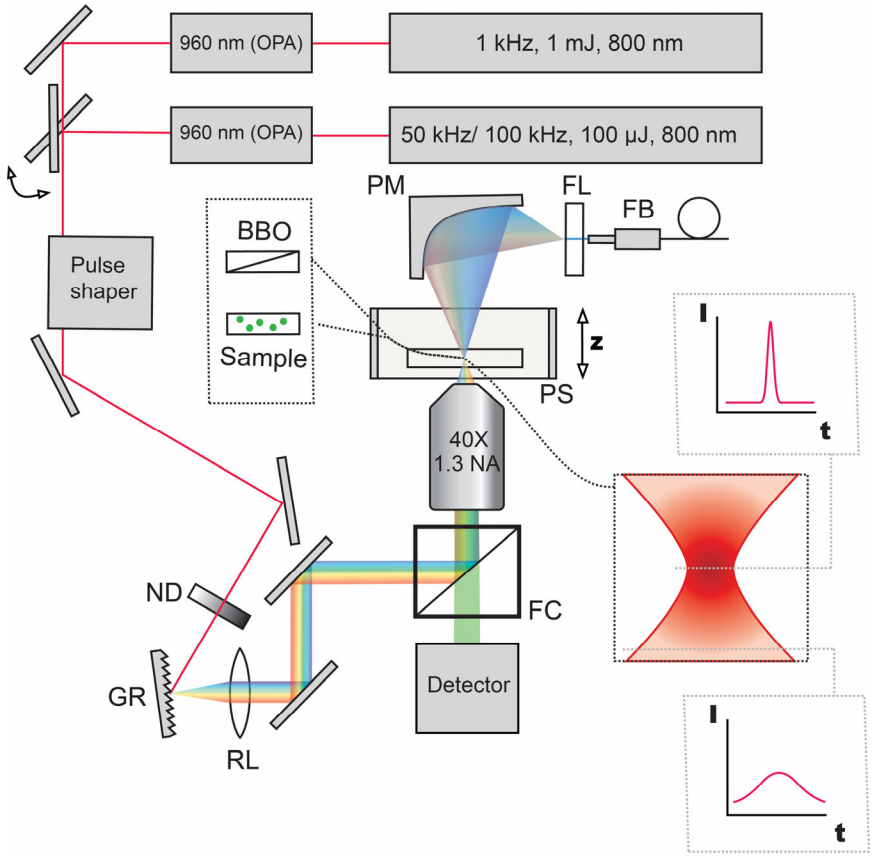

Figure 2.1 WF-TeFo setup diagram with switchable lasers and pulse shaping capabilities. The beam from two lasers with different repetition rates are aligned in a common path and switched between with a flip mirror. Pulse shaper was calibrated to accept either of the two beams. A discrete neutral density filter wheel (ND) was installed to change the power of optical excitation on the sample. Temporal focusing was implemented with a diffraction grating (GR), a relay lens (RL), and a 40X objective. A filter cube (FC) was used to image in the epifluorescent configuration. Samples (BBO, beads, or live animals) were mounted on a high-speed piezo stage (PS) for imaging. In pulse characterization experiments, the second harmonic signal was collected by a parabolic mirror (PM) and, prior to coupling into the pulse shaper's fiber spectrometer, was separated from the fundamental by an absorptive filter (FL). Adapted from (Lisicovas et al. 2019).

A filter cube was used to separate the fluorescence signal from two-photon excitation in an epifluorescent configuration. It was composed of a long-pass filter with a

cut-off wavelength at 800 nm, a dichroic mirror reflective in the near-infrared range, and transmissive for visible light in the range between 675 nm and 500 nm and a short-pass filter with 575 nm cut-off. In this configuration, infrared light coming from the diffraction grating is reflected towards the sample, while the generated epifluorescent signal is transmitted towards the detector. In the experiments presented below, fluorescence signal detection was accomplished with a high-speed, high-resolution CMOS camera (Zyla 5.5 with a 10-tap data transfer connector, Andor Technology). In all experiments, only a part of the sensor was used to collect the fluorescence signal. The resolution on the detector was determined to be 6.2 pixels/μm (10 μm microscope calibration slide, Olympus). The power of the laser beam after the objective lens was measured using a microscope slide power meter (S175C, Thorlabs). Pulse duration after the objective was measured and compressed to a transform-limited pulse duration using a pulse shaper with an integrated spectrometer (MIIPS Box 640, Biophotonics Solutions). When measuring pulse duration, a microscope slide with a mounted beta barium borate nonlinear crystal (BBO, EKSMA Optics) was placed in the focal plane. A parabolic mirror (focal length of 50 mm) and an absorptive filter (short-pass with 575 nm cut-off, Newport Corporation) placed above the sample was used to collect the second harmonic signal generated by the BBO. Using the pulse shaper, I have characterized the incoming pulse for both 1 kHz and 50/100 kHz (see figure 2.2).

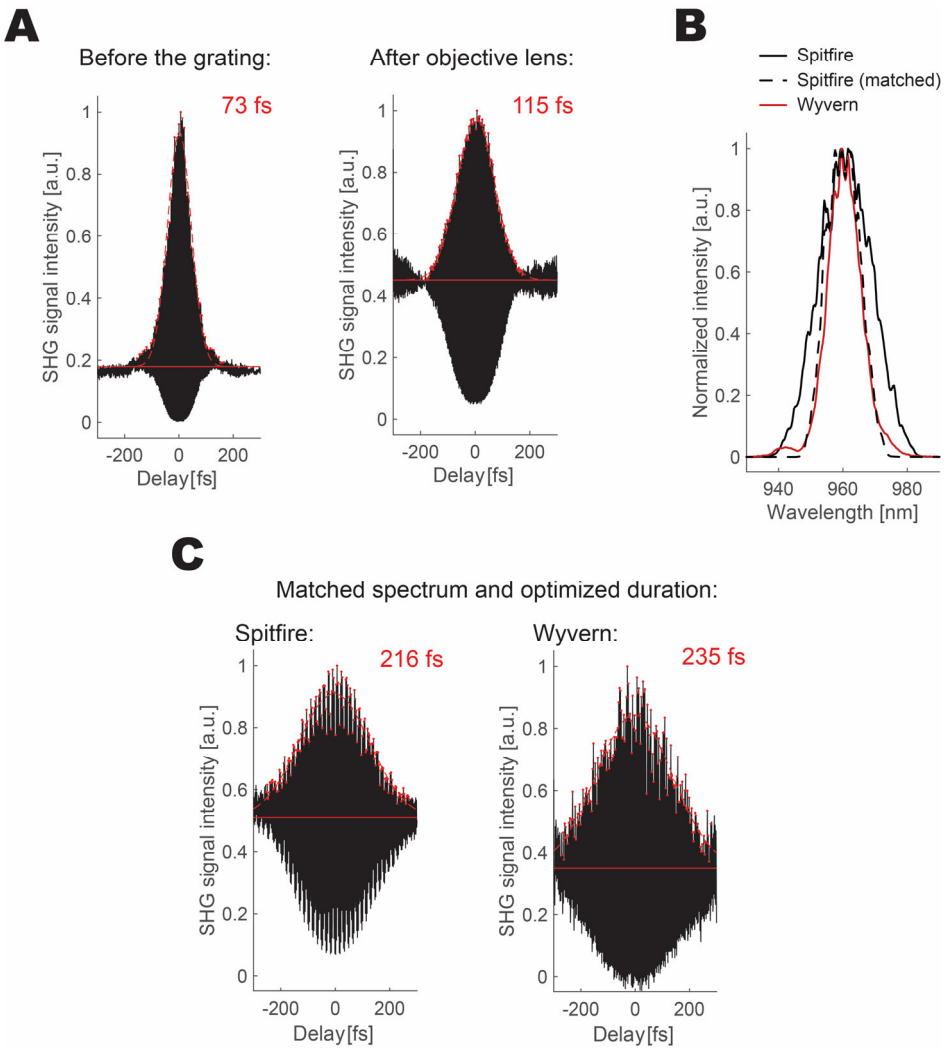

Figure 2.2 Pulse characterization and manipulation. (A) Optimized pulse duration measured before the grating and after the objective lens using the pulse shaper for the Spitfire system (1 kHz). (B) Equalization of pulse spectral bandwidth of the two laser systems using the pulse shaper. (C) Pulse duration measured for the two laser systems after optimization shows comparable pulse durations.

I found that a pulse shaper could not be used in the current implementation to precisely determine the pulse duration at the focus. This is likely due to BBO crystal being thicker than the focal depth (100 µm). The second harmonic signal coming from out of focus regions may have contributed to measured longer pulse durations. Nevertheless, pulse shaper was instrumental in equalizing the spectral bandwidth between the two

systems and reshaping the pulses to Fourier transform limited durations. Measurement for both systems after the above optimization shows similar pulse durations, indicating parity between laser systems.

2.2.2 Preparation of the microfluidic devices

Here, I have explored a novel approach for rapid manufacturing *C. elegans* microfluidics devices, in 2.5 dimensions. With this approach, a new design can be implemented in less than 24 hours from a blueprint to a functional device and with high accuracy. The key improvement in the traditional process is the mask preparation, which was performed as follows. The silicon substrate surface was prepared by cleaning with acetone and isopropanol for 10 min each in an ultrasound bath. A plasma cleaner was then used to treat the surface. Salinization of the silicon surface was then performed using 25mL of ethanol, with 125 µL of 3-(trimethoxysilyl)propyl methacrylate (Sigma) with 750 µL of 1:10 dilute acetic acid added just before submersion of the silicon wafer. The coating is allowed to progress in ultrasound bath for 10 min, after which the substrate was rinsed with ultrapure water (MiliQ) and blow-dried with nitrogen gas. The substrate was then immediately coated with IP-S photoresist (Nanoscribe) and mounted in the 3D printer (Photonics GT, Nanoscribe). Following the printing process, the microfluidics mask should have excellent surface adhesion, and the coated silicon portion should be hydrophobic, two features essential for successful PDMS molding. From here on, a standard method was applied for manufacturing of the devices (Friend and Yeo 2010). Devices manufactured in this fashion have superb resolution and support smooth variations in profile in 3 dimensions, as long as the base features are wider than top.

2.2.3 Preparation of imaging samples

To simplify the comparison between different excitation conditions, I have elected to use fluorescent beads (Fluoresbrite® YG Microspheres, Calibration Grade 1.00 µm, Polysciences, Inc.) as a surrogate for the green fluorescent protein (GFP). GFP serves as a basis for many popular genetically expressed neuronal activity probes, including versions of high-affinity Ca^{2+} probe composed of a single GFP (GCaMP) (Akerboom et al. 2012; Nakai, Ohkura, and Imoto 2001).

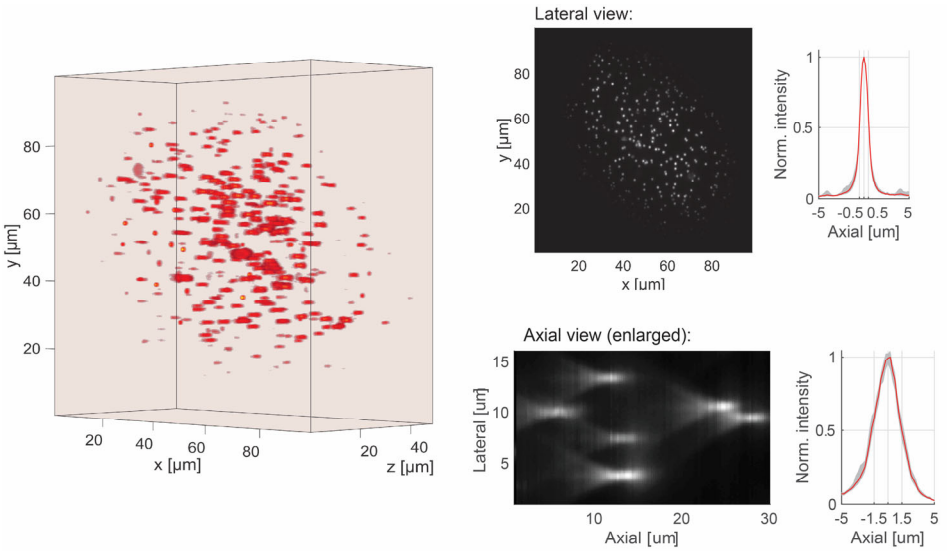

Figure 2.3 Volumetric imaging of beads with the WF-TeFo setup. Grayscale maximum projection image of the beads to illustrate the accessible area and a volumetric plot to demonstrate axial sectioning capabilities. The flattened lateral and axial views illustrate the typical resolution available with the current WF-TeFo setup. Measured full-width-half-max of the signal intensity in the lateral direction was ~1 µm (n = 59) and in axial direction was ~3.3 µm (n = 28). Profiles extracted from volumetric scans were normalized. The red line represents the mean and shading corresponds to bootstrapped confidence interval (α=0.05). Adapted from (Lisicovas et al. 2019).

Fluorescent beads sample was prepared by fixing stock suspension with an aqueous polyacrylamide crosslinking agent (Crosslinking Reagents and Catalysts 29:1, Bio-Rad). The resulting mixture was then quickly transferred to a cutout silicon mold (Silicone Isolators™, Grace Bio-Labs) sandwiched by a glass microscope slide and a coverslip. After polymerization, nail polish was applied around the seams to prevent evaporation. Figure 2.3 shows the volumetric image of the beads with the temporal focusing setup.

To ascertain that fluorescent beads can be used as a surrogate sample, I have measured the fluorescence lifetime and excitation spectrum using time-resolved spectroscopy (Streakscope, Hamamatsu). Results suggest that current fluorescent beads approximate well GFP both in terms of excitation spectrum and fluorescence lifetime. The

measured lifetime was 2.51 ns for the beads and ~2.4 ns for GFP (Husson et al. 2012). Figure 2.4 presents the results obtained by time-resolved spectroscopy.

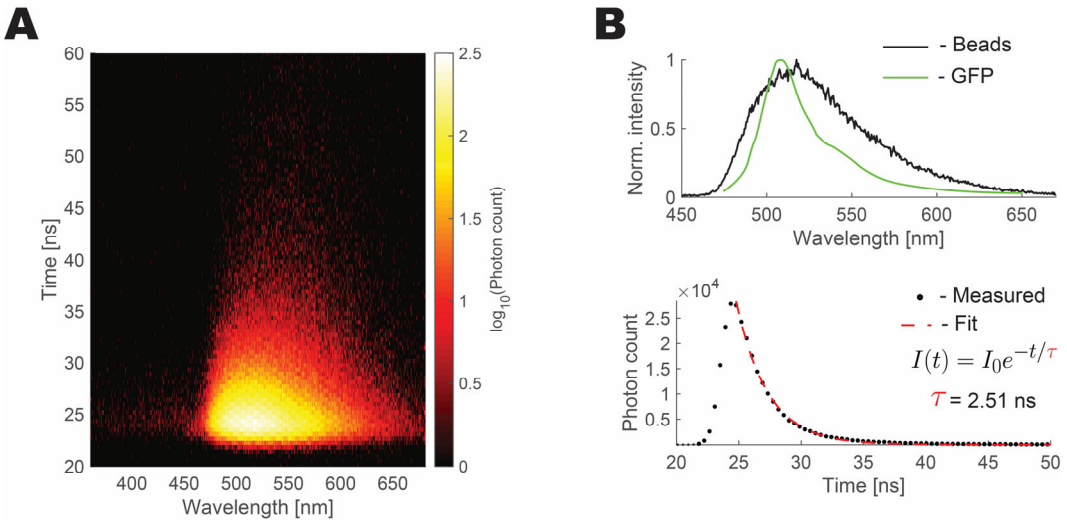

Figure 2.4 Fluorescent beads mimic the excitation spectrum and fluorescence lifetime of GFP. (A) Raw photon counts obtained from time-resolved spectroscopy experiment. (B) The excitation spectrum in comparison to GFP and measured fluorescence decay and the fit used to extract fluorescence lifetime.

Live animal experiments were performed with *C.elegans* cultured under standard cultivation conditions (Brenner 1974). In all live imaging experiments, I have used the LX2004 strain (*lite-1(ce314); vsIs183; lin-15(n765ts) X [nlp-3::GCaMP5G]*) with an integrated expression of GCaMP5 driven by *nlp-3* promoter (Collins et al. 2016). Animals were physically immobilized as described above using standard M9 medium (Stiernagle 2006) as the default liquid environment. 1M glycerol solution was prepared in M9 medium to stimulate aversive ASH neuron. Pure chemicals were sourced from Nacalai Tesque, Inc. Microfluidics channels were connected to tubing using stainless steel pipes, and liquid flow was controlled by a system of magnetic valves (VC-6, Warner Instruments), synchronized by the computer. Gravity and negative pressure applied to the outlet channel were used to maintain the liquid flow.

All experiments with fluorescent beads were performed at 50 ms exposure time with 1 µm steps between slices, while live animal experiments were done at 30 ms exposure per slice with 5 µm steps. I have measured the lateral and axial resolution of the

microscope using a fluorescent bead sample sectioned at 0.25 μm steps. After background subtraction, individual intensity traces were normalized, aligned, and the mean was analyzed. The resolution was inferred from full-width-half-max of the resulting normalized intensity distribution. Using this method, the calculated axial resolution was determined to be ~3.3 μm and is in agreement with previously published data (Vaziri and Shank 2010). The precise lateral resolution could not have been determined due to the use of large calibration beads. The measurement, however, recovered the diameter of ~1 μm (see Figure 2.3), which indicates that the lateral resolution is, in fact, better. Overall, these results are in agreement with the theoretical resolution of WF-TeFo, which corresponds to that of a line-scanning two-photon microscope (M. E. Durst, Zhu, and Xu 2008; Oron, Tal, and Silberberg 2005). In all experiments, only a part of the imaging detector was used to collect intensity information. The scale of the image on the sensor was measured to be 6.2 pixel·μm^{-1} (using a 10 μm calibration sample, Olympus). Custom Matlab (Mathworks) scripts were written to interface with the camera and analyze the acquired imaging data. The raw data had background subtracted, and all fits were performed with a native curve fitting toolbox in Matlab. Statistics were calculated using non-parametric resampling methods from the statistical toolbox (bootstrapping) to obtain confidence intervals. Additionally, live animal GCaMP5 fluorescence change measurements were analyzed using Fiji software to extract baseline relative fluorescence change (Schindelin et al. 2012). Data from discrete slices were de-noised and converted into a volumetric representation. The position of neurons was then annotated and used to extract fluorescence change over time.

2.3 Results

2.3.1 Fluorescence signal intensity scales linearly with the repetition rate

In optical microscopy, photons carry information about the system. The number of photons and how efficiently they can be detected is what determines the information bandwidth transmitted from the sample. It is a critical consideration for multiphoton microscopy especially, as the excitation/emission process produces a relatively small number of photons with a power-law dependence on excitation intensity (Lefort 2017). The rate of image acquisition is constrained by the number of photons that can be captured by the detector in one exposure cycle. The number of emitted photons can be increased by

increasing the excitation intensity, but this proves beneficial only until all the fluorophores become saturated. On the other hand, increased repetition rate would generate more fluorescent photons linearly as long as fluorophores have sufficient time to drop to ground state in between pulses (Denk, Piston, and Webb 1995).

To verify that the collected signal increases linearly with increase in repetition rate, I have performed two-photon imaging of fluorescent beads with either 1 kHz or 50 kHz repetition rate, varying the applied peak power density. Peak power density is defined as the power delivered by a pulse at its peak divided by the area of the beam waist, or in effect, intensity per pulse. These experiments confirm that obtained fluorescence signal intensity scales quadratically with peak power density for both repetition rate. In case of 1 kHz, sufficient power was available to illustrate the saturation of fluorescence signal (peak power density above $5 \cdot 10^{11}$ W·cm^{-2}), which leads to abrupt deviation from the quadratic relationship. The rate of rising of the fluorescence signal with peak power density shows a rough proportionality with repetition rate (i.e., $a_{50kHz} = 2.1 \cdot 10^{-18}$ W^{-2}·cm^{-4} vs. $a_{1kHz} = 3.2 \cdot 10^{-20}$ W^{-2}·cm^{-4}). Figure 2.5 shows the experimental data and fits.

The measured saturation threshold is in agreement with previously published values for conventional two-photon microscopy (Diaspro and Chirico 2003). Indeed, the best stability of the fluorophores is achieved when exciting below the saturation regime. It is, therefore, beneficial to increase the pulse repetition rate instead to achieve improvements in fluorescence signal.

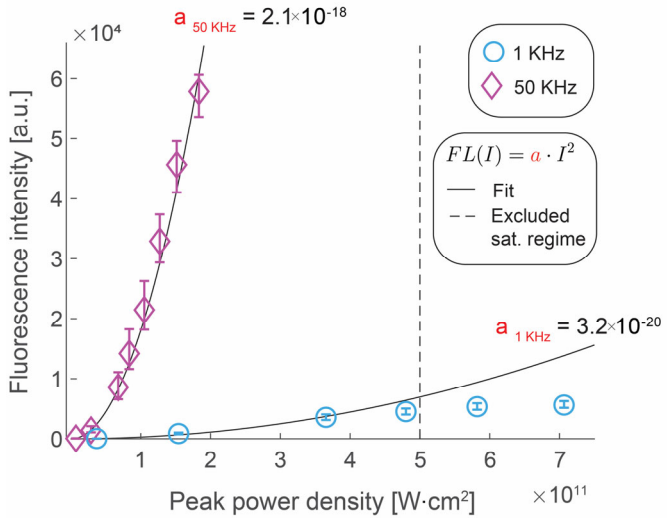

Figure 2.5 Increased repetition rate results in proportional gains in fluorescence intensity. Fluorescence intensity increase as a function of peak power density is shown for 1kHz (circles) and 50kHz (diamonds). Black lines represent quadratic fits with a single fitting variable (1 kHz, $R^2 = 0.97$, 50 kHz, $R^2 = 0.99$). Note that data points beyond the saturating peak power density were excluded from fitting. Error bars show bootstrapped confidence intervals calculated at $\alpha = 0.01$ confidence level. Data derived from n = 117 (1 kHz) and n = 41 (50 kHz) measurements of fluorescent beads within the 10^{th} percentile of the area around the excitation beam intensity peak. Adapted from (Lisicovas et al. 2019).

2.3.2 Photobleaching accelerates faster with increased intensity than with repetition rate

Having established that an increase in fluorescence signal can be obtained with increased repetition rate as well as to a smaller degree, with higher pulse intensity, I sought to compare how variations in these parameters affect photobleaching of fluorophores. Photoinduced damage is an essential consideration for any light-based measurement technique. This is especially true for two-photon microscopy excitation schemes, with the requirement of very high peak power densities. While fluorophore stability depends on chemical makeup and surrounding environment, in general commonly used organic

fluorophores at room temperature can undergo only a limited number of excitation cycles before permanent depletion (Diaspro et al. 2006). Elevated temperature or high-intensity electromagnetic fields accelerate the breakdown of fluorophores (Chirico et al. 2003). High excitation intensities promote higher-order excited states resulting in increased reactivity and breakage of covalent bonds (Diaspro et al. 2006). The severity of damage scales as power law with illumination intensity (Kalies, Kuetemeyer, and Heisterkamp 2011). Since in a typical WF-TeFo setup, intensity is distributed in a Gaussian over the excitation area, the bleaching in the center and the periphery are not equal. Thus using high peak power density excitation complicates the analysis and interpretation of acquired intensity information, especially when considering relative intensity changes over time.

To test how photobleaching characteristics change with an increase in intensity and repetition rate, I have measured the rate of photobleaching from fluorescent beads under varied conditions. These experiments show that increase of peak power density expedites the photobleaching process independent of the repetition rate used. While bleaching data collected for 1 kHz or 50 kHz result in similar photobleaching rate within the measurement error, the intensity of the fluorescent signal averaged over time is significantly higher. The loss of fluorescence due to photobleaching is well approximated with a double exponential decay function (Kalies, Kuetemeyer, and Heisterkamp 2011). The amplitude weighted average of the two decay rates follows a second-order power law for both repetition rates measured. This behavior is similar to the scaling of photobleaching rate in GFP (Chen et al. 2002). Figure 2.6 presents the photobleaching measurements and associated fits.

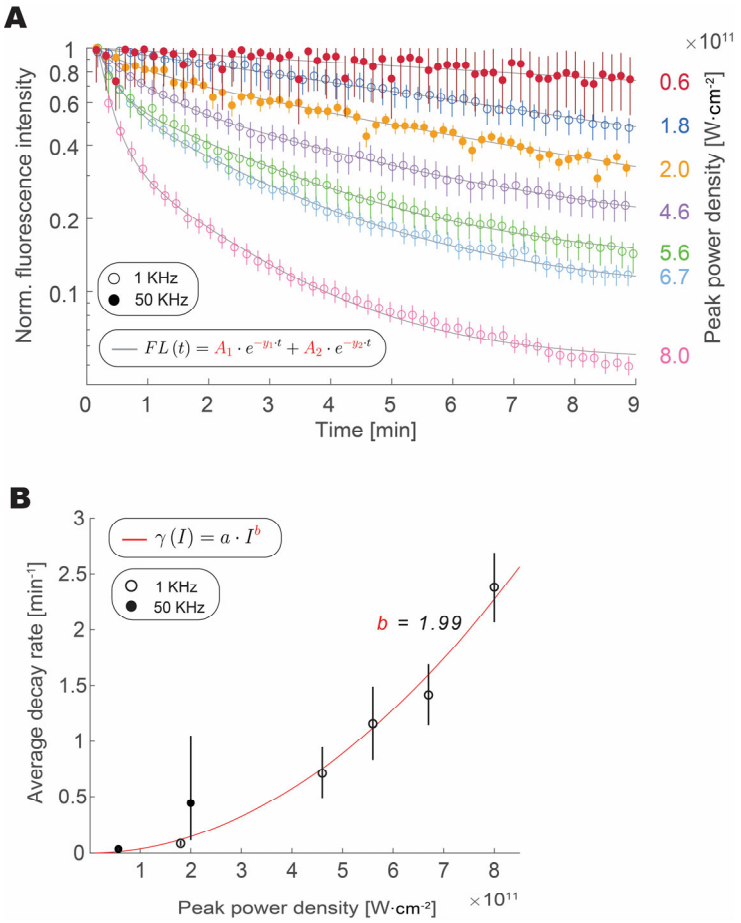

Figure 2.6 Effect of increase in intensity and repetition rate on photobleaching time. (A) Reduction of fluorescence intensity with continuous illumination. Average fluorescence intensity values for beads were extracted from the 10th percentile of excitation area with maximum intensity of the incident excitation beam and normalized for plotting. Intensity values are normalized by respective maximum intensity of the time series recorded at the start of the experiment to emphasize photobleaching rate and facilitate comparison between different conditions. Curves are shown for different repetition rates (circles for 1 kHz and full circles for 50 kHz) and varying peak intensities (color-coded). (B) Amplitude weighted average decay rate plotted versus increasing peak power density. Here 1 kHz (empty circles) and 50 kHz (full circles) were fitted with a power-law function ($R^2 = 0.96$). Error bars denote bootstrapped confidence intervals calculated at $\alpha = 0.01$ confidence level. Measured from n = 157–214 (1 kHz) and n = 32–56 (50 kHz) fluorescent beads. Adapted from (Lisicovas et al. 2019).

An increase in repetition rate results in more photons generated from fluorescence over unit time, without altering the photobleaching rate. If the intensity of the excitation is reduced in balance with an increase in repetition to maintain equivalent fluorescence intensity, it is possible to extend the recording time before complete loss of signal. To demonstrate this I have used the fits derived in figures 2.5 and 2.6 to obtain the ratio of average decay rates at peak power densities that produce equivalent fluorescence intensity according to the following relationship:

$$\frac{\gamma_{50kHz}}{\gamma_{1kHz}} = \left(\frac{I_{50kHz}}{I_{1kHZ}}\right)^{\frac{1}{2}\cdot b} = \left(\frac{\alpha_{1kHz}}{\alpha_{50kHZ}}\right)^{\frac{1}{2}\cdot b} \simeq \frac{\alpha_{1kHz}}{\alpha_{50kHZ}} \qquad 2.1$$

A measured decrease of 98.4% in the photobleaching rate was obtained by ramping the repetition rate 50-fold while maintaining equivalent fluorescence intensity.

2.3.3 Modeling of temperature constraints suggest an optimal repetition rate in the vicinity between 0.5 and 5 MHz

Subjecting biological tissues to high excitation intensities result in adverse effects. Sufficiently strong electromagnetic fields can lead to dielectric breakdown of the tissue components and are routinely employed for precise tissue ablation, notably in ophthalmology (Callou et al. 2016). However, even at moderate peak power densities, effects ranging from elevated tissue temperature to changes in cellular metabolism and, in the case of neurons, changes in neural activity patterns do occur (Podgorski and Ranganathan 2016). Since measurement of temperature increase due to laser-induced heating inside living tissue is technically complicated, rigorous modeling of complex excitation schemes has received considerable attention. Published reports have employed different computational approaches: using Monte Carlo simulations (Podgorski and Ranganathan 2016; Stujenske, Spellman, and Gordon 2015) and, more recently, an analytical solution for three-dimensional Fourier heat flow equation through use of Green's functions (Picot et al. 2018).

Increase in repetition rate, while maintaining peak power density constant, necessarily leads to more average power being dumped into the tissue. Due to tissue not being completely optically transparent for excitation wavelengths, this results in temperature build-up at the excitation region (Yang and Miklavcic 2005). Since there are

significant improvements in signal intensity resulting from increased repetition rate, I sought to estimate the limiting repetition rate. The laser system capable of delivering sufficient peak power densities over large areas at my disposal was limited to 100 kHz. This configuration did not result in any perceptible heating effects when applied to live animal imaging, as judged by the absence of change in animal behavior during prolonged exposure with reduced immobilization. *C. elegans* is acutely sensitive to localized temperature stimulus, showing instantaneous reversals with increases in temperature as low as 0.1 K (Mohammadi et al. 2013). I thus attempted to model the heating process as a function of excitation parameters to estimate the upper bounds on viable repetition rates for imaging of biological tissues.

Since the geometry of the excitation beam in WF-TeFo is relatively simple, I have opted to model the problem as a heat source imbedded in idealized brain tissue, saturated with GFP based fluorescence emitters. The excitation beam is shaped by a combination of spatiotemporal dispersion, loose-focusing, and an objective with a high numerical aperture to converge rapidly towards the focal plane over large areas (M E Durst, Zhu, and Xu 2008). Excitation intensity decays rapidly outside the Rayleigh length away from focus. It is thus not unreasonable to approximate the excitation beam incident on the tissue as a cylindrical heat source. This approach draws from previous estimates of heat accumulation in point-scanning two-photon microscopy, but, naturally, assumes different excitation beam geometry (Denk, Piston, and Webb 1995).

In order to further reduce the complexity, the model formulation assumes the excitation area is a cylinder with the radius equal to full-width-half-max of the intensity distribution in the lateral plane and the height of which is constrained by Rayleigh range. This region is where the sample is subjected to highest intensities of incoming excitation light. The heat accumulation, due to tissue absorption can dissipate to surrounding tissue laterally, but diffusion is restricted by beam geometry axially. Further, I assume that all photons absorbed by the tissue are converted to two-photon emission, or the energy is dissipated as heat. All higher-order absorption events are considered negligible. The Rayleigh length for the one-photon absorption process is on the order of 250 μm when using a high magnification and high numerical aperture objective lens. In comparison, two-photon absorption is confined to a Rayleigh length of close to 2.5 μm due to temporal focusing effect. Given that tissue absorption coefficient in one-photon regime is low and the path length is short, the total one-photon absorption can be approximated to scale

linearly with path length. Since heat dissipation is assumed to progress predominantly in the lateral direction, the model will predict a uniform temperature distribution for each axial slice of the excitation cylinder. The notable exception is the focal region, which also receives a contribution from two-photon absorption. This region, therefore, will reach the highest steady-state temperature. To define conservative bounds for average power that can be safely applied to the sample, I limit this analysis to the dimensions of the excitation cylinder constrained by two-photon Rayleigh length for contributions of both one- and two-photon processes. Table 2.1 lists all the variables used in the model definition.

Table 2.1 Modeling parameter and variable definitions

Model Param.	Description	Values and Units	References
F_a	The fraction of absorbed photons that do not result in two-photon emission	—	—
N_a	Number of absorbed photons	—	—
N_τ	Total number of photons	—	—
$N_{1\lambda}$	Number of photons absorbed due to one-photon absorption of the medium	—	—
$N_{2\lambda}$-N_{em}	Number of absorbed photons that do not result in two-photon emission	—	—
μ_a	Absorption coefficient	1 cm^{-1}	(Jacques 2013; Yaroslavsky et al. 2002; Johansson 2010)
d	Propagation length (two Rayleigh lengths)	5 μm	—
I	Peak power density	$W \cdot cm^{-2}$ (approx. equal to $4.3 \cdot 10^{35}$ photon$\cdot cm^{-2} \cdot s^{-1}$)	—
S	Coherence parameter	—	(Birge 1986)
$\delta_{2\lambda}$	Two-photon cross-section at 960 nm	31×10^{-50} $cm^4 \cdot s^{-1} \cdot$molec.$^{-1} \cdot$photon^{-1}	(Akerboom et al. 2012)
C	Typical concentration of fluorophores	6×10^{18} molec.$\cdot cm^{-3}$	(Drobizhev et al. 2011)
λ	The wavelength used for two-photon imaging	960 nm	—
h	Planck constant	$6.62607015 \cdot 10^{-34}$ J$\cdot$s$\cdot$photon^{-1}	—
c	Speed of light in vacuum	299,792,458 $m \cdot s^{-1}$	—
Φ	Quantum efficiency	0.67	(Akerboom et al. 2012)
ε	Heat source	$J \cdot m^{-3}$	—
P_A	Average laser power	W	—
V	The volume of the excitation cylinder	μm^3	—
q_r	Heat	J	—
T	Temperature	K	—
k	Specific thermal conductivity of brain tissue	0.5918 $W \cdot K^{-1} \cdot m^{-1}$	(Ponder 1962) (Poppendiek et al. 1967)

With these considerations in mind, the fraction of absorbed photons from a Gaussian shaped pulse can be expressed as the sum one and two-photon absorption contributions:

$$F_a = \frac{N_a}{N_\tau} = \frac{N_{1\lambda} + (N_{2\lambda} - N_{em})}{N_\tau} = (1 - e^{-\mu_a \cdot d}) + (I \cdot S \cdot \delta_{2\lambda} \cdot C \cdot d \cdot \frac{\lambda}{hc}) \cdot \left(1 - \frac{\Phi}{2\sqrt{2}}\right). \quad 2.2$$

Note that this expression is valid only if the fluorophores have sufficient time to return to the ground state in between pulses. If the tissue is considered to be a set of

infinitesimally small cells, then the primary mode of heat transfer is conduction rather than convection or radiation. Metabolic heat and blood circulation are not included in this analysis, since it is not a strong contributor for tissue cooling under given conditions (Elwassif et al. 2006; Stujenske, Spellman, and Gordon 2015; Picot et al. 2018). The source term is defined as a uniform cylindrical heat source encompassed by an infinite heat sink as follows:

$$\varepsilon = \frac{P_A \cdot F_a}{V}. \tag{2.3}$$

The balance of heat conduction from some radial distance r to $r + \Delta r$ can be expressed as:

$$|2\pi r d \cdot q_r|_r - |2\pi r d \cdot q_r|_{r+\Delta r} + 2\pi r \cdot \Delta r \cdot d \cdot \varepsilon = 0. \tag{2.4}$$

The expression for q_r is obtained by taking the limit of $\Delta r \rightarrow 0$ and integrating the resulting expression while taking into account that q_r is finite at $r = 0$:

$$q_r = \frac{\varepsilon \cdot r}{2}. \tag{2.5}$$

The heat flow balance at an arbitrary r can be found by using Fourier's law as follows:

$$-k \frac{dT}{dr} = \frac{\varepsilon \cdot r}{2}. \tag{2.6}$$

With the assumption that the surrounding of the cylinder is an infinite thermal sink ($T = T_0$, when $r = R$), integration of the above equation results in:

$$\Delta T = \frac{\varepsilon \cdot R^2}{4 \cdot k}. \tag{2.7}$$

With the values given in table 2.1, the amount of average power that can be applied to a tissue sample for a physiologically moderate temperature increase is predicted to be close to 100 mW. Figure 2.7 shows the schematic depiction of the model and predicted steady-state temperature increase at different average powers and peak power densities.

While the temperature effect is negligible at lower peak power densities, the two-photon contribution accounts for close to ~25% temperature increase at the focal plane at near saturating peak power density. This result is, of course, only valid under the assumption that axial heat diffusion can be neglected.

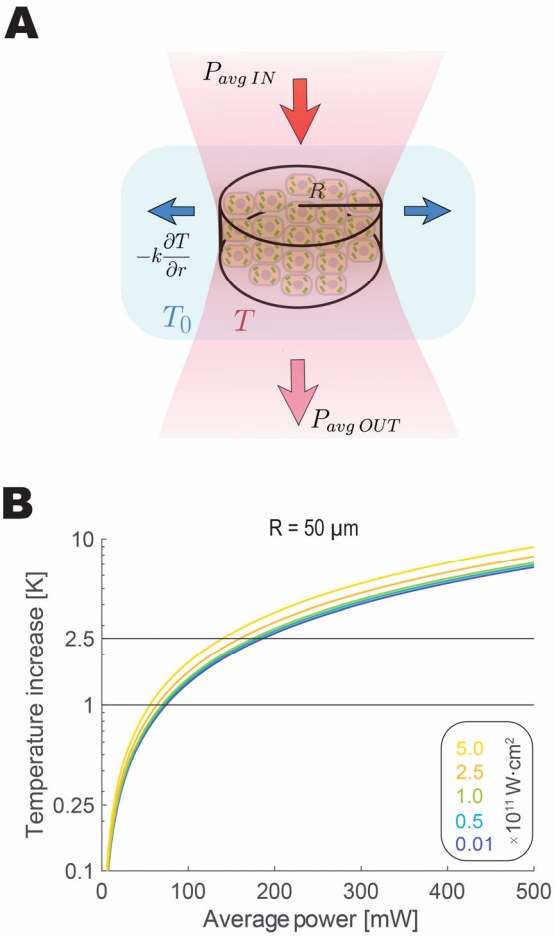

Figure 2.7 Temperature dissipation model. (A) Schematic depiction of the steady-state lateral heat dissipation in an idealized tissue under temporal focusing excitation. (B) Steady-state temperature increase scaling with applied average power for a 50 µm radius excitation spot. Adapted from (Lisicovas et al. 2019).

To test how the predictions of this simple model compare to previously published results for two-photon scanning microscopy, I have used the limit case from the report, where scanned area was the size of the excitation spot. The following conditions were used in the simulation: excitation was performed with 200 mW of average power, at 920 nm

with 80 MHz repetition rate, and 120 fs pulse duration; loose focusing resulted in 7 μm beam spot radius at a depth of 250 μm. Under these conditions, assuming the worst-case scenario of highest reported absorption (0.19 mm^{-1}) for brain tissue and lowest scattering (0.55 mm^{-1}) (Jacques 2013; Yaroslavsky et al. 2002; Johansson 2010), the model predicts a temperature increase of 6.2 K. In this case, the photons lost en route to focal plane due to absorption or scattering are not included in the heat calculation since the intensity is not high, and the area is dissipated over a large volume. The obtained prediction is consistent with previously published results (Podgorski and Ranganathan 2016).

I then looked for the optimal combination of pulse peak power density and repetition rate to achieve best imaging results under the thermal constraints. Photobleaching experiments indicate that the use of high peak power density is not advisable due to rapid increase in photobleaching. Setting the peak power density at 10% of the saturation limit in my experiments results in low fluorophore degradation, but still sufficient signal intensities for imaging. Under this condition, setting the thermal limit at an increase of 1 K to avoid thermal effects on tissue reduces the function to a single variable, which is the radius of the excitation spot. For spot diameters commonly reported in the literature (25 to 100 μm), the optimal excitation pulse repetition rate ranges from roughly 0.5 to 5 MHz. This result coincides with the typical repetition rates of the new generation fiber laser systems capable of delivering sufficient peak power densities over large imaging areas. Figure 2.8 presents the modeling results as a function of applied peak power density and repetition rate. Note that an order of magnitude more photons can be gathered by increasing excitation source repetition rate, which should translate to similar gains in achievable volumetric imaging speed.

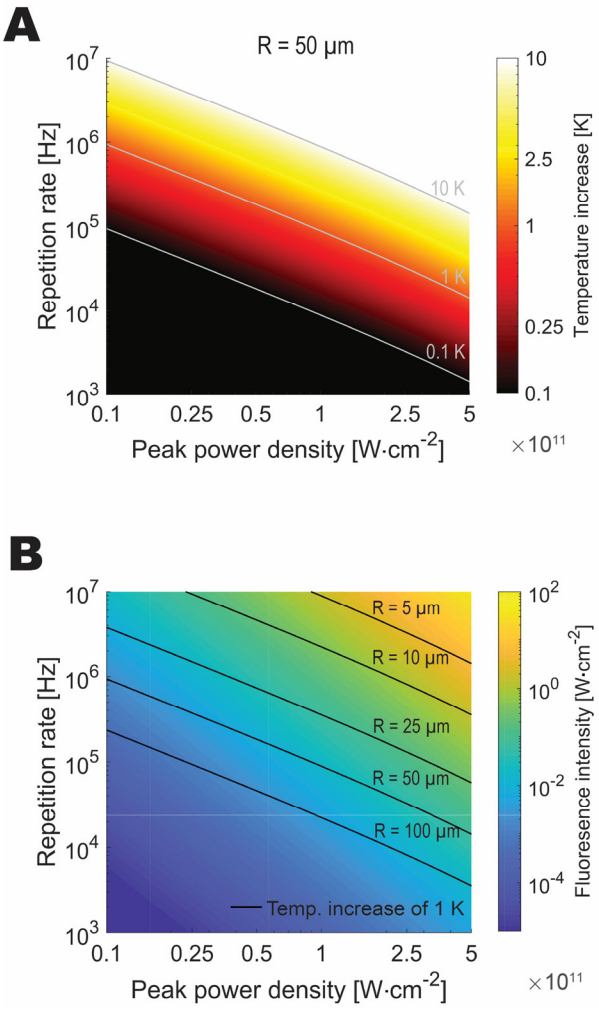

Figure 2.8 Optimal combination of peak power density and repetition rate for the highest signal intensity within thermal constraints. (A) The steady-state temperature increase as function of pulse peak power density and repetition rate for a spot with 50 µm radius. (B) Fluorescence intensity as a function of peak power density and repetition rate with predicted isotherm limits of 1 K for excitation spots of different radii. Adapted from (Lisicovas et al. 2019).

2.3.4 Design of a novel immobilization device for imaging with aversive cues

While multi neuron activity recordings from freely moving *C. elegans* are desirable, the analysis of acquired data is complex and is a research problem in itself.

Aside from challenges of achieving continues tracking of the region of interest at high magnification, accounting for animal body shape deformation, volumetric drift due to limited volumetric acquisition frame rate represent significant challenges (Nguyen et al. 2016). To avoid these challenges altogether, the conventional approach is to immobilize animals during imaging experiments. This can be achieved by a variety of means, the most popular of which is the use of glue and microfluidic device. The use of glue is not suitable for imaging due to optical distortion arising from high refractivity of the adhesive. In the case of immobilization in a microfluidic device, it possible to apply anesthetic agents in animal containment buffer to inhibit movement. However, the effects these compounds may have on the nervous system are not fully understood. The alternative is to use physical immobilization by application of pressure or suction to prevent animal movement (Kim et al. 2013).

Conventional microfluidic devices are manufactured by spin coating of photoresist have a uniform thickness, and subsequent development process results in deviations from exact design. Without layering, such devices can be designed only in two dimensions, and the processes of making a mask for molding is time-consuming. Because of these design constraints and challenges in manufacturing, it is difficult to produce an immobilization device that would contain an animal in place under liquid flow. In this work, immobilization is accomplished using a design modified from (Schrödel et al. 2013) to include specifically crafted 2.5 dimensional features. Two pinches and tapered head holder as well as positive pressure applied on the animal input channel contain the animal in place. Imaging chamber has sufficient opening to allow the animal nose to reach out to chemical stimulus, but sufficiently narrow to prevent animal sliding. This design is particularly important when stimulating with aversive compounds as animals tend to avoid exposure at any cost. Figure 2.9 shows an immobilization device, I have designed, manufactured and used for live imaging in this work.

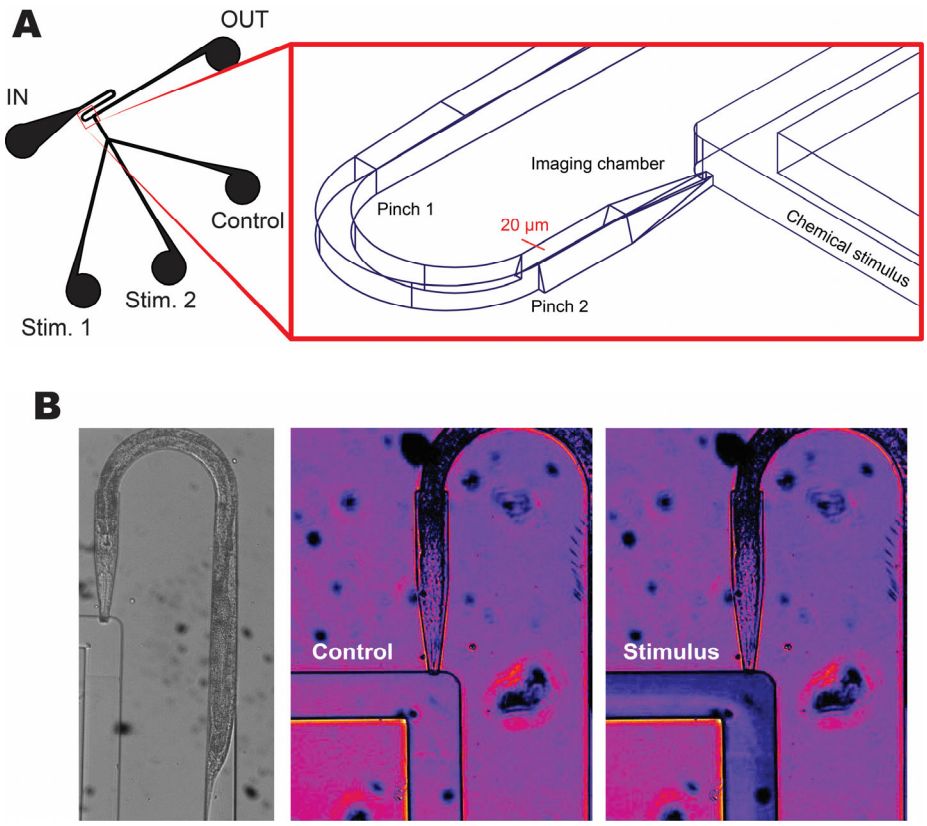

Figure 2.9 2.5D microfluidic device for animal immobilization. (A) The device was designed to accept and orient animals (IN), after which they are transported by flow into the imaging chamber. Two physical pinches prevent the animal from sliding backward. The nose tip with chemical receptors slides into the wedge for presentation of the stimuli (Stim. 1-2 and Control) en route to waste collector (OUT). (B) Shows the orientation of the animal in the device and demonstrates how stimulus is applied by laminar flow. In this case, a solution of food coloring was applied and a false-color map was used to enhance the contrast of a grayscale image.

2.3.5 Application of increased repetition rates for live animal imaging

Application of WF-TeFo for imaging of *C. elegans* has been previously reported (Schrödel et al. 2013). The authors achieved temporal and spatial resolution for recording from multiple cell bodies of neurons. They have employed a 10 kHz repetition laser system in conjunction with a photomultiplier to improve fluorescence signal detection and were

able to record from animals up to 5 min at a time. I have attempted to use a 1 kHz repetition laser system for live animal imaging; however, the obtained signal intensity was too low to extract neural activity without a photomultiplier device.

To test how an increase in repetition rate would affect the obtained fluorescence signal strength and photobleaching, I have used the high repetition laser source tuned to its maximum specification repetition rate of 100 kHz. As a proof of principle, I have chosen to analyze a well-defined response of *C. elegans* to high osmolality solution. When animals encounter high osmolality, they immediately initiate a reversal. This response is mediated by the ASH neuron pair through a TRPV4 cation channel (Liedtke et al. 2003). A genetically engineered animal strain expressing neural activity probe GCaMP5G expressed in a subset of aversive neurons was used for this experiment (see the Materials and Methods section). As described above, characterization of fluorescent beads indicates parallel properties with GFP. Since GCaMP5G is a derivative of GFP (Akerboom et al. 2012), I expected to observe similar improvements in signal intensity and photobleaching characteristics.

The animal was trapped in the custom made microfluidics device and allowed to acclimatize to a new setting for at least 30 min. During continuous volumetric recording, animal was exposed to repeated pulses of glycerol solution (1M). The striking result of the imaging experiment is the high amount of fluorescence generated by the setup. Even baseline fluorescence was sufficiently strong to be captured on the detector without any amplification. Using peak power densities at around $0.25 \cdot 10^{11}$ W·cm^2, I was able to perform continuous recording of basal fluorescence for over 25 minutes with sufficiently high fluorescence signal and virtually no photobleaching. Figure 2.10 shows the results from live imaging experiments.

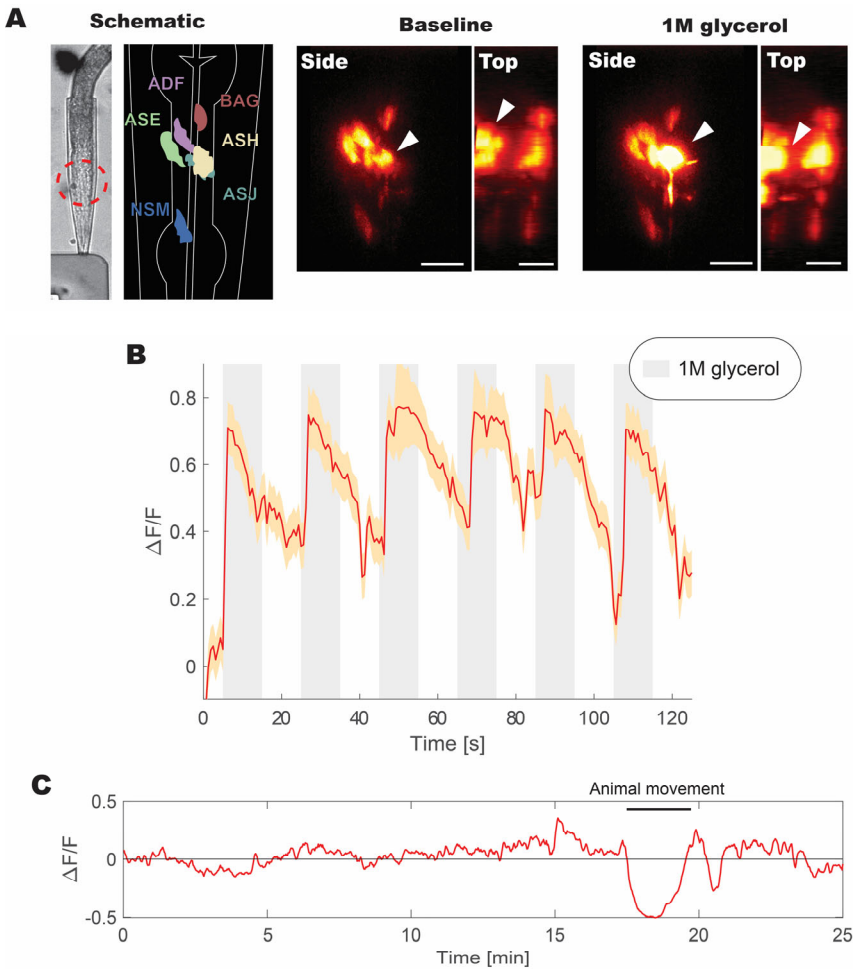

Figure 2.10 Volumetric imaging of live animals at 100 kHz with WF-TeFo. (A) Animals immobilized in a microfluidic device were subjected to continuous volumetric imaging. Out of the aversive neurons expressing neural activity probe, only ASH reacts to initial 1M glycerol stimulus (white arrow). (B) Normalized fluorescence change extracted from the ASH cell body shows periodic activation coinciding with glycerol pulses (20 s period between pulses). (C) Continuous recording of baseline neuronal activity without stimulation. Note that large drop in relative fluorescence at 18 min mark is due to animal movement in the device. Volumetric data were collected at ~2 Hz with 30 ms exposure for each slice. Normalized fluorescence intensity was calculated as a mean of volumetric fluorescence. Error bars represent standard error of the mean derived from measurements of individual pixels in the recording. Scale bars denote 10 µm. Adapted from (Lisicovas et al. 2019).

2.4 Discussion

In this chapter, I have outlined and demonstrated the improvements in WF-TeFo conferred by an increase in the repetition rate of the excitation laser source. Similar gains have been alluded to by others (Therrien et al. 2011; Prevedel et al. 2016). I expand these observations by directly comparing different repetition rates and providing an estimate of the upper limit of repetition rates that are practical for live imaging applications. The increase in repetition rate, while substantially enhancing the obtained fluorescence signal intensity, does not, at least for modest increase tested here, translate to increases in photobleaching. Furthermore, the demonstration of live imaging of neuronal activity in *C. elegans* shows the promise of WF-TeFo with increased repetition rate to be applied to high throughput volumetric imaging of long-term plastic changes in the nervous system of the nematode. The increase of repetition rate potentially offers an increase in continuous volumetric acquisition rate or duration by an order of magnitude, as indicated by modelling.

Technical advantages offered by WF-TeFo are likely to increase the popularity of the system in the future. The implementation of the technique does not require any proprietary components and is relatively insensitive to alignment errors (Oron and Silberberg 2015). In addition to this, the self-correcting property of the grating and objective pair ensures the Fourier transform-limited pulse durations are achieved at the focus and do not require additional compensation (for small amount of higher-order dispersion). This is an essential consideration for optimal performance of scanning microscopy setups primarily due to dispersion introduced by the objective lens (Field et al. 2010). The volumetric imaging rate of current implementation is mostly limited by the sensitivity of the detector. However, the CMOS technology is becoming more sensitive, quickly approaching the photon detection efficiency levels of EMCCDs, while maintaining the advantages of high resolution, high readout speed and reducing the detector noise (Gouveia and Choubey 2016). Considering this and advantages offered by increased repetition rate, the last limiting factor will be the speed of piezo actuator for axial scanning. And here also, WF-TeFo offers the advantage over the other scanning techniques, since the focal plane can be controlled through introduction of second-order dispersion. This feature of the technique allows for dispensing with slow mechanical scanning using piezo actuators to move the sample or the objective and instead introduce second-order group-

delay dispersion to control the focus. A dispersion control system design using a piezo bimorph mirror in a folded 4-f grating pair setup could be used to achieve kilohertz scanning speeds. And recently, fast scanning speed has been demonstrated by using an electrically tunable lens system to introduce dispersion (M. E. Durst, Zhu, and Xu 2008; Michael E. Durst and Turcios 2019).

Beyond imaging of *C. elegans*, a common application, where WF-TeFo is inferior to scanning techniques is the deep tissue imaging. While it is possible to compensate for dispersion and generate temporal focus deep inside the tissue with wave front-shaping (Katz et al. 2011), the resulting fluorescence information will be lost due to greater scattering and absorption at emission wavelength. This issue can be alleviated somewhat by engineering of redshifted neuronal activity probes that take advantage of different near-infrared spectral windows (Sordillo et al. 2014) for excitation and emission, and there are promising results leading in that direction (Qian et al. 2019; Piatkevich et al. 2018).

The most significant challenge for the implementation of WF-TeFo, or any two-photon technique, by biology and neuroscience laboratories is the excitation laser source. Currently, most of the lasers used for this purpose rely on Kerr-lens mode-locking in titanium-doped sapphire (Ti: Sa) crystal (Lefort 2017). These systems, however, cannot provide sufficient peak power density for large area WF-TeFo. The standard solution is to use regenerative amplifier systems coupled with non-linear optical parametric amplifiers. These systems are complex and require specialized expertise to configure and operate and are rather inconvenient for routine applications in imaging. Advances in fiber laser technology promise compact and exceedingly stable laser sources with convenient control over repetition rate but have limited wavelength tenability (Xu and Wise 2013). The last limitation has been resolved with new generation of non-colinear optical parametric amplifiers complementing the high power/ high repetition laser systems (i.e., Spirit and Spirit-NOPA, Spectra-Physics) offering convenient control over repetition rate and wavelength without the need to tinker with internal optics.

In summary, presented improvements in fluorescence signal intensity and photobleaching characteristics with increased repetition rate within thermal limits extend the utility of WF-TeFo. Exciting developments in high power/ high repetition rate fiber laser systems, as well as intrinsic advantages of WF-TeFo, make this technology a promising candidate for future fast/ long-term volumetric live imaging applications.

3 Long-term tracking of population behavior in response to olfactory and multicolor optogenetic stimuli

Contributions: equipment design, implementation, transgenic engineering, data collection, and analysis were performed by me. Dr. Eichiro Saita contributed valuable advice on odor delivery system; Dr. Takashi Maruyama provided some materials CRISPR integration and advice on molecular biology and genetic engineering; Dr. Tosif Ahamed gave valuable advice on data analysis. Prof. Ichiro N. Maruyama provided resources and lab space.

Abstract

Semi-automated and automated behavioral tracking and analysis have become indispensable tools for *C. elegans* neuroscience research. High-throughput studies have thus far revealed an incredible level of complexity arising from a mere 302 neurons. Behavior analysis methods range from simple centroid tracking to identify behavioral events (forward, backward locomotion, steering, etc.) to complex analysis of shape and locomotion patterns using dimensionality reduction. However, the majority of reports has focused on behaviors occurring on relatively short-time scales. Here I demonstrate a low-cost system capable of simultaneous tracking of ~50 animals over the course of hours. It is equipped with the ability to stimulate genetically targeted neurons with channelrhodopsins in red and blue channels, as well as two odorants simultaneously. The custom-written software modules provide real-time compression of data, isolating animal shapes as well as stimulus annotation. I characterize the system and use it to compare integration of contradictory olfactory/optogenetic stimuli induced behavior occurring in the crosstalk between sensory neurons. An in-depth analysis of long-term behavior remains one of the uncharted avenues of *C. elegans* research and for the first time a dual-channel optogenetic stimulation capable population tracker is implemented here to address this. The demonstrated system design presents a cost-effective and robust method for in-depth study of population dynamics occurring in response to diverse olfactory and optical stimuli.

3.1 Introduction

Since the inception of neuroscience, the study of behavior played a vital role in understanding the underlying mechanisms of neuronal action. Indeed, early studies integrating surgical intervention and resulting behavior changes in animals, as well as in humans provided many of the ideas at the core of modern neuroscience (Hebb 1962). Insights gained from study of animal behavioral adaptation motivated the development of the reinforcement learning framework used for automation of decision-making and goal-directed behavior (Richard S. Sutton and Andrew G. Barto 1998). In *C. elegans* research too, analysis of behavior has played a central role from the outset of the adoption of this model organism. Genetic screens, both forward and reverse, has long since used informative (albeit, not rigorously quantitative) descriptions of observed phenotypes (Brenner 1974; J. Hodgkin 1983). These studies have been and continue to be instrumental in gaining a more profound understanding of worm biology and organizing principles of the neuronal systems.

The somewhat crude descriptions, however, fail to capture the rich complexity of behavior. The first automated tracking of *C. elegans* has leveraged the newly available camera and computer technology to capture movement directions of 25 animals simultaneously (Dusenbery 1985). As the richness of the behavior has been slowly uncovered by the research community (Catharine H Rankin 2004), advances in tracking technology are driving the understanding of this complexity. Single worm tracking was instrumental in studies of worm navigation strategies (Pierce-Shimomura, Morse, and Lockery 1999; Yoshida et al. 2012), food preference (Shtonda and Avery 2006) and for phenotyping of the effects of mutations (Brown et al. 2013), however, a higher throughput method of tracking was desirable to gain statistical power for more subtle changes. Population tracking has been implemented for analysis of thermotactic plasticity (Chi et al. 2007; Winter et al. 2016) drug-induced effects (Ramot et al. 2008), habituation (Swierczek et al. 2011) sleep/ wake behavior (Winbush et al. 2015), effects of neuromodulators (Stern, Kirst, and Bargmann 2017; Flavell et al. 2013).

Light-activated ion channels provide an indispensable tool for dissection of neuronal networks (Deisseroth 2015). *C. elegans* was the first model organism to utilize the newly found bacterial ChR2 for direct activation of neurons (G. Nagel et al. 2005). A comprehensive toolset developed by the *C. elegans* community over the years enables

targeting of specific neurons for expression of transgenic proteins. A combination of these technologies has been applied for the study of information integration by enhancing or suppressing neuronal activity. Optogenetics has been used to study a diverse set of systems: dissection of forward/ reverse locomotion, mechanosensation, nociception, chemosensation, thermosensation, and learning (Husson, Gottschalk, and Leifer 2013; Fischer, Vladis, and Busch 2018). Efforts in protein engineering have introduced variants of optogenetic proteins with red-shifted spectral sensitivity (Klapoetke et al. 2014; Erbguth et al. 2012). These have been successfully applied to *C. elegans* mechanosensory stimulation (Schild and Glauser 2015). While optogenetic stimulation has been combined with population tracking recently (Yu et al. 2019), there is no available population tracker with the capability of dual-color excitation.

In this chapter, I present a novel low-cost population tracking platform capable of capturing detailed behavior, including both movement direction and shape, at high frame rates in response to olfactory and optogenetic stimuli with high temporal and spatial resolution and over long time scales. The system uses real-time lossless compression of behavioral data and active background subtraction, which enables practically unlimited recording length on changing or uneven background. I demonstrate that this system can be employed for the study of integration of optogenetic stimuli using engineered animal strains. To my knowledge, this is the first demonstration of the population tracking system with dual-color optogenetic stimulation capability.

3.2 Materials and Methods

3.2.1 Animal cultivation and preparation of transgenic strains

C. elegans were cultivated using standard methods (Brenner 1974) with some modifications. Five adult animals were picked to fresh NGM agar plates seeded with bacteria (*E. coli*, OP50) every four days and allowed to lay eggs for ~4 hours before removal. The new generation was then allowed to grow undisturbed in a dark incubator set to 20°C. Special care was taken to ensure that animals at no time are exposed to starvation conditions or mold/ pathogenic bacteria contamination. All animal strains were restarted from frozen stocks (Wood 1988) every four months to prevent accumulation of mutations in the genome. The newly started strains were allowed a minimum of two weeks (~4 generations) to enable the population to recover from suspended animation.

Plasmids for transgenes were prepared using standard techniques of molecular biology (Ausubel 1998). Gene fragments were amplified from precursor plasmids or the genome by PCR and assembled using either Gateway kit (Invitrogen) or for sequences used in CRISPR using Gibson assembly kit (New England Biolabs). Table 3.1 lists all plasmids used in this work (IPB stands for 'Information Processing Biology Unit'). Precursors were obtained from other laboratories through proxy repository (Addgene); the rest were provided by Information Processing Biology Unit and generated by me. All generated transgenic plasmids were tested using sequencing to ensure absence of mutations.

Table 3.1 Plasmids used for the preparation of transgenic animals

Plasmid	Description	Source
pCAG (ChrimsonR-tdT)	Plasmid containing ChrimsonR channelrhodopsin.	Addgene Nr. 59169; (Klapoetke et al. 2014)
pDD162 (*eft-3p* :: Cas9 - [Empty sgRNA])	Plasmid expressing Cas9 protein and guide RNA for introducing genome cuts.	Addgene Nr. 46168; (Dickinson et al. 2015)
pENTR P12 (*odr-10p*)	Gene promoter for expressing specifically in AWA neurons.	IPB plasmid collection
pENTR P12 (*ttx-3p*)	Gene promoter for expressing specifically in AIY neurons.	IPB plasmid collection
pENTR P12 (*lin-44p* :: RFP)	Selection marker expressing RFP in animal tail.	IPB plasmid collection
pPD4926 (*bli4*L - [Empty] - *bli4*R)	Plasmid backbone for CRISPR mediated homologous recombination near *bla-4* gene region.	Prepared by Dr.Takashi Murayama
pDD162 (*eft-3p* :: Cas9 - [*bli4* sgRNA])	Plasmid for introducing a genome cut near *bla-4* gene region.	Prepared by Dr.Takashi Murayama
pDEST (*ttx-3p* :: ChrimsonR-vGFP :: *unc-86* 3'UTR)	Gateway assembled expression cassette to achieve ChrimsonR localization exclusively in AIY neurons.	Prepared by me for this work.
pDEST (*odr-10p* :: ChrimsonR-venusGFP :: *unc-86* 3'UTR)	Gateway assembled expression cassette to achieve ChrimsonR localization exclusively in AWA neurons.	Prepared by me for this work.
pPD4926 (*bli4*L - [*ttx-3p* :: ChrimsonR-venusGFP :: *unc-86* 3'UTR] - *bli4*R)	Gibson assembled homologous recombination cassette for genomic integration.	Prepared by me for this work.
pPD4926 (*bli4*L - [*odr-10p* :: ChrimsonR-venusGFP :: *unc-86* 3'UTR] - *bli4*R)	Gibson assembled homologous recombination cassette for genomic integration.	Prepared by me for this work.

Plasmids were injected using standard microinjection protocol (Evans 2006) and selected for animal lines with stable expression of fluorescent markers. Final confirmation

was performed using confocal imaging. For this purpose, the imaging slide was prepared by the application of a thin layer (0.5 mm) of 2% agarose in M9 medium. Then 10µL of 0.5M NaN_3 solution was applied to the agar pad, and adult animals were submerged by using a pick. After cessation of movement, a coverslip was applied and sealed using nail polish. Imaging was performed on LSM780 confocal microscope (Zeiss) using 2.5 mW 488 nm laser diode source. Animals were optically sectioned in axial dimension. The resulting stack was projected using Fiji image analysis software (Schindelin et al. 2012) by average intensity (see figure 3.1).

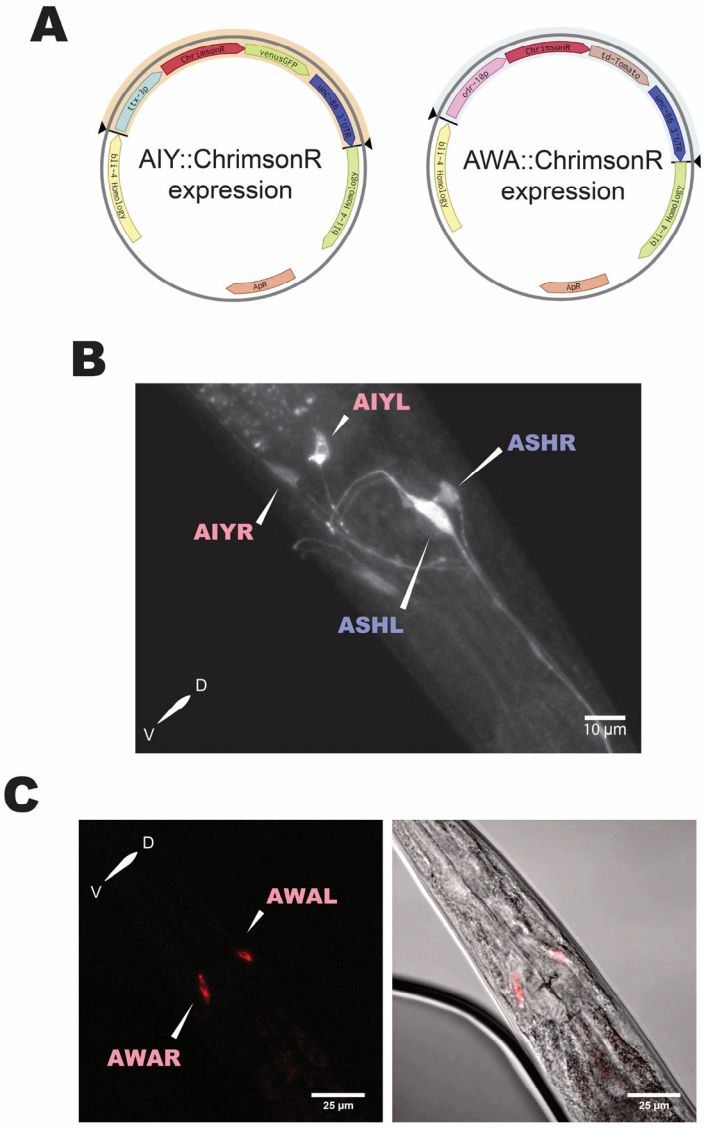

Figure 3.1 Expression of transgenic proteins in engineered animal strains. (A) Plasmids engineered for expression of ChrimsonR (CrR) channelrhodopsin in AIY and AWA neurons. (B) Expression of CrR and ChR2 visualized by fused venusGFP in AIY and ASH neurons, respectively. (C) Expression of CrR in AWA neurons visualized by imaging fused tdTomato fluorescent protein. White bars denote scale bars (10 or 25 µm). Orientation is indicated by versal (V) and dorsal (D) directions.

All animal strains used in this study are summarized in table 3.2. Where indicated, animal strains were received from *Caenorhabditis Elegans* Genetics Center (CGC), which is funded by the NIH Office of Research Infrastructure Programs (P40 OD010440).

Table 3.2 Animal strains used in the study

Strain	Description	Source
N2	Wild type strain.	(Brenner 1974).
lite-1 (ce314)	Lack of *lite-1*receptor reduced sensitivity to blue and ultraviolet light.	Received from CGC (Edwards et al. 2008).
AQ2235 *lite-1* (ce314); ljIs114 [*gpa-13p* :: FLPase, *sra-6p* :: FTF :: ChR2H :: eGFP]	Expression of ChR2 exclusively in ASH neuron pair.	Received from CGC (Ezcurra et al. 2011).
AQ2235 *lite-1* (ce314); ljIs114 [*gpa-13p* :: FLPase, *sra-6p* :: FTF :: ChR2H eGFP]; ex[*odr-10p* :: ChrimsonR :: tdTomato]	Integrated expression of ChR2 in ASH neurons and extrachromosomal ChrimsonR in AWA neurons.	Prepared by me for this work.
AQ2235 *lite-1* (ce314); [*ttx-3p* :: ChrimsonR :: venusGFP]	Integrated expression of ChrimsonR in AIY neurons.	Prepared by me for this work.
AQ2235 *lite-1* (ce314); ljIs114 [*gpa-13p* :: FLPase, *sra-6p* :: FTF :: ChR2H :: eGFP]; [*ttx-3p* :: ChrimsonR :: venusGFP]	Integrated expression of ChR2 in ASH neurons and ChrimsonR in AIY neurons.	Prepared by me for this work.

3.2.2 Population assay conditions

For experiments involving optogenetic stimulation, L4 adolescent animals were transferred to plates seeded with 150 µl of OP50 culture supplemented to 1mM all-trans-retinal (Sigma) (ATR) and left to dry in a clean hood (G. Nagel et al. 2005). Animals were used for experiments after a minimum of 10 h exposure to ATR. Animal behavior analysis was performed on modified chemotaxis buffer (CTX) agar plates (C I Bargmann, Hartwieg, and Horvitz 1993). CTX agar was made the day before the experiment by dissolving premade agar solution: 15 g/L bactoagar (BD, USA), 214 mM D-sorbitol (Sigma); and supplementing it with CTX buffer components (to the final concentration of: cholesterol (5mg/L), $MgSO_4$ (1mM), $CaCl_2$ (1mM) and KPO_4 (25mM)). The resulting solution was measured to have ~300 mOsm osmotic pressure (Osmomat 010, Gonotec).

Warm agar solution was then distributed to 30 mm culture dish plates (Falcon) and left to stand with lids closed overnight. An OP50 liquid culture was incubated at 25°C for 13-14 hours overnight. Then 10 mL was centrifuged at 6000g at 4°C and washed with CTX buffer and suspended in 2mL CTX for storage at 4°C. Before the experiment, plates were seeded with 200 arbitrary units (calculated as a product of volume and concentration estimate through optical density measurement, i.e. 20 µL solution with OD_{600} value of 10 or equivalent amount) of OP50. Bacterial culture supplemented with ATR to 1mM unless otherwise specified) and left to dry with lids open. 40-50 animals were transferred to plates using a platinum pick (0.1 mm, Nilaco Corporation) in groups of 20 by taking care to manipulate gently. Then animals were allowed to settle in the dark for 4-5 hours before the start of experiments. In general, 200 units is sufficient to keep 50 animals satiated for ~12-16 hours. The use of minimal medium like CTX for long-term behavioral assay offers several advantages. Firstly, bacteria arrests replication since CTX buffer offers no readily available carbon source, which improves animal tracking. Secondly, absence of cholesterol in CTX formulation prevents overcrowding by arresting egg development.

3.3 Results

3.3.1 Design and implementation of the tracking system

Tracker hardware was designed to combine population tracking with olfactory and optogenetic stimulation. While a number of trackers have been reported previously to share one or more features from this specification (Yu et al. 2019; Husson et al. 2018; Winter et al. 2016), the present system is distinguished by ability to perform two-color optogenetic stimulation and record behavior over long-time scales (hours to potentially days). Tracker hardware can be subdivided into several modules: the imaging module, the olfactory stimulation module, and the optogenetic stimulation module (see figure 3.2).

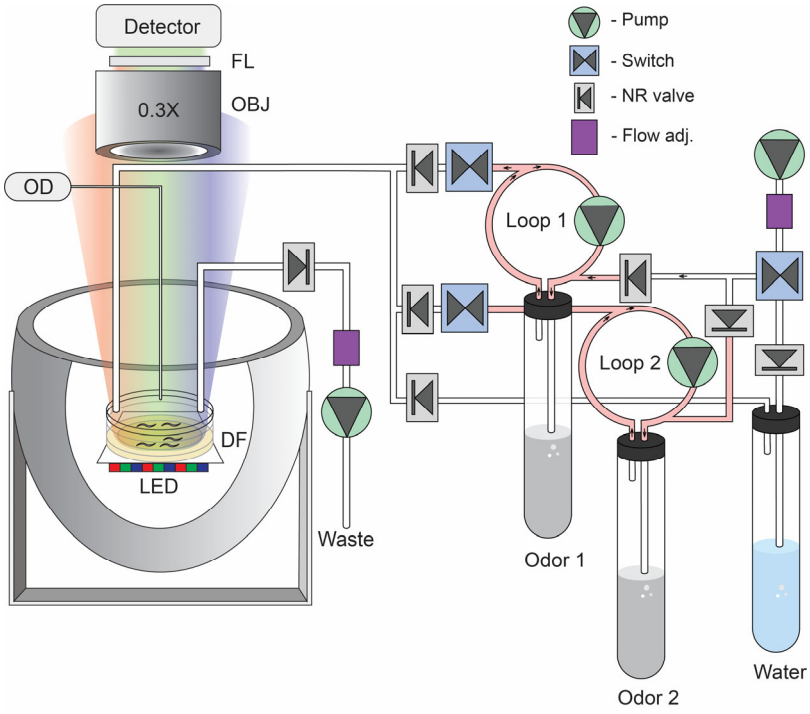

Figure 3.2 Hardware components of the tracking system. The tracking hardware is composed of three subsystems: optical tracking, olfactory stimulation, and optogenetic stimulation. The optical system is composed of a low magnification wide field-of-view objective (OBJ) and a high-resolution, high-speed detector. Filter (FL) was used to separate animal movement data. The optical stimulation system consists of light source with a high-power LED array, which is positioned below the locomotion plate covered by a high-efficiency optical diffuser (DF). The olfactory stimulation system is composed of the system of pumps, switch valves and non-return valves that deliver air stream through odorant solutions or water. Odorant solutions have dedicated recirculation-pumping loops to keep the air saturated at all times. The three air stream channels converge and feed into an acrylic plate covering the behavioral arena. The additional air-circulation system draws the odor infused air out of the chamber, allowing for quick removal of the odorants. Odorant concentration was measured using a volatile organic compound detector (OD).

The imaging module consists of a dissecting microscope (SZ61, Olympus) with a filter turret attachment. A wide-angle low-magnification (0.3X, Olympus) objective was used to replace standard configuration to allow for increased field of view to cover the

whole behavioral arena. A band-pass filter (545/17 nm, Semrock) was used to separate the animal locomotion data from optogenetic stimuli induced background. High-resolution high-speed CMOS camera (Zyla 5.5 10-Tap, Andor Technology) was used to capture behavioral data.

Optogenetic stimulation capability was implemented using a high power light-emitting diode array (LED). A commercial LED array light source (ML-56 COB, Eurolite) was modified to fit animal locomotion plates to maintain consistent illumination intensity throughout the behavioral arena. A high-efficiency micro-patterned optical diffuser plate (80° light shaping diffuser, Optical Solutions) was placed above the array to homogenize intensity. Spectral measurements were performed using a fiber spectrometer (USB4000, Ocean Optics) to determine the wavelength distribution of individual color channels in the array (see figure 3.3). The measured spectra showed excellent overlap with the sensitivity ranges of channelrhodopsins used in this study. Light source power measurements were made using thermopile power meter (PMKIT-21-01, Newport Corporation) to establish the available stimulation range and control granularity. Determined maximum intensity falls well outside the dynamic range of both channelrhodopsins (Klapoetke et al. 2014; G. Nagel et al. 2005). A digital multiplex to USB adapter (Open DMX USB, Enttec) was used to interface light source with the computer. The integrated cooling fans were connected to USB controlled power supply (2230J-30-1, Keithley Instruments) and calibrated to maintain constant temperature of the light source enclosure. The temperature increase was measured using a thermocouple (TX1001, Yokogawa) showed temperature increase in behavioral chamber of less than ~1°/min at or below 1.5mW/mm^2.

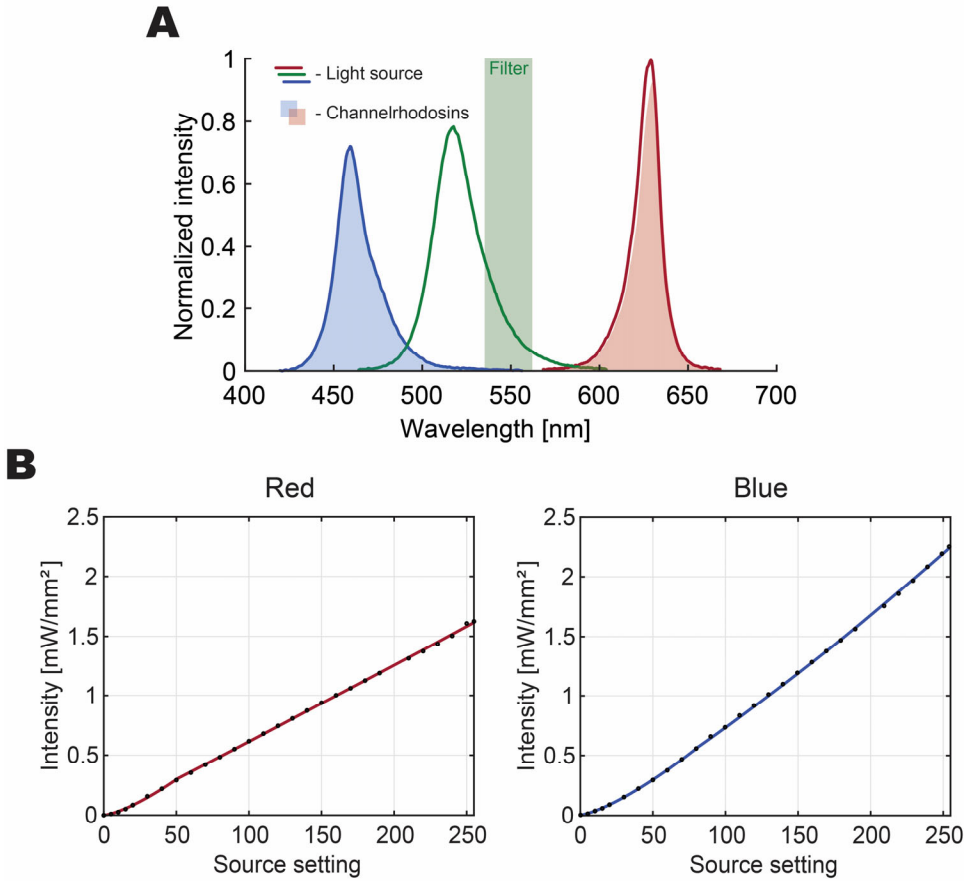

Figure 3.3 Characterization of the light source for optogenetic stimulation. (A) LED spectrum measurement. The solid lines represent the measured spectrum, while shading shows spectral sensitivity of channelrhodopsins: ChR2 and CrR. Spectral sensitivity adapted from (Klapoetke et al. 2014)). The green bar shows the part of the spectrum used for behavioral imaging. (B) Intensity calibration for red and blue components of the LED array, showing the available intensity range.

The olfactory stimulation setup was designed to enable the delivery of discrete odorant pulses with high temporal precision. The system consists of three subsystems. In the 'off' configuration the air is pumped through a water solution to prevent agar desiccation. When odorant delivery is switched on, the air stream is directed through one or both of the concentrator loops. The loops have independent air pumps that continuously recirculate air through a solution keeping it saturated with odorants at all times. Pump control was achieved with USB controlled power supply (2230J-30-1, Keithley

Instruments). A system of non-return valves and electromagnetic valves (Warner Instruments) is employed to prevent odorants from mixing. The material of the tubing connecting the components is particularly important since the typical odorants are readily absorbed by many types of silicone polymers (STI Components, Inc. 2014). For the present system, all tubing was made of polytetrafluoroethylene, which was chosen for chemical stability and low odor trapping.

The output of three sub-systems converges just before the input into locomotion chamber to allow for fast switching of different streams. An acrylic plate is used to hold the input and output piping above the locomotion arena creating a seal with plate holding the animals. Stable air circulation was achieved by a system of two pumps working in tandem on both ends of the path. The odorant concentration was measured using a volatile organic compound detector based on photoionization detection (Tiger handheld VOC detector, Ion Science Ltd.) continuously sampling odorant concentration inside the behavioral chamber.

Figure 3.4 presents the odor pulse characteristics measured for diacetyl (Butane-2,3-dione) and octanol (1-octanol), two odorants commonly used for *C. elegans* behavioral assays, as well as air saturation with diacetyl as a function of concentration in solution. In the case of 1-octanol, I observed no concentration dependence when mixed in either water or mineral oil. It may be due to higher relative vapor density of the 1-octanol (equal to 4.5) and propensity to condense on the interior surfaces of connecting tubing during saturation.

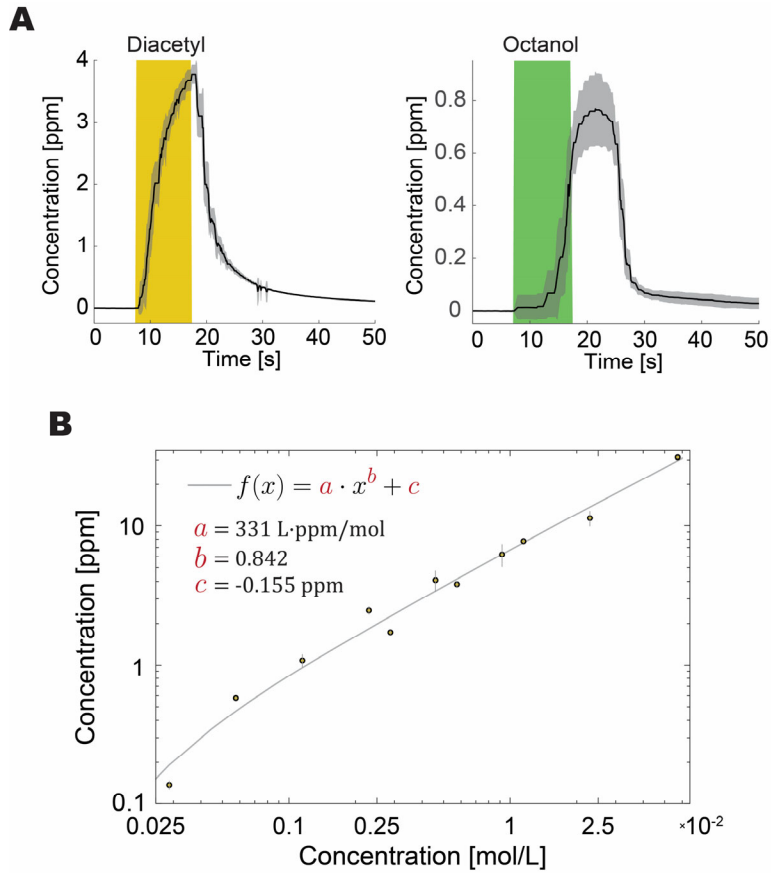

Figure 3.4 Stimulation repeatability and concentration dependence. (A) Odor presentation repeatability measured for diacetyl solution in water and pure 1-octanol. The observed lag between 'on' state and actual concentration peak was taken into account in further analysis. The shading around the mean represents bootstrapped confidence intervals with α=0.05. (B) Measured dependence between diacetyl concentration in the solution and resulting concentration (ppm) in the behavioral chamber for 10 s pulses fitted with a power law. Error bars represent bootstrapped confidence intervals with α=0.05.

3.3.2 Design of tracking software

The goal of the tracking implementation was to enable the collection of detailed behavioral information over long periods of time with high temporal and spatial resolution. Traditionally worm trackers collect video frames for analysis offline post experiments (Husson et al. 2018). Since collecting population data (positions and postures) requires

high-resolution camera sensors, retaining all original data during capture accrues a significant storage burden. For example, the 5.5 megapixels, 16-bit sensor used in this study, running in a continuous data stream at 5 Hz, would accumulate uncompressed data at a rate of 185 GB per hour. For this reason, I have also set out to implement lossless compression of behavioral data during recording.

The architecture of the behavioral tracking software consists of three interdependent modules: equipment control, real-time capture, and post-processing module. Figure 3.5 shows the flowchart diagram of the data flow and function of the three modules.

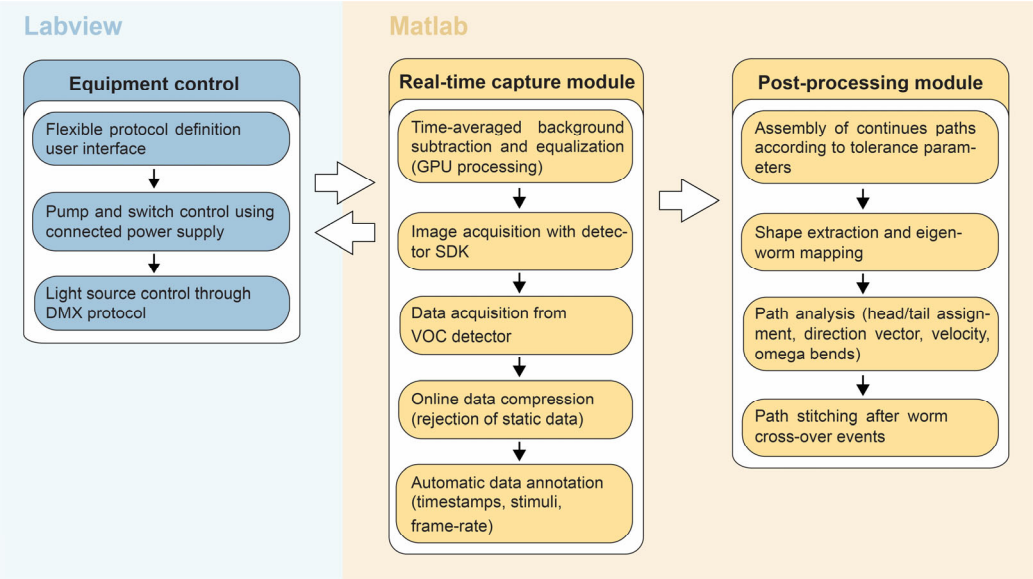

Figure 3.5 Software design flowchart diagram. The data acquisition and experiment control are handled by the interaction of 'Equipment control' and 'Real-time capture' modules. Organized data is then passed onto 'Post-processing' module for extraction of behavioral metrics.

The equipment control module was implemented using Labview (National Instruments, USA). A custom program was written to interface with power supply module to control odor delivery pumps and valves as well as the LED light source through a DMX protocol. The sharing of control and stimulus annotation information with real-time capture module was implemented using a virtual keyboard interface. The module also includes a flexible and easy to use user interface for experiment configuration (see figure 3.6).

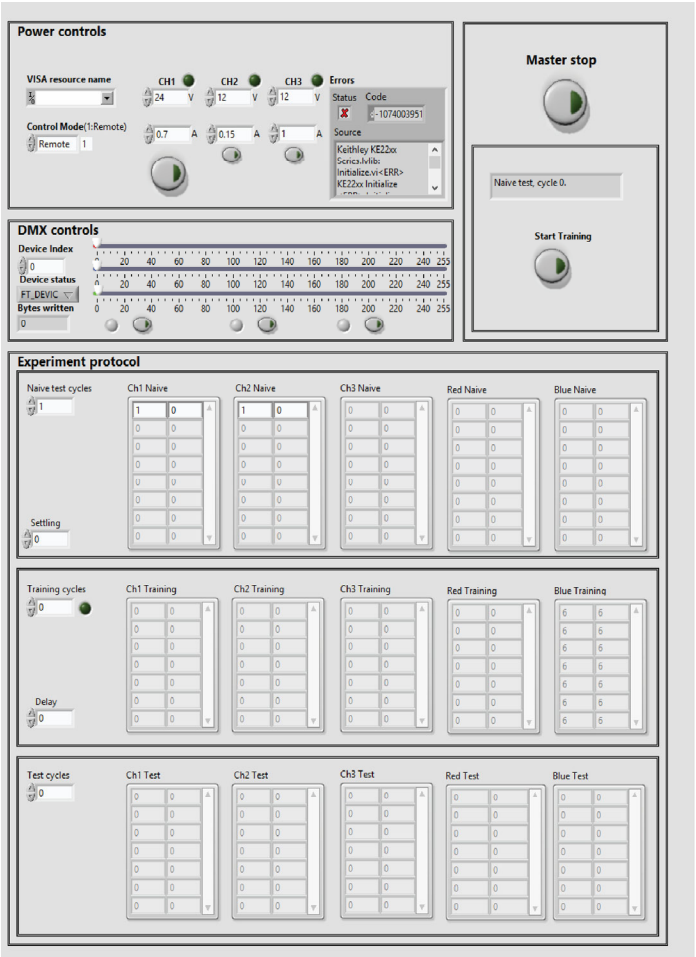

Figure 3.6 Experiment setup user interface. The 'Equipment control' module enables the controlled delivery of odorant and optogenetic stimuli. The user interface allows to easily specify the delay before the start of recording, frequency, temporal pattern and strength of the stimulus application.

The real-time capture module captures the information from the camera sensor and processes it for storage. Each incoming frame is relayed to the graphics processing unit, where background subtraction is performed to isolate pixels representing the animals. The moving average filter was implemented to reject all the static background information, but retain all moving objects of the appropriate size. Once a moving object has been identified, the program tracks its outline, even if the object remains stationary and prevents it from being discarded as the background. The captured data consists of a single averaged

background image, a sparse representation of object pixels, timestamp for each frame and stimulus information from the ‘Equipment control’ module. The software implementation in Matlab (Mathworks) is optimized to have minor impact for performance, and the principal limit for imaging rate is the exposure time of the camera and the latency of the frame acquisition software development kit. In the experiments presented here an average rate of 5 Hz is achieved using 150 ms exposure time. At this rate, the burden of collecting data amounts to roughly 30MB per animal per hour, an approximately 130-fold decrease in collected data without the loss of behavioral information for a typical experiment.

‘Data post-processing’ module further compresses the acquired data by extracting motion data from recordings. These include the absolute position of the animal on the behavioral arena, the tangential velocity (i.e., the speed with regards to the heading direction, (Roberts et al. 2016)), annotation of reversal and turn events and extraction of the shape information (Stephens et al. 2008). A significant difficulty in analyzing population data is the cross-over events between animals, which results in loss of tracking information. Since the tracking hardware can produce images with high dynamic range and spatial resolution, I have applied a technique traditionally used for identification of blood vessels in angiograms (Frangi, Niessen, and Viergever 2001). This approach uses the eigenvalue decomposition of the Hessian matrix of the image to identify outlines of tubular objects with soft edges and performs well for the separation of animals in an aggregate clump. Resolved animal shapes are selected and ordered by the proximity of the centroids into tracks as well as each shape is skeletonized to extract worm posture (Stephens et al. 2008). Each track is processed to determine the position of the animal head. The tip of the head shows more erratic movement in relation to animal body than the tail (Shingai et al. 2013). This observation was used to determine head position for track fragments shorter than 20 sec. For longer tracks, the head position was determined as an extremum of the skeletonized shape that coincides with the movement direction the most, as animals tend to move forward rather than reverse on average (Liu et al. 2018). Based on head position, when the movement of animal head and centroid does not align, the movement is annotated as reversal. If animal assumes a circular shape, the segment is annotated as an omega turn. Figure 3.7 outlines the main steps in analysis process pipeline.

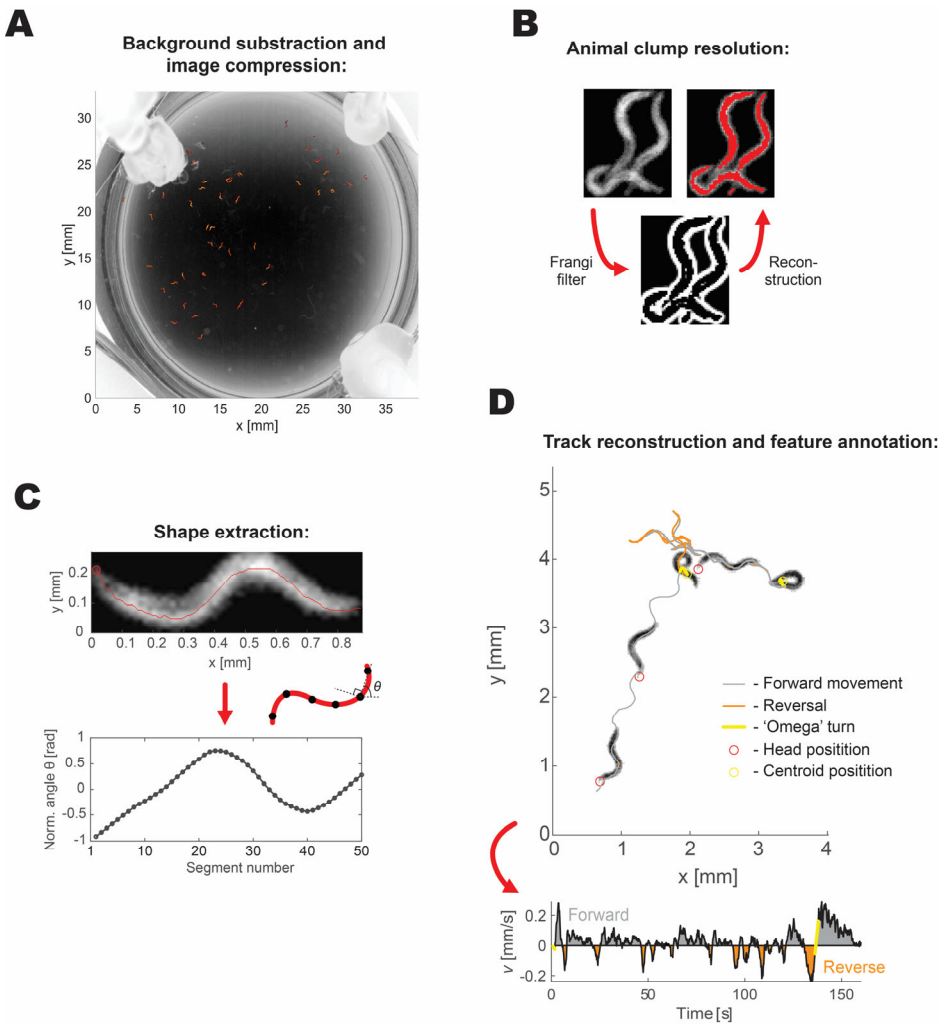

Figure 3.7 Behavioral metric extraction from acquired frames. (A) The whole field of view of a behavioral locomotion arena, showing odor inlet and outlet as well as the odor concentration sampling channel. (B) Clump separation using Frangi filter to find soft boundaries. (C) Animal shapes were skeletonized, divided into segments (50), and fit with a spline. The normalized angle between segments was determined as a representation of the shape. (D) An example track annotated to reveal major features of animal behavior: forward movement, reversal, and omega turn.

3.3.3 Long-term tracking reveals eigenshapes on bacterial food

A high compression ratio allows the population tracker to be used for the collection of behavioral data at high frequency and long-time scales. I sought to test how collected

data compares to that acquired by tracking individual animals. For this purpose, I have analyzed the dimensionality of animal posture variance.

Principle component analysis (PCA) has been previously applied to the analysis of variance of postures (Stephens et al. 2008). It has revealed that 95% of the variance is distributed along four principal components, which the authors term ‘eigenshapes.’ These principle shapes can then be combined to produce more complicated shapes. The work also presents a partial reconstruction of equations of motion for the dynamics in this space, derived from analysis of quarter of a million high-resolution frames with single animals engaged in exploratory behavior off food acquired at 32 Hz. More recently, similar experiment has been performed to obtain the eigenshapes for animals on bacterial food (Brown et al. 2013). While overall eigenshapes are roughly identical, the order is switched, which reflects that animals on food are more likely to be engaged in grazing behavior.

To validate the consistency and accuracy of postural extraction in the present system, I have performed a seven hour-long tracking experiment with no external stimuli and have calculated the eigenshapes. The recovered shapes are in good agreement with published results (Brown et al. 2013). Correlation of second and third principal components reveals a fixed amplitude oscillator evolving clockwise or counterclockwise. This rotation corresponds to animal movement direction. The angular velocity was calculated from the data and cross-correlated with tangential velocity, showing strong correlation ($R=0.75$). This result is in agreement with published data for exploratory locomotion (Stephens et al. 2008) and demonstrates the utility of combined high-resolution and long time scale behavioral population analysis (see figure 3.8).

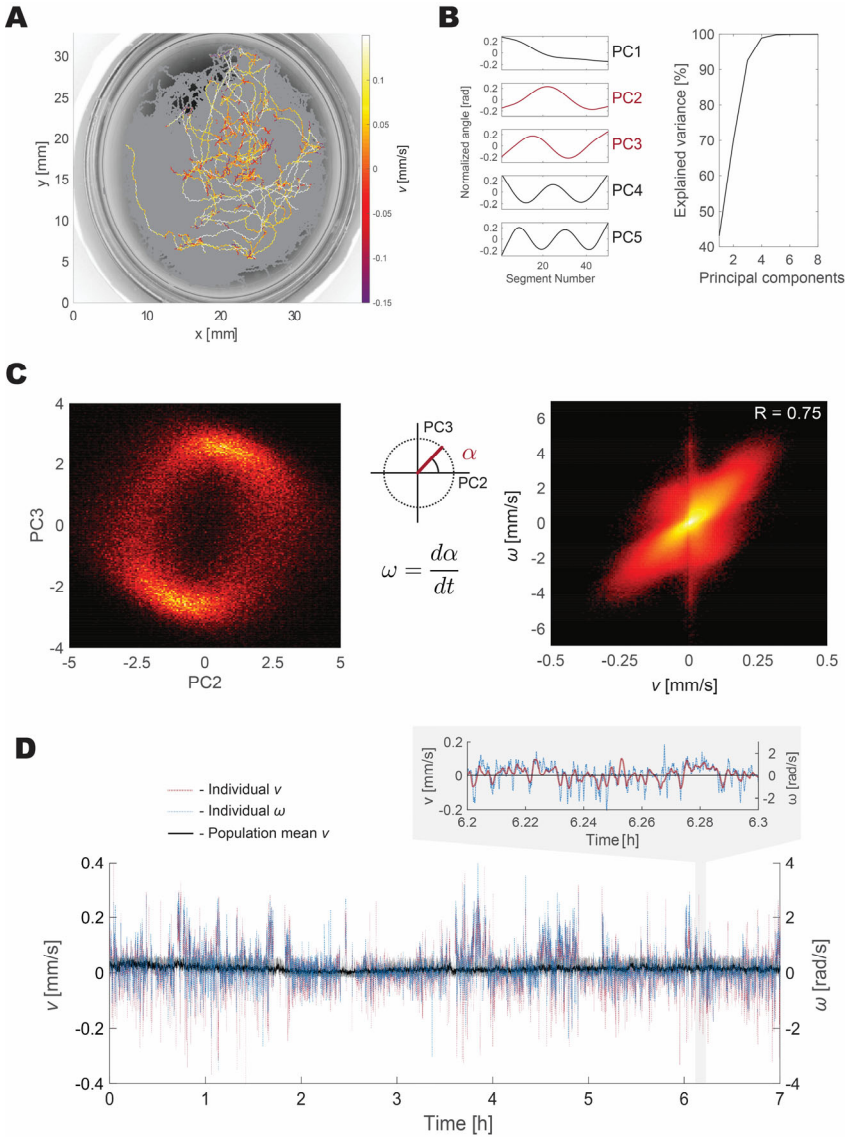

Figure 3.8 Long-term recording analysis reveals principal worm eigenshapes. (A) An example of an animal track over a course of 7 hours highlighted in a population experiment. (B) The result of the principal component analysis of the shape variance reveals five components that, in combination, account for 98.8% of the variance. (C) The correlation plot of the second and third components reveals a cyclical oscillation with animal locomotion. Angular velocity of the oscillator was compared with tangential velocity and found to be in good correlation (R = 0.75). (D) A comparison of tangential velocity and angular velocity metrics for a single animal confirms the correlation. (n=40) animals were used for the experiment.

3.3.4 Pulsed odor stimulus of opposite valence induce locomotion features consistent with attraction and repulsion

To demonstrate the utility of a fully integrated stimulation and population tracking system, I have selected to evaluate the behavioral effects of two olfactory stimuli with opposite valence. A study exploring integration of attractive taste diacetyl and aversive quinine showed that they interact to suppress or promote pumping rate of the pharynx in a concentration dependent manner and hence control feeding (Li et al. 2012). Here I expand on these observations by analyzing the effects of contradictory cues on animal locomotion, when induced with use of olfactory and optical stimuli.

Diacetyl is moderately attractive to *C. elegans* at low concentrations, as determined by behavioral choice assays. Genetic analysis and calcium imaging show that AWA neurons are primarily responsible for sensing diacetyl at low concentrations. In the case of high concentration, diacetyl induces aversion through as yet not fully mapped set of other sensory neurons (Taniguchi et al. 2014). Population tracking in a microfluidics device confirmed that diacetyl solution is attractive at low concentrations, and animals display suppressed turning (Larsch et al. 2015). I have performed population tracking experiments to quantify changes in population tangential velocity in response to diacetyl pulses of varying concentration delivered as a scent, including at high concentrations. Results indicate that animals tend to move towards moderate concentration (6.2 ppm) odor source and away from high concentration (29.7 ppm). Low and moderate diacetyl concentrations make animals speed up and reduce reversals, while high concentrations result in slowing down. Despite short exposure time (10 s), population tracker is capable of capturing this behavioral effect (see figure 3.9).

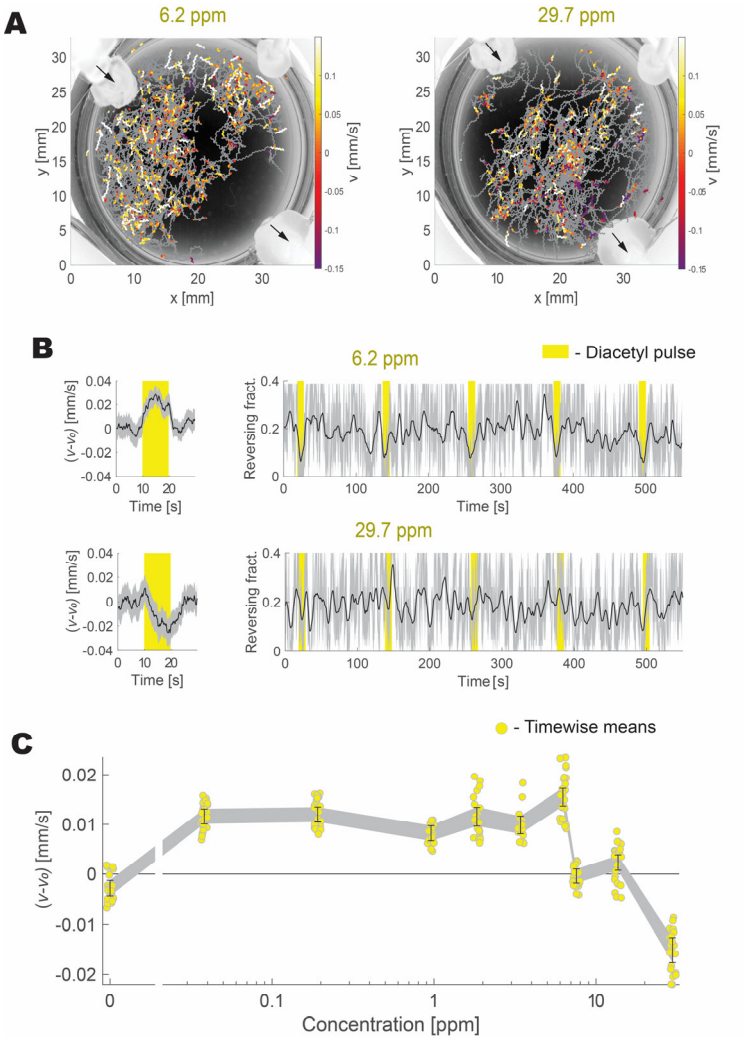

Figure 3.9 The influence of diacetyl concentration on animal behavior. (A) Animals are attracted by the low and moderate diacetyl concentrations and exhibit increased pausing and reversing at high concentrations. The panel shows tracks color-coded with tangential velocity during stimulus application for animals exposed to moderate and high diacetyl concentrations. Arrows indicate the direction of airflow. (B) The average velocity with subtracted baseline locomotion rate and the fraction of reversing animals is shown for moderate and high concentrations of diacetyl pulses. (C) The average velocity with subtracted baseline locomotion rate shown for a range of different concentrations of diacetyl. Circles denote means calculated at different times during pulsed exposure. n=40-50 animals were used for each concentration measurement. Shaded error bars represent bootstrapped confidence intervals with α=0.01.

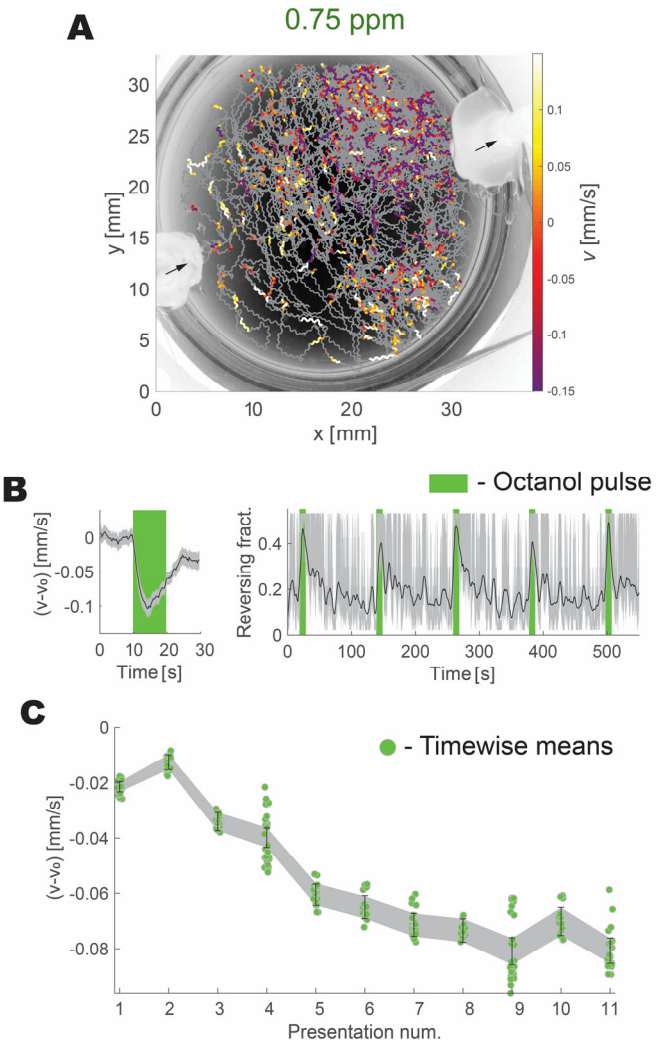

Figure 3.10 Sensitization to repeated octanol pulses. (A) Octanol pulses induce reversals and avoidance. Animal movement during repeated octanol pulses with highlighted sections of the track showing tangential velocity during the odor presentation (color-coded). Arrows indicate the direction of airflow. (B) Octanol pulses induce decrease in average tangential velocity and increased reversals. The baseline velocity before the pulse was subtracted from the velocity during the pulse. (C) Repeated presentation of octanol pulses lead to increase in reversals, demonstrating a sensitization effect of octanol. Circles denote means calculated at different times during pulsed exposure. n=~200 animals were used. Shaded error bars represent bootstrapped confidence intervals with α=0.01.

Octanol pulses induce an aversive response in *C. elegans* on food. At low concentrations, ASH neurons are required and sufficient for sensing octanol (Chao et al. 2004). Indeed, octanol induces a strong activation of the ASH neuron (Summers et al. 2015). I have performed repeated exposure of the animal population to octanol pulses on food to induce aversive responses. Under these conditions animals aggregate away from the odor inlet and a characteristic decrease in tangential velocity over the baseline value and increase in reversing are observed. Repeated pulsed octanol presentation led to progressively increasing aversive responses to the pulses, a phenomenon termed octanol sensitization (see figure 3.10). Octanol sensitization has not been previously reported in experiments on food likely since it is generally assumed that food inhibits octanol avoidance (Metaxakis, Petratou, and Tavernarakis 2018).

3.3.5 Optical stimuli recapture changes in tangential velocity

Published reports have indicated that optogenetic stimuli, applied to sensory and interneurons can be used to approximate natural stimuli. For instance, activation of ASH neurons leads to rapid avoidance behavior, similar to the one induced by chemical stimulation (Faumont et al. 2011). AWA uses a complex concentration encoding, which sends signals only when detecting changes in the odor gradient; nevertheless, optogenetic stimulation has been reported to induce a characteristic reduction in turning (Larsch et al. 2013). AIY interneuron acts as a hub for integration of sensory stimuli with positive valence (Guillermin, Carrillo, and Hallem 2017) involved in regulation of both speed and locomotion direction (Li et al. 2014). It has been demonstrated that animals expressing ChR2 in AIY neurons can navigate in complex artificial light gradients (Kocabas et al. 2012).

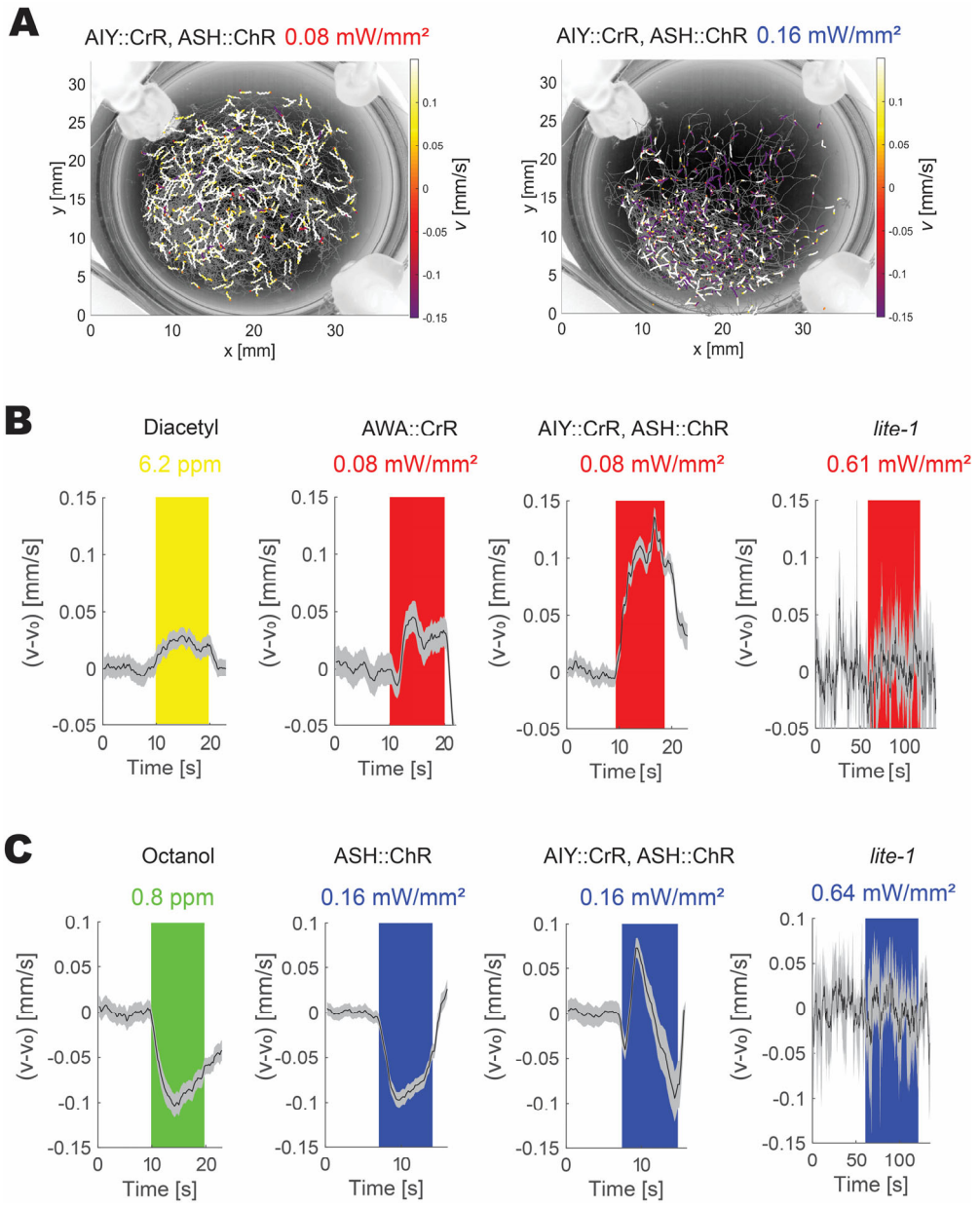

Figure 3.11 Comparison of odor and optogenetic stimuli. (A) Animals, expressing CrR in AIY and ChR2 in ASH, responding to either red or blue light stimuli. Track fragments occurring during stimulation are annotated with velocity. (B) Comparison of average baseline subtracted velocity for appetitive stimuli, optical, and optogenetic. (C) Comparison of average baseline subtracted velocity for aversive stimuli, optical, and optogenetic. Note that *lite-1* serves to demonstrate that observed effects are not caused by temperature increase. n=50-200 animals were used. Shaded error bars represent bootstrapped confidence intervals with α=0.01.

To show that the designed tracking system can be used to induce and capture optogenetic responses, I have performed activation of specific neurons using channelrhodopsins. Behavior was assayed by checking in changes in tangential velocity from the baseline locomotion value. I have confirmed that activation of AWA neuron with CrR increased velocity similarly to diacetyl, while stimulation of AIY interneuron produced a 2-fold greater increase (figure 3.11 A). Optogenetic activation of ASH neuron with ChR2 (in the animal strain expressing only this transgene) recaptured the decrease in velocity seen with octanol pulses (figure 3.11 B). The animal strain expressing CrR in AIY and ChR2 in ASH neurons showed an initial increase and subsequent decrease in velocity compared to the baseline when stimulated with blue light, suggesting a competition of appetitive and aversive drives (figure 3.11 B). This indicates the presence of overlap in excitation spectra between CrR and ChR2.

I then sought to determine how well stimulus strength can be controlled with a change in stimulation power. When activating AIY expressing CrR with increasing intensity, the gain in tangential velocity rapidly saturates (see figure 3.12 A). Analogous experiment using blue light confirms cross-excitability between CrR and ChR2, but CrR is less sensitive to blue light, exhibiting saturation at higher intensity when compared to blue light (see figure 3.12 B). Stimulation of ASH expressing ChR2 leads to a reduction in mean velocity, which also saturates, albeit more gradually (see figure 3.12 B). Simultaneous stimulation of ASH expressing ChR2 and AIY expressing CrR by blue light of increasing intensity displays a complex pattern of competition between appetitive and aversive drives. At lower intensities, the stimulation of ASH overrules AIY on average. At mid intensities, they reach parity, yielding pausing behavior. On the other hand, high blue light intensity leads to abrupt reversals (see figure 3.12 D).

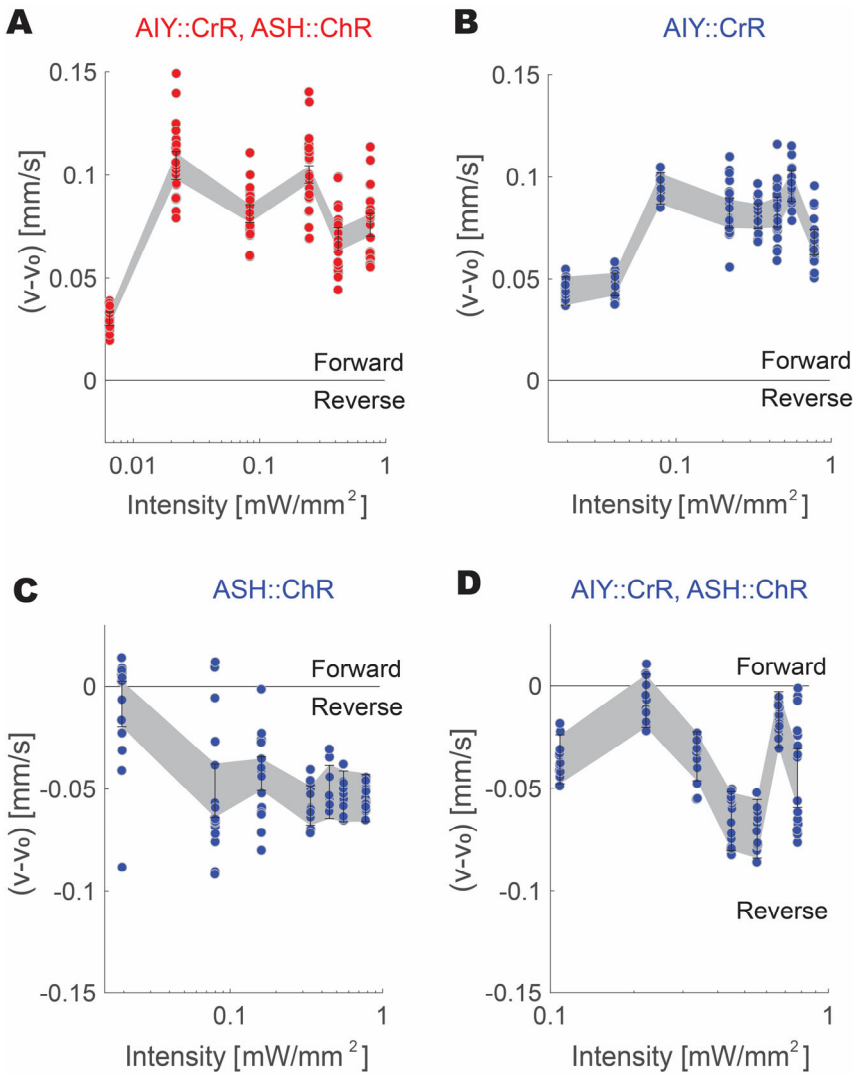

Figure 3.12 Velocity change as a function of optical stimulation power. (A) Responses of animals expressing CrR in AIY and ChR2 in ASH to red light of varying intensity. (B) Responses of animal expressing CrR in AIY to blue light of varying intensity. CrR is sensitive to both red and blue light. (C) Responses of animal expressing ChR2 in ASH to blue light of varying intensity. (D) Responses of animal expressing CrR in AIY and ChR2 in ASH to blue light of varying intensity. This results in stimulation of both AIY and ASH, leading to competition between appetitive and aversive signals. Circles denote means calculated at different times during pulsed exposure. n=~40-50 animals per condition were used. Shaded error bars represent bootstrapped confidence intervals with α=0.01.

3.3.6 Repeated co-stimulation of appetitive and aversive neurons leads to reversal inhibition

Finally, I employ the main advantages of the system: continuous long-term high-resolution behavior tracking and dual-channel olfactory and optical stimulation, to demonstrate its utility for study of long-term plastic behavior. Having demonstrated that sensory stimuli with different valence compete to determine behavioral outcome (increase or decrease of locomotion velocity), I sought to investigate, whether the balance can be shifted with repeated stimulation.

To this end, I have presented the animals with paired stimuli of opposite valence periodically over the course of ~30 minutes without altering stimulation strength. Stimulus strength was selected to favor aversive behavioral outcome. The result was a gradual suppression in average aversive behavior in case of both olfactory and optical stimuli (see figure 3.13 A). Averaging over multiple trials reveals a gradual saturation of the change in velocity (compared to the first presentation) with repeated stimulation when pairing cues of opposite valence. This was in stark contrast to repeats of aversive stimulation only, which in case of octanol produced sensitization and optogenetic activation of ASH alone showed no change (see figure 3.13 B). This result is reminiscent of observed increase in pharyngeal pumping by combination of lower concentration of aversive quinine and high concentration of appetitive diacetyl (Li et al. 2012).

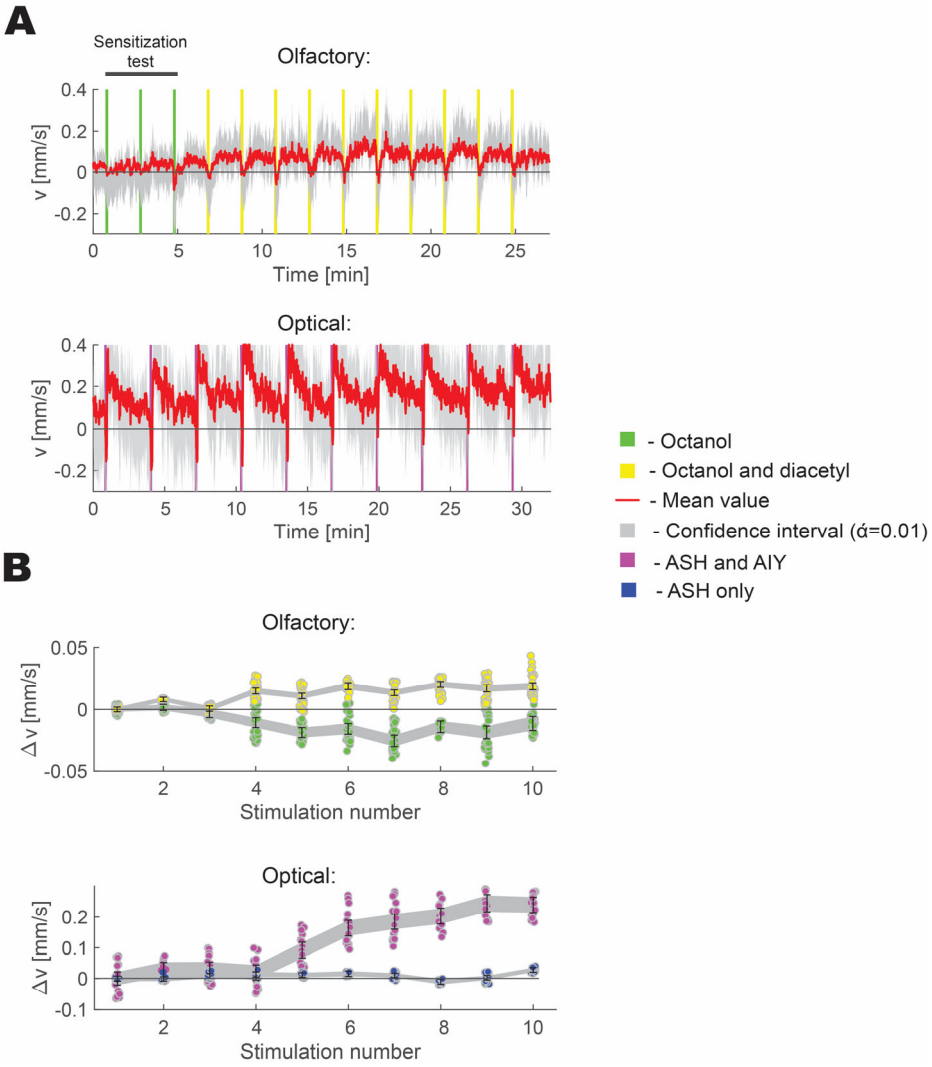

Figure 3.13 Integration of repeated pairing of olfactory and optogenetic stimuli of opposite valence. (A) Time course of a typical tracking experiment with repeated presentation of paired stimuli of opposite valence (olfactory and optogenetic). (B) Change of tangential velocity with repeated stimulation (only aversive only or both aversive and appetitive) reveals a saturation effect. Circles denote means calculated at different times during pulsed exposure. Averaged from n=100-400 animals. In these experiments diacetyl was presented at 6.2 ppm, octanol at 0.75 ppm, red light at 0.08 mW/mm^2 and blue light at 0.16 mW/mm^2. Averaged from n=100-400 animals. Shaded error bars represent bootstrapped confidence intervals with α=0.01.

3.4 Discussion

In this chapter, I demonstrate a low-cost automated population tracking system capable of continuous behavioral monitoring of movement direction and postural information with high temporal and spatial resolution. While it is comparable to the recently published population tracking system for optogenetic analysis based on Multi-Worm Tracker (Yu et al. 2019; Swierczek et al. 2011), the key differences are: the lossless compression of behavioral data (compression ratio of 130), background subtraction algorithm that is resistant to variations in uneven background illumination and changing features on the behavioral arena (i.e. bacterial food lawn), as well as ability to expose animals to odorant pulses and multicolor optogenetic stimuli. As such, this system is a powerful tool for studying the interplay of sensory signal integration and behavior. Olfaction is probably the most evolved sensory modality in *C. elegans*, capable of differentiating between a vast array of chemical compositions with high dynamic range (Cornelia I Bargmann 2006; Larsch et al. 2015). The ability to use a flexible system for odor pulse delivery opens the possibility to study complex decision making processes and plasticity over long time scales.

As a proof of principle for the utility of the present system, I have provided example applications to dimensionality reduction and evaluation of the previously reported flip-flop integration circuit for contradictory sensory cues (Li et al. 2012). For the latter example, I have established that optogenetic stimulation can be used to mimic olfactory cues, as suggested previously (Faumont et al. 2011; Larsch et al. 2015; Kocabas et al. 2012). Experiments performed with increasing intensity reveal a competition between attractive and aversive cues. In both cases, olfactory and optogenetic, the repeated presentation of appetitive cue suppresses aversive responses, especially when attractive cue was delivered through optogenetic activation of the AIY interneuron. Optogenetic stimulation of the AIY interneuron induced the higher reduction, consistent with its proposed function in attractive valence encoding (Guillermin, Carrillo, and Hallem 2017). This inhibition is also reminiscent of the decision-making task involving crossing of aversive fructose barrier to reach a food source, the value of which is gradually increased by hunger state (Ghosh et al. 2016). While presented data is not sufficiently exhaustive to draw a definitive conclusion, it reveals parallels between pharyngeal responses and changes in behavior, when animals are confronted with contradictory cues and, more

importantly, serves to illustrate the typical use case of the tracker design developed in this chapter.

Currently, the main limitation of the system is the inherent cross-excitability of the two types of channelrhodopsins. Under the conditions used in this study, CrR can be independently activated by red light, since it does not open ChR2; however, blue light stimulus activates both CrR and ChR2. Successful independent optical excitation has been previously reported (Klapoetke et al. 2014; Schild and Glauser 2015), using Chronos, a novel blue light sensitive channelrhodopsin variant with faster kinetics. However, this solution is only useful at low light levels and short exposure times, where the inevitable cross-activation red light-sensitive channelrhodopsin by blue light results only in sub-threshold depolarization of the neuron.

The underlying reason for cross-excitability of channelrhodopsins is the use of the same cofactor to confer sensitivity to light (ATR) (Fenno, Yizhar, and Deisseroth 2011), and while the binding site can alter absorption spectrum, the conformational change is not sufficient to altogether abolish the sensitivity to more energetic photons in blue light. Unlike other model organisms routinely used with optogenetics, *C. elegans* do not produce ATR endogenously, and it has to be supplemented for optogenetic stimulation to induce neuronal activation or depolarization. The magnitude of depolarization can be controlled by adjusting the ATR concentration in the environment (G. Nagel et al. 2005). In the future, the cross-excitation could be resolved by engineering optogenetic channel pair, each member of which is loaded with a distinct cofactor that set more stringent constraints on absorption spectrum (Azimihashemi et al. 2014).

Despite current technological limitations, dual-color optogenetics applied to population tracking nevertheless has the potential to prove a powerful tool for optogenetic interrogation of neuronal networks.

4 Conclusion

In the preceding chapters I have presented improvements to optogenetics based methods enabling the dissection of the intricate processes in the neuronal network of *C. elegans* over long time scales. Although developed for the nematode, these techniques can be adapted for other small transparent animal models.

In chapter 2, I have demonstrated a whole-brain capable WF-TeFo imaging system with a high repetition excitation laser source. I show that balancing the excitation intensity and repetition rate can drastically enhance the fluorescence signal collected at the detector and at the same time reduce the fluorophore photobleaching rate. These findings hint at the possibility of enhancing the volumetric imaging rate and duration by order of magnitude and are especially encouraging in light of the ease of implementation of the WF-TeFo, relative stability to pulse broadening, and inherent non-mechanical sectioning capabilities.

In chapter 3, I have demonstrated an implementation of a low-cost automated behavior and posture tracker design with integrated dual olfactory and optogenetic stimulation over the whole behavioral arena. Currently it is the first demonstration of a dual-color optogenetic population tracker. Owing to intelligent background subtraction and on-the-fly data compression, there is practically no limit on the length of experiments that can be undertaken on the system. I have demonstrated that this system can be used to study behavioral implications of signal integration in neuronal circuits.

With the current landscape of optical technology, the improvements in imaging and tracking tools can be benchmarked on where they fall between orthogonal bases of improvement in throughput, and complexity of captured content (Brown and Schafer 2015). The premise of current work proposes an additional basis, which is continuous observation time and demonstrates improvements along these axes.

This set of techniques is intended to complement each other. The main advantage of direct optical stimulation is the ability to induce strong behavioral effects (as demonstrated in Chapter 3) as compared to natural stimuli. Thus neuronal integration can first be probed in a population tracking with high sensitivity until an effect can be observed. These conditions can be then scrutinized in a volumetric imaging system at the scale of individual animals to gain an understanding of the neuronal signaling changes taking place. Alternatively, functional connectivity can suggest points-of-interest to be

probed with optogenetic control to correlate with behavioral outcome, taking advantage of high statistical power. Implementation of such framework with multineuronal recording and stimulation capability has a potential to advance the understanding of relationship between behavior and functional neuronal connectivity, especially considering they can be employed on extended time scales.

Bibliography

Abrahamsson, Sara, Rob Ilic, Jan Wisniewski, Brian Mehl, Liya Yu, Lei Chen, Marcelo Davanco, et al. 2016. “Multifocus Microscopy with Precise Color Multi-Phase Diffractive Optics Applied in Functional Neuronal Imaging.” *Biomed. Opt. Express* 7 (3): 855–69.

Akerboom, Jasper, Tsai Wen Chen, Trevor J. Wardill, Lin Tian, Jonathan S. Marvin, Sevinç Mutlu, Nicole Carreras Calderón, et al. 2012. “Optimization of a GCaMP Calcium Indicator for Neural Activity Imaging.” *Journal of Neuroscience* 32: 13819–13840.

Alcedo, Joy, and Yun Zhang. 2013. “Chapter 10 - Molecular and Cellular Circuits Underlying Caenorhabditis Elegans Olfactory Plasticity.” In *Handbook of Behavioral Neuroscience*, edited by Randolf Menzel and Paul R Benjamin, 22:112–23. Elsevier.

Amano, Hisayuki, and Ichiro N. Maruyama. 2011. “Aversive Olfactory Learning and Associative Long-Term Memory in Caenorhabditis Elegans.” *Learning & Memory (Cold Spring Harbor, N.Y.)* 18: 654–665. https://doi.org/10.1101/lm.2224411.

Amor, Rumelo, Alison McDonald, Johanna Trägårdh, Gillian Robb, Louise Wilson, Nor Zaihana Abdul Rahman, John Dempster, William Bradshaw Amos, Trevor J. Bushell, and Gail McConnell. 2016. “Widefield Two-Photon Excitation without Scanning: Live Cell Microscopy with High Time Resolution and Low Photo-Bleaching.” *PLoS ONE* 11: e0147115.

Ardiel, Evan L., and Catharine H. Rankin. 2010. “An Elegant Mind: Learning and Memory in *Caenorhabditis Elegans*.” *Learning and Memory* 17: 191–201.

Ardiel, Evan L, Andrew C Giles, Alex J Yu, Theodore H Lindsay, Shawn R Lockery, and Catharine H Rankin. 2016. “Dopamine Receptor {DOP-4} Modulates Habituation to Repetitive Photoactivation of a *C. Elegans* Polymodal Nociceptor.” *Learn. Mem.* 23 (10): 495–503.

Ardiel, Evan L, Abhishek Kumar, Joseph Marbach, Ryan Christensen, Rishi Gupta, William Duncan, Jonathan S Daniels, Nico Stuurman, Daniel Colón-Ramos, and Hari Shroff. 2017. “Visualizing Calcium Flux in Freely Moving Nematode Embryos.” *Biophys. J.* 112 (9): 1975–83.

Ausubel, Frederick M. 1998. *Current Protocols in Molecular Biology*. Edited by Frederick M. Ausubel, Roger Brent, Robert E. Kingston, David D. Moore, J.G. Seidman, John A. Smith, Kevin Struhl. John Wiley & Sons.

Azimihashemi, N., K. Erbguth, A. Vogt, T. Riemensperger, E. Rauch, D. Woodmansee, J. Nagpal,

et al. 2014. “Synthetic Retinal Analogues Modify the Spectral and Kinetic Characteristics of Microbial Rhodopsin Optogenetic Tools.” *Nature Communications*, no. 5: 5810.

Bargmann, C I, E Hartwieg, and H R Horvitz. 1993. “Odorant-Selective Genes and Neurons Mediate Olfaction in *C. Elegans*.” *Cell* 74 (3): 515–27.

Bargmann, Cornelia I. 2012. “Beyond the Connectome: How Neuromodulators Shape Neural Circuits.” *Bioessays* 34 (6): 458–65.

Bargmann, Cornelia I. 2006. “Chemosensation in C. Elegans.” *WormBook*, October, 1–29.

Bhattacharya, Raja, Denis Touroutine, Belinda Barbagallo, Jason Climer, Christopher M Lambert, Christopher M Clark, Mark J Alkema, and Michael M Francis. 2014. “A Conserved {Dopamine-Cholecystokinin} Signaling Pathway Shapes {Context--Dependent} *Caenorhabditis Elegans* Behavior.” *PLoS Genet.* 10 (8): e1004584.

Bickle, John. 2016. “Revolutions in Neuroscience: Tool Development.” *Frontiers in Systems Neuroscience* 10: 24.

Birge, Robert R. 1986. “Two-Photon Spectroscopy of Protein-Bound Chromophores.” *Acc. Chem. Res.* 19 (5): 138–46.

Bono, Mario de, and Cornelia I. Bargmann. 1998. “Natural Variation in a Neuropeptide {Y} Receptor Homolog Modifies Social Behavior and Food Response in *C. Elegans*.” *Cell* 94 (5): 679–89.

Bono, Mario de, and Andres Villu Maricq. 2005. “Neuronal Substrates of Complex Behaviors in *C. Elegans*.” *Annu. Rev. Neurosci.* 28: 451–501.

Bovetti, Serena, Claudio Moretti, Stefano Zucca, Marco Dal Maschio, Paolo Bonifazi, and Tommaso Fellin. 2017. “Simultaneous High-Speed Imaging and Optogenetic Inhibition in the Intact Mouse Brain.” Scientific Reports 7 (January): 40041.

Breimann, Laura, Friedrich Preusser, and Stephan Preibisch. 2019. “Light-Microscopy Methods in *C. Elegans* Research.” *Current Opinion in Systems Biology* 13 (February): 82–92.

Brenner, Sydney. 1974. “The Genetics of *Caenorhabditis Elegans*.” *Genetics* 77: 71–94.

Brockie, Penelope J., and Andres V. Maricq. 2006. “Ionotropic Glutamate Receptors: Genetics, Behavior and Electrophysiology.” *WormBook*, January, 1–16.

Brown, André E. X., and William R. Schafer. 2015. “Automated Behavioural Fingerprinting of *Caenorhabditis Elegans* Mutants.” In *Systems Genetics: Linking Genotypes and Phenotypes*, 234–256.

Brown, André E.X., Eviatar I. Yemini, Laura J. Grundy, Tadas Jucikas, and William R. Schafer.

2013. “A Dictionary of Behavioral Motifs Reveals Clusters of Genes Affecting *Caenorhabditis Elegans* Locomotion.” *Proceedings of the National Academy of Sciences of the United States of America* 110: 791–796.

Callou, Thais P., Renato Garcia, Adriana Mukai, Natalia T. Giacomin, Rodrigo Guimarães de Souza, and Samir J. Bechara. 2016. “Advances in Femtosecond Laser Technology.” *Clinical Ophthalmology* 10: 697–703.

Chalasani, Sreekanth H., Nikos Chronis, Makoto Tsunozaki, Jesse M. Gray, Daniel Ramot, Miriam B. Goodman, and Cornelia I. Bargmann. 2007. “Dissecting a Circuit for Olfactory Behaviour in *Caenorhabditis Elegans*.” *Nature* 450 (7166): 63–70.

Chalfie, Martin, Yuan Tu, Ghia Euskirchen, William W. Ward, and Douglas C. Prasher. 1994. “Green Fluorescent Protein as a Marker for Gene Expression.” *Science* 263: 802–805.

Chao, Michael Y., Hidetoshi Komatsu, Hana S. Fukuto, Heather M. Dionne, and Anne C. Hart. 2004. “Feeding Status and Serotonin Rapidly and Reversibly Modulate a *Caenorhabditis Elegans* Chemosensory Circuit.” *Proceedings of the National Academy of Sciences of the United States of America* 101: 15512–15517.

Chen, Tong-Sheng, Shao-Qun Zeng, Qing-Ming Luo, Zhi-Hong Zhang, and Wei Zhou. 2002. “High-Order Photobleaching of Green Fluorescent Protein inside Live Cells in Two-Photon Excitation Microscopy.” *Biochem. Biophys. Res. Commun.* 291 (5): 1272–75.

Cheung, Benny H. H., Merav Cohen, Candida Rogers, Onder Albayram, and Mario De Bono. 2005. “Experience-Dependent Modulation of *C. Elegans* Behavior by Ambient Oxygen.” *Current Biology* 15: 905–917.

Chi, Cynthia A., Damon A. Clark, Stella Lee, David Biron, Linjiao Luo, Christopher V. Gabel, Jeffrey Brown, Piali Sengupta, and Aravinthan D. T. Samuel. 2007. “Temperature and Food Mediate Long-Term Thermotactic Behavioral Plasticity by Association-Independent Mechanisms in *C. Elegans*.” *J. Exp. Biol.* 210 (Pt 22): 4043–52.

Chiel, H. J., and R. D. Beer. 1997. “The Brain Has a Body: Adaptive Behavior Emerges from Interactions of Nervous System, Body and Environment.” *Trends Neurosci.* 20 (12): 553–57.

Chirico, Giuseppe, Fabio Cannone, Giancarlo Baldini, and Alberto Diaspro. 2003. “Two-Photon Thermal Bleaching of Single Fluorescent Molecules.” *Biophys. J.* 84 (1): 588–98.

Chow, Brian Y., Xue Han, Allison S. Dobry, Xiaofeng Qian, Amy S. Chuong, Mingjie Li, Michael A. Henninger, et al. 2010. “High-Performance Genetically Targetable Optical Neural Silencing by Light-Driven Proton Pumps.” *Nature* 463 (7277): 98–102.

Collins, Kevin M., Addys Bode, Robert W. Fernandez, Jessica E. Tanis, Jacob C. Brewer, Matthew

S. Creamer, and Michael R. Koelle. 2016. “Activity of the *C. Elegans* Egg-Laying Behavior Circuit Is Controlled by Competing Activation and Feedback Inhibition.” *ELife* 5.

Cronin, Christopher J., Jane E. Mendel, Saleem Mukhtar, Young-Mee Kim, Robert C. Stirbl, Jehoshua Bruck, and Paul W. Sternberg. 2005. “An Automated System for Measuring Parameters of Nematode Sinusoidal Movement.” *BMC Genet.* 6 (February): 5.

Deisseroth, Karl. 2015. “Optogenetics: 10 Years of Microbial Opsins in Neuroscience.” *Nature Neuroscience* 18: 1213.

Denk, W., J. H. Strickler, and W. W. Webb. 1990. “Two-Photon Laser Scanning Fluorescence Microscopy.” Science 248 (4951): 73–76.

Denk, Winfried, David W. Piston, and Watt W. Webb. 1995. “{Two-Photon} Molecular Excitation in {Laser-Scanning} Microscopy.” In *Handbook of Biological Confocal Microscopy*, edited by James B Pawley, 445–58. Boston, MA: Springer US.

Diaspro, Alberto, and Giuseppe Chirico. 2003. “Two-Photon Excitation Microscopy.” In *Advances in Imaging and Electron Physics*, edited by Peter W Hawkes, 126:195. Elsevier.

Diaspro, Alberto, Giuseppe Chirico, and Maddalena Collini. 2005. “Two-Photon Fluorescence Excitation and Related Techniques in Biological Microscopy.” Quarterly Reviews of Biophysics 38 (2): 97–166.

Diaspro, Alberto, Giuseppe Chirico, Cesare Usai, Paola Ramoino, and Jurek Dobrucki. 2006. “Photobleaching.” In *Handbook Of Biological Confocal Microscopy*, edited by James B Pawley, 690–702. Boston, MA: Springer US.

Dickinson, Daniel J., Ariel M. Pani, Jennifer K. Heppert, Christopher D. Higgins, and Bob Goldstein. 2015. “Streamlined Genome Engineering with a Self-Excising Drug Selection Cassette.” *Genetics* 200: 1035–1049.

DiLoreto, Elizabeth M., Christopher D. Chute, Samantha Bryce, and Jagan Srinivasan. 2019. “Novel Technological Advances in Functional Connectomics in *C. Elegans*.” *J Dev Biol* 7 (2).

Dipon Ghosh, D, Tom Sanders, Soonwook Hong, Li Yan McCurdy, Daniel L Chase, Netta Cohen, Michael R Koelle, and Michael N Nitabach. 2016. “Neural Architecture of {Hunger-Dependent} Multisensory Decision Making in *C. Elegans*.” *Neuron* 92 (5): 1049–62.

Drobizhev, Mikhail, Nikolay S. Makarov, Shane E. Tillo, Thomas E. Hughes, and Aleksander Rebane. 2011. “Two-Photon Absorption Properties of Fluorescent Proteins.” *Nat. Methods* 8 (April): 393.

Durst, M E, G Zhu, and C Xu. 2008. “Simultaneous Spatial and Temporal Focusing in Nonlinear

Microscopy." *Opt. Commun.* 281 (7): 1796–1805.

Durst, Michael E., and Anthony Turcios. 2019. "Temporal Focusing with Remote Axial Scanning via Dispersion with an Electrically Tunable Lens." In *Biophotonics Congress: Optics in the Life Sciences Congress 2019*, NW1C.5. Optical Society of America.

Dusenbery, D. B. 1985. "Using a Microcomputer and Video Camera to Simultaneously Track 25 Animals." *Comput. Biol. Med.* 15 (4): 169–75.

Edwards, Stacey L., Nicole K. Charlie, Marie C. Milfort, Brandon S. Brown, Christen N. Gravlin, Jamie E. Knecht, and Kenneth G. Miller. 2008. "A Novel Molecular Solution for Ultraviolet Light Detection in Caenorhabditis Elegans." *PLoS Biol.* 6 (8): e198.

Egnor, S. E. Roian, and Kristin Branson. 2016. "Computational Analysis of Behavior." *Annual Review of Neuroscience* 39: 217–236.

Elwassif, Maged M., Qingjun Kong, Maribel Vazquez, and Marom Bikson. 2006. "Bio-Heat Transfer Model of Deep Brain Stimulation-Induced Temperature Changes." Journal of Neural Engineering 3 (4): 306–15.

Erbguth, Karen, Matthias Prigge, Franziska Schneider, Peter Hegemann, and Alexander Gottschalk. 2012. "Bimodal Activation of Different Neuron Classes with the Spectrally Red-Shifted Channelrhodopsin Chimera {C1V1} in *Caenorhabditis Elegans*." PLoS One 7 (10): e46827.

Escobet-Montalbán, Adrià, Roman Spesyvtsev, Mingzhou Chen, Wardiya Afshar Saber, Melissa Andrews, C. Simon Herrington, Michael Mazilu, and Kishan Dholakia. 2018. "Wide-Field Multiphoton Imaging through Scattering Media without Correction." Science Advances 4 (10): eaau1338.

Evans, Thomas C. 2006. "Transformation and Microinjection." WormBook: The Online Review of *C. Elegans* Biology 10.

Ezcurra, Marina, Yoshinori Tanizawa, Peter Swoboda, and William R. Schafer. 2011. "Food Sensitizes *C. Elegans* Avoidance Behaviours through Acute Dopamine Signalling." *EMBO J.* 30 (6): 1110–22.

Faumont, Serge, Gary Rondeau, Tod R. Thiele, Kristy J. Lawton, Kathryn E. McCormick, Matthew Sottile, Oliver Griesbeck, et al. 2011. "An Image-Free Opto-Mechanical System for Creating Virtual Environments and Imaging Neuronal Activity in Freely Moving *Caenorhabditis Elegans*." *PLoS One* 6 (9): e24666.

Feng, Zhaoyang, Christopher J. Cronin, John H. Wittig Jr., Paul W. Sternberg, and William R. Schafer. 2004. "An Imaging System for Standardized Quantitative Analysis of *C. Elegans*

Behavior." *BMC Bioinformatics* 5 (August): 115.

Fenno, Lief, Ofer Yizhar, and Karl Deisseroth. 2011. "The Development and Application of Optogenetics." *Annual Review of Neuroscience* 34: 389–412.

Field, Jeffrey J., Ramón Carriles, Kraig E. Sheetz, Eric V. Chandler, Erich E. Hoover, Shane E. Tillo, Thom E. Hughes, Anne W. Sylvester, David Kleinfeld, and Jeff A. Squier. 2010. "Optimizing the Fluorescent Yield in Two-Photon Laser Scanning Microscopy with Dispersion Compensation." *Optics Express* 18: 13661–13672.

Fire, A. 1986. "Integrative Transformation of *Caenorhabditis Elegans*." *EMBO J.* 5 (10): 2673–80.

Fischer, Katharina Elisabeth, Nathalie Alexandra Vladis, and Karl Emanuel Busch. 2018. "Optogenetic Applications in the Nematode *Caenorhabditis Elegans*." In *Optogenetics: A Roadmap*, edited by Albrecht Stroh, 89–116. New York, NY: Springer New York.

Flavell, Steven W., Navin Pokala, Evan Z. Macosko, Dirk R. Albrecht, Johannes Larsch, and Cornelia I. Bargmann. 2013. "Serotonin and the Neuropeptide PDF Initiate and Extend Opposing Behavioral States in *C. Elegans*." *Cell* 154: 1023–1035.

Frangi, Alejandro F., Wiro J. Niessen, and Max A. Viergever. 2001. "Three-Dimensional Modeling for Functional Analysis of Cardiac Images: A Review." *IEEE Transactions on Medical Imaging* 20: 2–25.

Friend, James, and Leslie Yeo. 2010. "Fabrication of Microfluidic Devices Using Polydimethylsiloxane." *Biomicrofluidics* 4: 026502.

Friston, Karl J. 2011. "Functional and Effective Connectivity: A Review." *Brain Connectivity* 1: 13–36.

Ghosh, D. Dipon, Tom Sanders, Soonwook Hong, Li Yan McCurdy, Daniel L. Chase, Netta Cohen, Michael R. Koelle, and Michael N. Nitabach. 2016. "Neural Architecture of Hunger-Dependent Multisensory Decision Making in *C. Elegans*." *Neuron* 92: 1049–1062.

Giles, Andrew C., Jacqueline K. Rose, and Catharine H. Rankin. 2005. "Investigations of Learning and Memory in *Caenorhabditis Elegans*." *International Review of Neurobiology* 69: 37–71.

Goldey, Glenn J., Demetris K. Roumis, Lindsey L. Glickfeld, Aaron M. Kerlin, R. Clay Reid, Vincent Bonin, Dorothy P. Schafer, and Mark L. Andermann. 2014. "Removable Cranial Windows for Long-Term Imaging in Awake Mice." *Nature Protocols* 9: 2515–2538.

Goodman, Miriam B., Theodore H. Lindsay, Shawn R. Lockery, and Janet E. Richmond. 2012. "Electrophysiological Methods for *Caenorhabditis Elegans* Neurobiology." *Methods in Cell Biology* 107: 409–436.

Gouveia, Luiz Carlos Paiva, and Bhaskar Choubey. 2016. “Advances on CMOS Image Sensors.” *Sensor Review* 36: 231–239.

Guillermin, Manon L., Mayra A. Carrillo, and Elissa A. Hallem. 2017. “A Single Set of Interneurons Drives Opposite Behaviors in *C. Elegans*.” *Current Biology* 27: 2630–2639.e6.

Guo, Zengcai V., Anne C. Hart, and Sharad Ramanathan. 2009. “Optical Interrogation of Neural Circuits in *Caenorhabditis Elegans*.” *Nat. Methods* 6 (12): 891–96.

Ha, Heon ick, Michael Hendricks, Yu Shen, Christopher V. Gabel, Christopher Fang-Yen, Yuqi Qin, Daniel Colón-Ramos, Kang Shen, Aravinthan D.T. Samuel, and Yun Zhang. 2010. “Functional Organization of a Neural Network for Aversive Olfactory Learning in *Caenorhabditis Elegans*.” *Neuron* 68: 1173–1186.

Hall, David H., Robyn Lints, and Zeynep Altun. 2005. “Nematode Neurons: Anatomy and Anatomical Methods in *Caenorhabditis Elegans*.” *International Review of Neurobiology*.

Harris, Todd W., Igor Antoshechkin, Tamberlyn Bieri, Darin Blasiar, Juancarlos Chan, Wen J Chen, Norie De La Cruz, et al. 2010. “WormBase: A Comprehensive Resource for Nematode Research.” *Nucleic Acids Res.* 38 (Database issue): 463.

Hebb, Donald Olding. 1962. *The Organization of Behavior: A Neuropsychological Theory*. Science Editions.

Hedgecock, E. M., and R. L. Russell. 1975. “Normal and Mutant Thermotaxis in the Nematode *Caenorhabditis Elegans*.” *Proceedings of the National Academy of Sciences of the United States of America* 72: 4061–4065.

Hendricks, Michael, and Yun Zhang. 2013. “Complex {RIA} Calcium Dynamics and Its Function in Navigational Behavior.” *Worm* 2 (3): e25546.

Henze, D. A., Z. Borhegyi, J. Csicsvari, A. Mamiya, K. D. Harris, and G. Buzsáki. 2000. “Intracellular Features Predicted by Extracellular Recordings in the Hippocampus in Vivo.” *J. Neurophysiol.* 84 (1): 390–400.

Herry, Cyril, Stephane Ciocchi, Verena Senn, Lynda Demmou, Christian Müller, and Andreas Lüthi. 2008. “Switching on and off Fear by Distinct Neuronal Circuits.” *Nature* 454: 600–606.

Hobert, Oliver. 2016. “A Map of Terminal Regulators of Neuronal Identity in *Caenorhabditis Elegans*.” *Wiley Interdiscip. Rev. Dev. Biol.* 5 (4): 474–98.

Hochbaum, Daniel R., Yongxin Zhao, Samouil L. Farhi, Nathan Klapoetke, Christopher A. Werley, Vikrant Kapoor, Peng Zou, et al. 2014. “All-Optical Electrophysiology in Mammalian Neurons Using Engineered Microbial Rhodopsins.” *Nature Methods* 11: 825–833.

Hodgkin, A. L., and A. F. Huxley. 1939. “Action Potentials Recorded from inside a Nerve Fibre [8].” *Nature* 144: 710–711. https://doi.org/10.1038/144710a0.

Hodgkin, J. 1983. “Male Phenotypes and Mating Efficiency in {CAENORHABDITIS} {ELEGANS}.” *Genetics* 103 (1): 43–64.

Huang, Tianxiao, Yan Sun, Zheng Zhang, Shixiong Deng, and Rui Peng. 2017. “Monoamine and Neuropeptide Connections Significantly Alter the Degree Distributions of the *Caenorhabditis Elegans* Connectome.” *Neuroreport* 28 (16): 1071–77.

Husson, Steven J., Wagner Steuer Costa, Cornelia Schmitt, and Alexander Gottschalk. 2018. “Keeping Track of Worm Trackers.”

Husson, Steven J., Wagner Steuer Costa, Sebastian Wabnig, Jeffrey N. Stirman, Joseph D. Watson, Clay W. Spencer, Jasper Akerboom, et al. 2012. “Optogenetic Analysis of a Nociceptor Neuron and Network Reveals Ion Channels Acting Downstream of Primary Sensors.” *Curr. Biol.* 22 (9): 743–52.

Husson, Steven J., Alexander Gottschalk, and Andrew M. Leifer. 2013. “Optogenetic Manipulation of Neural Activity in *C. Elegans*: From Synapse to Circuits and Behaviour.” *Biology of the Cell* 105: 235–250.

Jacques, Steven L. 2013. “Optical Properties of Biological Tissues: A Review.” *Phys. Med. Biol.* 58 (11): 37–61.

Ji, Na, Jeremy Freeman, and Spencer L. Smith. 2016. “Technologies for Imaging Neural Activity in Large Volumes.” *Nature Neuroscience* 19: 1154–1164.

Jin, Xin, Navin Pokala, and Cornelia I. Bargmann. 2016. “Distinct Circuits for the Formation and Retrieval of an Imprinted Olfactory Memory.” *Cell* 164: 632–643. https://doi.org/10.1016/j.cell.2016.01.007.

Johansson, Johannes D. 2010. “Spectroscopic Method for Determination of the Absorption Coefficient in Brain Tissue.” *J. Biomed. Opt.* 15 (5): 57005.

Kalies, S., K. Kuetemeyer, and A. Heisterkamp. 2011. “Mechanisms of High-Order Photobleaching and Its Relationship to Intracellular Ablation.” *Biomed. Opt. Express, BOE* 2 (4): 805–16.

Kano, Takashi, Penelope J. Brockie, Toshihiro Sassa, Hiroyuki Fujimoto, Yasushi Kawahara, Yuichi Iino, Jerry E. Mellem, David M. Madsen, Ryuji Hosono, and Andres V. Maricq. 2008. “Memory in *Caenorhabditis Elegans* Is Mediated by NMDA-Type Ionotropic Glutamate Receptors.” *Current Biology* 18: 1010–1015.

Kato, Saul, Harris S. Kaplan, Tina Schrödel, Susanne Skora, Theodore H. Lindsay, Eviatar Yemini, Shawn Lockery, and Manuel Zimmer. 2015. “Global Brain Dynamics Embed the Motor

Command Sequence of *Caenorhabditis Elegans*." *Cell* 163 (3): 656–69.

Katz, Ori, Eran Small, Yaron Bromberg, and Yaron Silberberg. 2011. "Focusing and Compression of Ultrashort Pulses through Scattering Media." *Nature Photonics* 5: 372.

Kerr, Jason N. D., and Winfried Denk. 2008. "Imaging in Vivo: Watching the Brain in Action." *Nature Reviews Neuroscience* 9: 195–205.

Kerr, Rex A. 2006. "Imaging the Activity of Neurons and Muscles." *WormBook*.

Kim, Eric, Lin Sun, Christopher V. Gabel, and Christopher Fang-Yen. 2013. "Long-Term Imaging of *Caenorhabditis Elegans* Using Nanoparticle-Mediated Immobilization." *PLoS ONE* 8: e53419.

Kiontke, Karin, and Walter Sudhaus. 2006. "Ecology of *Caenorhabditis* Species." *WormBook*.

Klapoetke, Nathan C., Yasunobu Murata, Sung Soo Kim, Stefan R. Pulver, Amanda Birdsey-Benson, Yong Ku Cho, Tania K. Morimoto, et al. 2014. "Independent Optical Excitation of Distinct Neural Populations." *Nat. Methods* 11 (3): 338–46.

Kocabas, Askin, Ching Han Shen, Zengcai V. Guo, and Sharad Ramanathan. 2012. "Controlling Interneuron Activity in *Caenorhabditis Elegans* to Evoke Chemotactic Behaviour." *Nature* 490: 273–277.

Larsch, Johannes, Steven W. Flavell, Qiang Liu, Andrew Gordus, Dirk R. Albrecht, and Cornelia I. Bargmann. 2015. "A Circuit for Gradient Climbing in *C. Elegans* Chemotaxis." *Cell Reports* 12: 1748–1760. https://doi.org/10.1016/j.celrep.2015.08.032.

Larsch, Johannes, Donovan Ventimiglia, Cornelia I. Bargmann, and Dirk R. Albrecht. 2013. "High-Throughput Imaging of Neuronal Activity in *Caenorhabditis Elegans*." *Proc. Natl. Acad. Sci. U. S. A.* 110 (45): 4266–73.

Lefort, Claire. 2017. "A Review of Biomedical Multiphoton Microscopy and Its Laser Sources." *J. Phys. D Appl. Phys.* 50 (October).

Leifer, Andrew M., Christopher Fang-Yen, Marc Gershow, Mark J. Alkema, and Aravinthan D. T. Samuel. 2011. "Optogenetic Manipulation of Neural Activity in Freely Moving *Caenorhabditis Elegans*." *Nat. Methods* 8 (2): 147–52.

Li, Zhaoyu, Yidong Li, Yalan Yi, Wenming Huang, Song Yang, Weipin Niu, Li Zhang, et al. 2012. "Dissecting a Central Flip-Flop Circuit That Integrates Contradictory Sensory Cues in *C. Elegans* Feeding Regulation." *Nature Communications* 3: 776.

Li, Zhaoyu, Jie Liu, Maohua Zheng, and X. Z. Shawn Xu. 2014. "Encoding of Both Analog- and Digital-like Behavioral Outputs by One *C. Elegans* Interneuron." *Cell* 159: 751–765.

Liedtke, Wolfgang, David M. Tobin, Cornelia I. Bargmann, and Jeffrey M. Friedman. 2003. "Mammalian {TRPV4} ({VR-OAC}) Directs Behavioral Responses to Osmotic and Mechanical Stimuli in *Caenorhabditis Elegans*." *Proc. Natl. Acad. Sci. U. S. A.* 100 (November): 14531–36.

Lisicovas, Viktoras, Bala Murali Krishna Mariserla, Chakradhar Sahoo, Reuben T. Harding, Michael K. L. Man, E Laine Wong, Julien Madéo, and Keshav M. Dani. 2019. "Improving Signal and Photobleaching Characteristics of Temporal Focusing Microscopy with the Increase in Pulse Repetition Rate." *Methods and Protocols* 2.

Liu, Mochi, Anuj K. Sharma, Joshua W. Shaevitz, and Andrew M. Leifer. 2018. "Temporal Processing and Context Dependency in *Caenorhabditis Elegans* Response to Mechanosensation." *Elife* 7 (June).

Lockery, Shawn R., and Miriam B. Goodman. 2009. "The Quest for Action Potentials in *C. Elegans* Neurons Hits a Plateau." *Nature Neuroscience* 12: 377–378.

Logothetis, N. K., J. Pauls, M. Augath, T. Trinath, and A. Oeltermann. 2001. "Neurophysiological Investigation of the Basis of the FMRI Signal." *Nature* 412: 150–157.

Luo, Linjiao, Nathan Cook, Vivek Venkatachalam, Luis A. Martinez-Velazquez, Xiaodong Zhang, Ana C. Calvo, Josh Hawk, et al. 2014. "Bidirectional Thermotaxis in *Caenorhabditis Elegans* Is Mediated by Distinct Sensorimotor Strategies Driven by the AFD Thermosensory Neurons." *Proc. Natl. Acad. Sci. U. S. A.* 111: 2776–2781.

Luo, Linjiao, Quan Wen, Jing Ren, Michael Hendricks, Marc Gershow, Yuqi Qin, Joel Greenwood, et al. 2014. "Dynamic Encoding of Perception, Memory, and Movement in a *C. Elegans* Chemotaxis Circuit." *Neuron* 82: 1115–1128.

McDiarmid, Troy A., Evan L. Ardiel, and Catharine H. Rankin. 2015. "The Role of Neuropeptides in Learning and Memory in *Caenorhabditis Elegans*." *Current Opinion in Behavioral Sciences* 2 (April): 15–20.

McEwan, Andrea H., and Catharine H. Rankin. 2013. "Mechanosensory Learning and Memory in *Caenorhabditis Elegans*." In *Invertebrate Learning and Memory*, edited by Randolf Menzel and Paul R Benjamin, 91. Academic Press.

Mellem, Jerry E., Penelope J. Brockie, David M. Madsen, and Andres V. Maricq. 2008. "Action Potentials Contribute to Neuronal Signaling in *C. Elegans*." *Nature Neuroscience* 11: 865–867.

Mellem, Jerry E., Penelope J. Brockie, Yi Zheng, David M. Madsen, and Andres V. Maricq. 2002. "Decoding of Polymodal Sensory Stimuli by Postsynaptic Glutamate Receptors in *C.*

Elegans." *Neuron* 36 (5): 933–44.

Metaxakis, Athanasios, Dionysia Petratou, and Nektarios Tavernarakis. 2018. "Multimodal Sensory Processing in *Caenorhabditis Elegans*." *Open Biology* 8.

Miller, David R., Jeremy W. Jarrett, Ahmed M. Hassan, and Andrew K. Dunn. 2017. "Deep Tissue Imaging with Multiphoton Fluorescence Microscopy." Current Opinion in Biomedical Engineering 4 (December): 32–39.

Mohammadi, Aylia, Jarlath Byrne Rodgers, Ippei Kotera, and William S. Ryu. 2013. "Behavioral Response of *Caenorhabditis Elegans* to Localized Thermal Stimuli." BMC Neuroscience 14 (1): 66.

Morrison, Glenn E., and Derek Van Der Kooy. 2001. "A Mutation in the AMPA-Type Glutamate Receptor, Glr-1, Blocks Olfactory Associative and Nonassociative Learning in *Caenorhabditis Elegans*." *Behavioral Neuroscience* 115: 640.

Morrison, Glenn E., Joseph Y M Wen, Susan Runciman, and Derek Van Der Kooy. 1999. "Olfactory Associative Learning in *Caenorhabditis Elegans* Is Impaired in Lrn-1 and Lrn-2 Mutants." *Behavioral Neuroscience* 113: 358.

Mouridi, Sonia El, Claire Lecroisey, Philippe Tardy, Marine Mercier, Alice Leclercq-Blondel, Nora Zariohi, and Thomas Boulin. 2017. "Reliable {CRISPR/Cas9} Genome Engineering in *Caenorhabditis Elegans* Using a Single Efficient {sgRNA} and an Easily Recognizable Phenotype." *G3* 7 (5): 1429–37.

Nabavi, Sadegh, Rocky Fox, Christophe D. Proulx, John Y. Lin, Roger Y. Tsien, and Roberto Malinow. 2014. "Engineering a Memory with LTD and LTP." *Nature* 511: 348–352.

Nagel, Eike, Christoph Klein, Ingo Paetsch, Sabine Hettwer, Bernhard Schnackenburg, Karl Wegscheider, and Eckart Fleck. 2003. "Magnetic Resonance Perfusion Measurements for the Noninvasive Detection of Coronary Artery Disease." *Circulation* 108 (4): 432–37.

Nagel, Georg, Martin Brauner, Jana F. Liewald, Nona Adeishvili, Ernst Bamberg, and Alexander Gottschalk. 2005. "Light Activation of Channelrhodopsin-2 in Excitable Cells of *Caenorhabditis Elegans* Triggers Rapid Behavioral Responses." *Curr. Biol.* 15 (24): 2279–84.

Nakai, J., M. Ohkura, and K. Imoto. 2001. "A High Signal-to-Noise Ca^{2+} Probe Composed of a Single Green Fluorescent Protein." *Nature Biotechnology* 19: 137–141.

Nakano, Akihiko. 2002. "Spinning-Disk Confocal Microscopy -- a Cutting-Edge Tool for Imaging of Membrane Traffic." Cell Structure and Function 27 (5): 349–55.

Nguyen, Jeffrey P., Frederick B. Shipley, Ashley N. Linder, George S. Plummer, Mochi Liu, Sagar

U. Setru, Joshua W. Shaevitz, and Andrew M. Leifer. 2016. “Whole-Brain Calcium Imaging with Cellular Resolution in Freely Behaving *Caenorhabditis Elegans*.” *Proc. Natl. Acad. Sci. U. S. A.* 113 (8): 1074–81.

Nichols, Annika L. A., Tomáš Eichler, Richard Latham, and Manuel Zimmer. 2017. “A Global Brain State Underlies *C. Elegans* Sleep Behavior.” *Science* 356 (6344).

Ohkura, Masamichi, Takuya Sasaki, Chiaki Kobayashi, Yuji Ikegaya, and Junichi Nakai. 2012. “An Improved Genetically Encoded Red Fluorescent Ca^{2+} Indicator for Detecting Optically Evoked Action Potentials.” *PLoS One* 7 (7): e39933.

Oron, Dan, and Yaron Silberberg. 2005. “Spatiotemporal Coherent Control Using Shaped, Temporally Focused Pulses.” *Opt. Express* 13 (24): 9903–8.

Oron, Dan, and Yaron Silberberg . 2015. “Temporal Focusing Microscopy.” *Cold Spring Harb. Protoc.* 2015 (2): 145–51.

Oron, Dan, Eran Tal, and Yaron Silberberg. 2005. “Scanningless Depth-Resolved Microscopy.” *Opt. Express* 13 (5): 1468–76.

Papagiakoumou, Eirini, Aurélien Bègue, Ben Leshem, Osip Schwartz, Brandon M. Stell, Jonathan Bradley, Dan Oron, and Valentina Emiliani. 2013. “Functional Patterned Multiphoton Excitation Deep inside Scattering Tissue.” Nature Photonics 7 (February): 274.

Piatkevich, Kiryl D., Erica E. Jung, Christoph Straub, Changyang Linghu, Demian Park, Ho Jun Suk, Daniel R. Hochbaum, et al. 2018. “A Robotic Multidimensional Directed Evolution Approach Applied to Fluorescent Voltage Reporters Article.” *Nature Chemical Biology* 14: 352–360.

Picot, Alexis, Soledad Dominguez, Chang Liu, I-Wen Chen, Dimitrii Tanese, Emiliano Ronzitti, Pascal Berto, et al. 2018. “Temperature Rise under {Two-Photon} Optogenetic Brain Stimulation.” *Cell Rep.* 24 (5): 1243-1253.e5.

Pierce-Shimomura, J. T., T. M. Morse, and S. R. Lockery. 1999. “The Fundamental Role of Pirouettes in *Caenorhabditis Elegans* Chemotaxis.” *J. Neurosci.* 19 (21): 9557–69.

Podgorski, Kaspar, and Gayathri Ranganathan. 2016. “Brain Heating Induced by Near-Infrared Lasers during Multiphoton Microscopy.” *J. Neurophysiol.* 116 (3): 1012–23.

Ponder, E. 1962. “The Coefficient of Thermal Conductivity of Blood and of Various Tissues.” *J. Gen. Physiol.* 45 (January): 545–51.

Poppendiek, H. F., R. Randall, J. A. Breeden, J. E. Chambers, and J. R. Murphy. 1967. “Thermal Conductivity Measurements and Predictions for Biological Fluids and Tissues.” *Cryobiology* 3 (4): 318–27.

Prevedel, Robert, Aart J. Verhoef, Alejandro J. Pern'ia-Andrade, Siegfried Weisenburger, Ben S. Huang, Tobias Nöbauer, Alma Fernández, et al. 2016. "Fast Volumetric Calcium Imaging across Multiple Cortical Layers Using Sculpted Light." *Nat. Methods* 13 (October): 1021.

Prevedel, Robert, Young-Gyu Yoon, Maximilian Hoffmann, Nikita Pak, Gordon Wetzstein, Saul Kato, Tina Schrödel, et al. 2014. "Simultaneous Whole-Animal {3D} Imaging of Neuronal Activity Using Light-Field Microscopy." *Nat. Methods* 11 (7): 727–30.

Qian, Yong, Kiryl D. Piatkevich, Benedict Mc Larney, Ahmed S. Abdelfattah, Sohum Mehta, Mitchell H. Murdock, Sven Gottschalk, et al. 2019. "A Genetically Encoded Near-Infrared Fluorescent Calcium Ion Indicator." *Nature Methods* 16: 171–174.

Qu, Junle, Lixin Liu, Yonghong Shao, Hanben Niu, and Bruce Z Gao. 2012. "Recent Progress in Multifocal Multiphoton Microscopy." *J. Innov. Opt. Health Sci.* 5 (3).

Rakowski, Franciszek, Jagan Srinivasan, Paul W. Sternberg, and Jan Karbowski. 2013. "Synaptic Polarity of the Interneuron Circuit Controlling *C. Elegans* Locomotion." *Front. Comput. Neurosci.* 7 (October): 128.

Ramot, Daniel, Brandon E. Johnson, Tommie L. Berry Jr., Lucinda Carnell, and Miriam B. Goodman. 2008. "The Parallel Worm Tracker: A Platform for Measuring Average Speed and Drug-Induced Paralysis in Nematodes." *PLoS One* 3 (5): e2208.

Rankin, C. H., C. D. Beck, and C. M. Chiba. 1990. "Caenorhabditis Elegans: A New Model System for the Study of Learning and Memory." *Behav. Brain Res.* 37 (1): 89–92.

Rankin, Catharine H. 2004. "Invertebrate Learning: What Can't a Worm Learn?" *Curr. Biol.* 14 (15): 617–18.

Richard S. Sutton and Andrew G. Barto. 1998. *Reinforcement Learning*. The MIT Press.

Richmond, Janet. 2005. "Synaptic Function." *WormBook*, December, 1–14.

Riddle, Donald L. 1997. *C. Elegans {II}*. Cold Spring Harbor Laboratory Press.

Roberts, William M., Steven B. Augustine, Kristy J. Lawton, Theodore H. Lindsay, Tod R. Thiele, Eduardo J. Izquierdo, Serge Faumont, et al. 2016. "A Stochastic Neuronal Model Predicts Random Search Behaviors at Multiple Spatial Scales in *C. Elegans*." *ELife* 5.

Russell, Joshua, Andrés G. Vidal-Gadea, Alex Makay, Carolyn Lanam, and Jonathan T. Pierce-Shimomura. 2014. "Humidity Sensation Requires Both Mechanosensory and Thermosensory Pathways in *Caenorhabditis Elegans*." *Proceedings of the National Academy of Sciences of the United States of America* 111: 8269–8274.

Saeki, Satoshi, Masayuki Yamamoto, and Yuichi Iino. 2001. "Plasticity of Chemotaxis Revealed

by Paired Presentation of a Chemoattractant and Starvation in the Nematode *Caenorhabditis Elegans*." *Journal of Experimental Biology* 204: 1757–1764.

Sakai, Naoko, Ryo Iwata, Saori Yokoi, Rebecca A. Butcher, Jon Clardy, Masahiro Tomioka, and Yuichi Iino. 2013. "A Sexually Conditioned Switch of Chemosensory Behavior in *C. Elegans*." *PLoS ONE* 8: e68676.

Sambongi, Y., T. Nagae, Y. Liu, T. Yoshimizu, K. Takeda, Y. Wada, and M. Futai. 1999. "Sensing of Cadmium and Copper Ions by Externally Exposed {ADL}, {ASE}, and {ASH} Neurons Elicits Avoidance Response in *Caenorhabditis Elegans*." *Neuroreport* 10 (4): 753–57.

Sasakura, Hiroyuki, Yuki Tsukada, Shin Takagi, and Ikue Mori. 2013. "Japanese Studies on Neural Circuits and Behavior of *Caenorhabditis Elegans*." *Frontiers in Neural Circuits* 7: 187.

Scanziani, Massimo, and Michael Häusser. 2009. "Electrophysiology in the Age of Light." *Nature* 461: 930–939.

Schild, Lisa C., and Dominique A. Glauser. 2015. "Dual Color Neural Activation and Behavior Control with Chrimson and CoChR in *Caenorhabditis Elegans*." *Genetics* 200: 1029–1034.

Schindelin, Johannes, Ignacio Arganda-Carreras, Erwin Frise, Verena Kaynig, Mark Longair, Tobias Pietzsch, Stephan Preibisch, et al. 2012. "Fiji: An Open-Source Platform for Biological-Image Analysis." *Nat. Methods* 9 (7): 676–82.

Schrödel, Tina, Robert Prevedel, Karin Aumayr, Manuel Zimmer, and Alipasha Vaziri. 2013. "Brain-Wide {3D} Imaging of Neuronal Activity in *Caenorhabditis Elegans* with Sculpted Light." *Nat. Methods* 10 (10): 1013–20.

Schwiening, Christof J. 2012. "A Brief Historical Perspective: Hodgkin and Huxley." *Journal of Physiology* 590: 2571–2575.

Serrano-Saiz, Esther, Richard J. Poole, Terry Felton, Feifan Zhang, Estanisla Daniel De La Cruz, and Oliver Hobert. 2013. "Modular Control of Glutamatergic Neuronal Identity in *C. Elegans* by Distinct Homeodomain Proteins." *Cell* 155 (3): 659–73.

Shimozawa, Togo, Kazuo Yamagata, Takefumi Kondo, Shigeo Hayashi, Atsunori Shitamukai, Daijiro Konno, Fumio Matsuzaki, et al. 2013. "Improving Spinning Disk Confocal Microscopy by Preventing Pinhole Cross-Talk for Intravital Imaging." *Proc. Natl. Acad. Sci. U. S. A.* 110 (9): 3399–3404.

Shingai, Ryuzo, Morimichi Furudate, Katsunori Hoshi, and Yuishi Iwasaki. 2013. "Evaluation of Head Movement Periodicity and Irregularity during Locomotion of *Caenorhabditis Elegans*." *Frontiers in Behavioral Neuroscience* 7: 20.

Shtonda, Boris Borisovich, and Leon Avery. 2006. "Dietary Choice Behavior in *Caenorhabditis*

Elegans." *Journal of Experimental Biology* 209 (1): 89–102.

Sordillo, Laura A., Yang Pu, Sebastião Pratavieira, Yury Budansky, and Robert R. Alfano. 2014. "Deep Optical Imaging of Tissue Using the Second and Third Near-Infrared Spectral Windows." *Journal of Biomedical Optics* 19: 056004.

Stephens, Greg J., Bethany Johnson-Kerner, William Bialek, and William S. Ryu. 2008. "Dimensionality and Dynamics in the Behavior of *C. Elegans*." *PLoS Computational Biology* 4: e1000028.

Stern, Shay, Christoph Kirst, and Cornelia I. Bargmann. 2017. "Neuromodulatory Control of Long-Term Behavioral Patterns and Individuality across Development." *Cell* 171: 1649–1662.e10.

STI Components, Inc. 2014. "{STI} Chemical Resistance Chart."

Stiernagle, Theresa. 2006. "Maintenance of *C. Elegans*." *WormBook*.

Stirman, Jeffrey N., Matthew M. Crane, Steven J. Husson, Alexander Gottschalk, and Hang Lu. 2012. "A Multispectral Optical Illumination System with Precise Spatiotemporal Control for the Manipulation of Optogenetic Reagents." *Nat. Protoc.* 7 (2): 207–20.

Stujenske, Joseph M., Timothy Spellman, and Joshua A. Gordon. 2015. "Modeling the Spatiotemporal Dynamics of Light and Heat Propagation for In Vivo Optogenetics." *Cell Rep.* 12 (3): 525–34.

Summers, Philip J., Robert M. Layne, Amanda C. Ortega, Gareth P. Harris, Bruce A. Bamber, and Richard W. Komuniecki. 2015. "Multiple Sensory Inputs Are Extensively Integrated to Modulate Nociception in *C. Elegans*." *Journal of Neuroscience* 35: 10331–10342.

Suzuki, Hiroshi, Tod R. Thiele, Serge Faumont, Marina Ezcurra, Shawn R. Lockery, and William R. Schafer. 2008. "Functional Asymmetry in *Caenorhabditis Elegans* Taste Neurons and Its Computational Role in Chemotaxis." *Nature* 454: 114–117.

Swierczek, Nicholas A., Andrew C. Giles, Catharine H. Rankin, and Rex A. Kerr. 2011. "High-Throughput Behavioral Analysis in *C. Elegans*." *Nat. Methods* 8 (7): 592–98.

Taketani, Makoto, and Michel Baudry. 2006. *Advances in Network Electrophysiology: Using Multi-Electrode Arrays*. *Advances in Network Electrophysiology: Using Multi-Electrode Arrays*.

Taniguchi, Gun, Takayuki Uozumi, Keisuke Kiriyama, Tomoko Kamizaki, and Takaaki Hirotsu. 2014. "Screening of Odor-Receptor Pairs in *Caenorhabditis Elegans* Reveals Different Receptors for High and Low Odor Concentrations." *Sci. Signal.* 7 (323): ra39.

Therrien, O. D., B. Aubé, S. Pagès, P. De Koninck, and D. Côté. 2011. "Wide-Field Multiphoton

Imaging of Cellular Dynamics in Thick Tissue by Temporal Focusing and Patterned Illumination." *Biomed. Opt. Express* 2 (3): 696–704.

Tian, Lin, S. Andrew Hires, Tianyi Mao, Daniel Huber, M. Eugenia Chiappe, Sreekanth H. Chalasani, Leopoldo Petreanu, et al. 2009. "Imaging Neural Activity in Worms, Flies and Mice with Improved {GCaMP} Calcium Indicators." *Nat. Methods* 6 (12): 875–81.

Timbers, Tiffany A., Andrew C. Giles, Evan L. Ardiel, Rex A. Kerr, and Catharine H. Rankin. 2013. "Intensity Discrimination Deficits Cause Habituation Changes in Middle-Aged *Caenorhabditis Elegans*." *Neurobiology of Aging* 34: 621–631.

Tobin, David M., David M. Madsen, Amanda Kahn-Kirby, Erin L. Peckol, Gary Moulder, Robert Barstead, Andres V. Maricq, and Cornelia I. Bargmann. 2002. "Combinatorial Expression of {TRPV} Channel Proteins Defines Their Sensory Functions and Subcellular Localization in *C. Elegans* Neurons." *Neuron* 35 (2): 307–18.

Vaziri, Alipasha, and Charles V. Shank. 2010. "Ultrafast Widefield Optical Sectioning Microscopy by Multifocal Temporal Focusing." *Opt. Express* 18 (19): 19645–55.

Vaziri, Alipasha, Jianyong Tang, Hari Shroff, and Charles V. Shank. 2008. "Multilayer Three-Dimensional Super Resolution Imaging of Thick Biological Samples." *Proc. Natl. Acad. Sci. U. S. A.* 105 (51): 20221–26.

Venkatachalam, Vivek, Ni Ji, Xian Wang, Christopher Clark, James Kameron Mitchell, Mason Klein, Christopher J Tabone, et al. 2016. "Pan-Neuronal Imaging in Roaming *Caenorhabditis Elegans*." *Proc. Natl. Acad. Sci. U. S. A.* 113 (8): 1082–88.

Verkhratsky, Alexei, and Vladimir Parpura. 2014. "History of Electrophysiology and the Patch Clamp." *Methods in Molecular Biology* 1183: 1–19.

Wang, Wenjing, Christina K. Kim, and Alice Y. Ting. 2019. "Molecular Tools for Imaging and Recording Neuronal Activity." *Nat. Chem. Biol.* 15 (2): 101–10.

Ward, S. 1973. "Chemotaxis by the Nematode *Caenorhabditis Elegans*: Identification of Attractants and Analysis of the Response by Use of Mutants." *Proc. Natl. Acad. Sci. U. S. A.* 70 (3): 817–21.

Waschuk, Stephen A., Arandi G. Bezerra Jr., Lichi Shi, and Leonid S. Brown. 2005. "Leptosphaeria Rhodopsin: Bacteriorhodopsin-like Proton Pump from a Eukaryote." *Proc. Natl. Acad. Sci. U. S. A.* 102 (19): 6879–83.

Weiner, Andrew M. 2009. *Ultrafast Optics*. John Wiley and sons.

Wen, Joseph Y. M., Namit Kumar, Glenn Morrison, Gloria Rambaldini, Susan Runciman, Joyce Rousseau, and Derek Van Der Kooy. 1997. "Mutations That Prevent Associative Learning in

C. Elegans." *Behavioral Neuroscience*.

White, J. G., E. Southgate, J. N. Thomson, and S. Brenner. 1986. "The Structure of the Nervous System of the Nematode *C. Elegans*." *Philos T R Soc B* 314: 1–340.

Winbush, Ari, Matthew Gruner, Grant W. Hennig, and Alexander M. van der Linden. 2015. "Long-Term Imaging of Circadian Locomotor Rhythms of a Freely Crawling *C. Elegans* Population." *Journal of Neuroscience Methods* 249: 66–74.

Winter, Peter B., Renee M. Brielmann, Nicholas P. Timkovich, Helio T. Navarro, Andreia Teixeira-Castro, Richard I. Morimoto, and Luis A. N. Amaral. 2016. "A Network Approach to Discerning the Identities of *C. Elegans* in a Free Moving Population." *Sci. Rep.* 6 (October): 34859.

Wood, William B. 1988. *The Nematode Caenorhabditis Elegans*. Cold Spring Harbor Laboratory.

Xu, C., and F. W. Wise. 2013. "Recent Advances in Fiber Lasers for Nonlinear Microscopy." *Nat. Photonics* 7 (November).

Yang, Li, and Stanley J Miklavcic. 2005. "Theory of Light Propagation Incorporating Scattering and Absorption in Turbid Media." *Opt. Lett.* 30 (7): 792–94.

Yaroslavsky, A. N., P. C. Schulze, I. V. Yaroslavsky, R. Schober, F. Ulrich, and H. J. Schwarzmaier. 2002. "Optical Properties of Selected Native and Coagulated Human Brain Tissues in Vitro in the Visible and near Infrared Spectral Range." *Phys. Med. Biol.* 47 (12): 2059–73.

Yew, Elijah Y. S., Colin J. R. Sheppard, and Peter T. C. So. 2013. "Temporally Focused Wide-Field Two-Photon Microscopy: Paraxial to Vectorial." *Opt. Express* 21 (10): 12951–63.

Yoshida, Kazushi, Takaaki Hirotsu, Takanobu Tagawa, Shigekazu Oda, Tokumitsu Wakabayashi, Yuichi Iino, and Takeshi Ishihara. 2012. "Odour Concentration-Dependent Olfactory Preference Change in *C. Elegans*." *Nat. Commun.* 3 (March): 739.

Yu, Alex J., Troy A. McDiarmid, Evan L. Ardiel, and Catharine H. Rankin. 2019. "{High-Throughput} Analysis of Behavior Under the Control of Optogenetics in *Caenorhabditis Elegans*." *Curr. Protoc. Neurosci.* 86 (1): e57.

Zhang, Yun, Hang Lu, and Cornelia I. Bargmann. 2005. "Pathogenic Bacteria Induce Aversive Olfactory Learning in *Caenorhabditis Elegans*." *Nature* 438: 179–184.

Zhao, Yongxin, Satoko Araki, Jiahui Wu, Takayuki Teramoto, Yu-Fen Chang, Masahiro Nakano, Ahmed S Abdelfattah, et al. 2011. "An Expanded Palette of Genetically Encoded Ca^{2+} Indicators." *Science* 333 (6051): 1888–91.

Zheng, Maohua, Pengxiu Cao, Jiong Yang, X. Z. Shawn Xu, and Zhaoyang Feng. 2012. “Calcium Imaging of Multiple Neurons in Freely Behaving *C. Elegans*.” *J. Neurosci. Methods* 206 (1): 78–82.

Zhu, Guanghao, James van Howe, Michael Durst, Warren Zipfel, and Chris Xu. 2005. “Simultaneous Spatial and Temporal Focusing of Femtosecond Pulses.” *Opt. Express* 13 (6): 2153–59.